Seismic Waveform Modeling of Regional Phases
and
Wavefields from an Off-Center Explosion

Thesis by

Lian-She Zhao

In Partial Fulfillment of the Requirements

for the Degree of

Doctor of Philosophy

California Institute of Technology

Pasadena, California

1992

(Submitted July 10, 1991)

Acknowledgements

I thank all the people in this world for their companionship. When you need food, there is " McDonald's ".

I thank Professors Donald V. Helmberger and David G. Harkrider for their support, guidance and encouragement. It was a great experience to work with Don and Dave, you could have random walks.

I thank my academic advisor, Professor Thomas J. Ahrens for his suggestions and guidance. I thank Professors Toshiro Tanimoto, Hiroo Kanamori, Robert W. Clayton, Don L. Anderson, George R. Rossman and Peter J. Wyllie for the time they shared with me.

Great appreciation should be directed to my fellow students for making my stay at Caltech worth remembering. Especially I have to mention: Bradley Woods, always ready for my questions of any kind, Eddie Garnero, always smiling, and Shawn Larson, *mplot* designer. Discussions with Brad, Eddie, Shawn, Scott Phelps, Tom Duffy, Richard Stead, Doug Dreger, Joanne Yoshimura, Laura Jones, Dave Wald and Hongkie Thio contributed to my ideas and English. Suggestions from earlier Chinese students Jiajun Zhang and Yu Shen Zhang made it easier for me to make decisions.

I thank my mother for her persistence in my education. I thank my wife for her love, understanding and encouragement. To them, I dedicate this thesis.

General Abstract

This thesis consists of two parts. Part I (Chapter 1) is a theoretical study of wavefields radiated from an off-center explosion in an embedded solid sphere, while Part II (Chapters 2, 3 and 4) deals with seismic waveform modeling of regional phases.

Chapter 1 investigates the effects of asymmetric source regions on the excitation of seismic body waves of explosions. We give an analytic formulation for determining the wave fields from an off-center explosion in an embedded solid sphere in an elastic whole-space. It is shown that SH wave amplitudes can be ten times larger than the P wave amplitudes if the source is properly located.

Chapter 2 discusses the strategies of modeling regional Broadband recordings with the application to Harvard station recordings of November 25, 1988 Saguenay earthquake. We demonstrate that the longer period motions (WWSSN) preceding the direct S arrival can be modeled reasonably well with a crustal model consisting of a layer over half-space. While a generic model assumed to be the same everywhere can be used to model the P_{nl} waveshape, Helmberger and Engen (1980), some adjustments are required to fit the absolute timing of P_n and S_n for specific paths. In particular, path from the Saguenay event to Harvard is slower than expected for a shield environment and is associated with the roots of the Appalachian

Thrust Belt.

Chapters 3 and 4 concern the velocity structures of the Tibetan Plateau and surrounding regions. A fast shield-like velocity model, TIP, is proposed for the structure beneath the Tibetan Plateau as suggested by modeling SH waveforms in Chapter 3. The crustal model is determined by modeling Love waveforms and P_{nl} waveforms in the time domain while the upper mantle is constrained with S and SS waveform data. Relocations of Tibetan earthquakes are discussed in Chapter 4, assuming model TIP at source region and model JB at receiver regions. A detailed investigation of 100 such events yields a distinctly different picture from a random distribution of events down to a depth of about 50 kms given by ISC. Waveform modeling of depth phases such as pP indicates that only three or four events from of this population is actually deeper than 25 km. These few events occur near the edges of the Plateau where active subduction is occurring as suggested by the thrust-like nature of their mechanisms. The events occurred earlier than indicated by the ISC by 3 seconds on average which leads to about a 1.5% and 0.5% over estimation of P_n and S_n velocities respectively applying ISC tables and standard flat-layered models.

Table of Contents

PART I

Wave Fields from an Off-Center Explosion

CHAPTER 1

Wave Fields from an Off-Center Explosion in an Embedded Solid Sphere

ABSTRACT

This study investigates the effects of explosions in asymmetric source regions on the excitation of seismic body waves. We give an analytic formulation for determining the wave fields from an off-center explosion in an embedded solid sphere in an elastic whole-space. As expected, this geometry generates shear as well as compressional body waves. The calculated wave fields show that the degree of shear wave generation is determined by the asymmetry of the source region. The results are compared with the known analytic solutions of an explosion in an elastic whole-space and at the center of an elastic sphere embedded in the whole-space. The radiation patterns at different periods for different parameters of the media suggest that the asymmetry of the source region has significant effects on shorter period, but has only minor effects on long periods. The long period P to S wave maximum amplitude results are in agreement with that for explosions in axisymmetric cavities.

INTRODUCTION

Shear waves are almost always observed from underground explosions. One can visualize many ways to convert explosion P waves into SV waves. An obvious mechanism is the free-surface or other near by planar boundaries. But the presence of SH waves is especially perplexing. The SH waves are generally considered to be due to tectonic release from the volume relaxation of the local prestress surrounding the shot point or as a triggered earthquake on nearby fault planes (Press and Archambeau, 1962, Aki and Tsai, 1972). Other mechanisms for SH wave excitation have also been investigated; such as, the conversion of source P waves from explosions in long narrow valleys and the generation of S waves by explosions in anisotropic media and axisymmetric cavities (Ben-Menahem and Sena, 1990, Mandal and Toksoz, 1990, Glenn etal, 1985, 1986, and Rial and Moran, 1986).

We show in this paper that a significant amount of shear waves can be generated by an asymmetric source region. We give the formulation for the wave fields of an off-center explosive source in an elastic homogeneous sphere embedded in an elastic homogeneous whole-space with different elastic constants and densities. Our's differs from the usual scattering due to spherical inclusions problem found in the acoustic literature. For instance, Pao (1978) gives the scattering or transition matrix (Waterman,1969 and 1976, Varatharajulu and Pao, 1976) solution for a spherical cavity, a rigid sphere in a solid, and an elastic sphere in a fluid and a solid. The scattering matrix formulation is then compared to earlier obtained solutions for an incident plane wave with a stationary or sinusoidal time history (Pao and Mow,

1973). The effect of restricting the source duration to be finite for an incident plane P wave on a solid sphere is considered by Dubrovskiy and Morochnik (1989). The solution due to a spherical incident wave is given in Pao and Mow (1973). The only solution found by the authors for a source embedded eccentrically within a sphere was that by Thompson (1973) for a spherical source embedded in a fluid sphere in a fluid space. That problem is the fluid or acoustical analogue to our problem.

As in Thompson (1973), we expand the wave fields in spherical harmonics and use the interface boundary conditions at the spherical contact, welded in this case, to find the coefficients of the expansion. Since this is a whole space problem, the separation of the shear displacement field into SV and SH waves and potentials may seem an unwarranted complication. But, for completeness and for use in a later paper, we present potential expressions in APPENDIX A for an arbitrary orientation of the symmetry axis, which will facilitate the incorporation of this source into a vertically inhomogeneous elastic half-space problem. Initially, for ease of formulation, the spherical coordinate system is oriented with the source on the vertical axis, ie. $\theta=0$, so that only SV waves are generated. Once the displacement field is obtained, the coordinate system is rotated for a more general source orientation and expressions are then given in APPENDIX A to convert the wave fields into P, SV, and SH wave potentials and their respective displacement fields.

THEORY

The geometry and the coordinate system are given in Figure 1. The displacement resulting from an explosive source located at the spherical coordinates, (r_0, θ_0, ϕ_0) , in a homogeneous, isotropic, unbounded elastic medium may be expressed in the form (Ben-Menahem and Singh 1981, p384):

$$\mathbf{u}_0 = i k_\alpha g(\omega) A_0 \nabla h_0^{(2)}(k_\alpha R)$$

where the receiver is located at (r, θ, ϕ), $g(\omega)$ is the spectrum of explosive source function; ∇ is gradient; $h_0^{(2)}(k_\alpha R)$ is spherical Hankel function of second kind; $k_\alpha = \omega/\alpha$; α is the compressional velocity; $\alpha^2 = (\lambda + 2\mu)/\rho$ in terms of the density ρ and the lame' constants λ and μ; R is distance between source and receiver; and

$$A_0 = \frac{M_0}{4\pi(\lambda + 2\mu)}.$$

where M_0 is the seismic moment.

We now express the spherical Hankel function $h_0^{(2)}(k_\alpha R)$ in terms of r_0, r and the angle δ between the position vectors of the source and receiver as

$$h_0^{(2)}(k_\alpha R) = \sum_{l=0}^{l=\infty} (2l+1) j_l(k_\alpha r_0) h_l^{(2)}(k_\alpha r) P_l(\cos\delta)$$

where $r \geq r_0$, $j_l(k_\alpha r)$ is the spherical Bessel function; and $P_l(\cos\theta)$ is the Legendre function. Initially we replace δ by θ. This is equivalent to assuming that the source is located on the z axis, that is, $\theta_0 = 0$. With this substitution, the displacement expression becomes

$$\mathbf{u}_0 = i k_\alpha^2 g(\omega) A_0 \sum_{l=0}^{l=\infty} (2l+1) j_l(k_\alpha r_0) \mathbf{L}_{0l}^-(k_\alpha r)$$
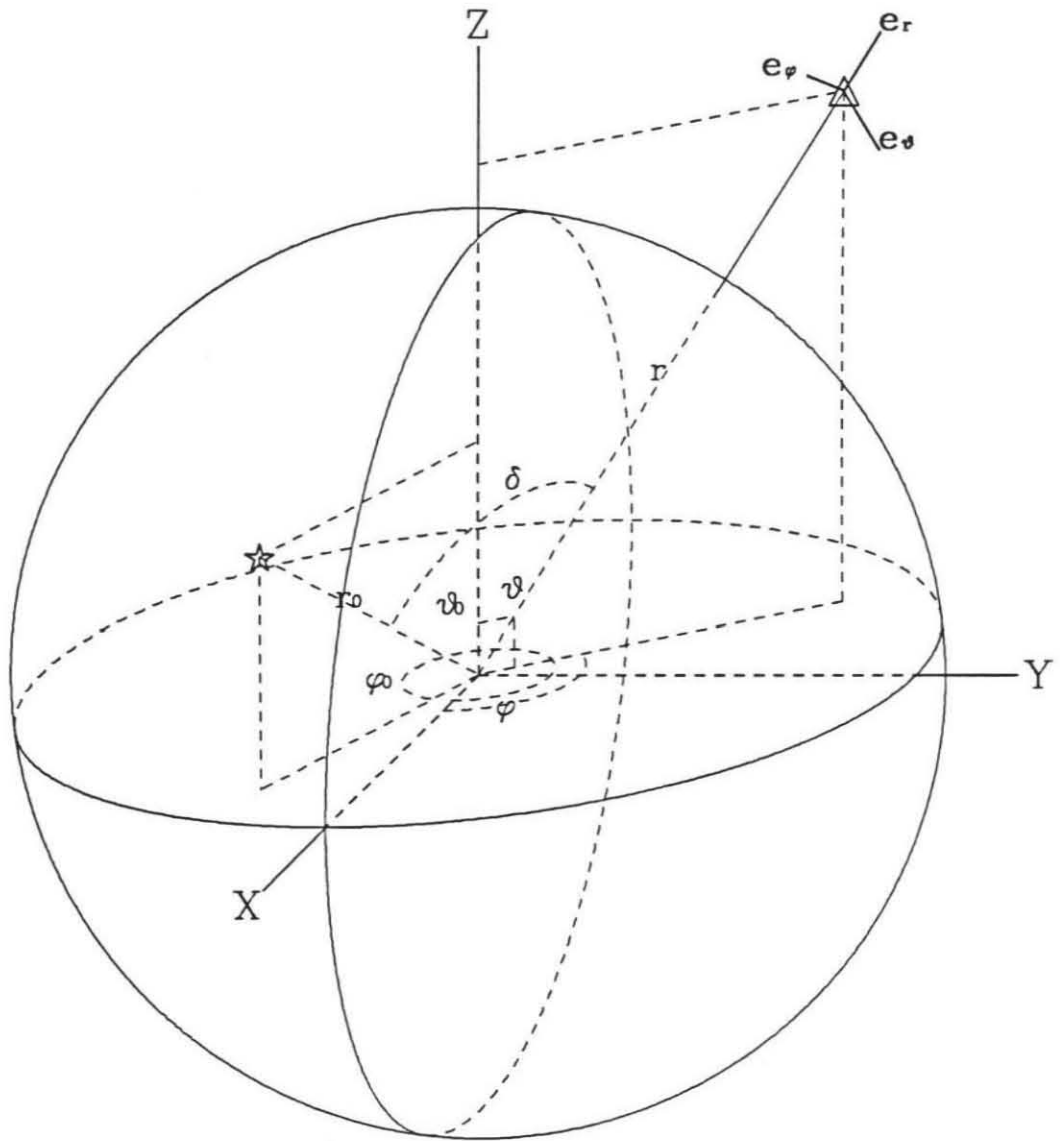
Figure 1. The geometry and the coordinate system used in this study. star is source, and triangle is receiver.

for $r \geq r_0$ and where $\mathbf{L}_{0l}^-(\mathbf{k}_\alpha r)$ is defined below.

If we bound the source medium by a sphere of radius $r = a$, we can assume the displacement field inside and outside as

$$\mathbf{u}_1 = \mathbf{u}_0 - \sum_{l=0}^{l=\infty} (2l+1)[a_l \mathbf{N}_{0l}^+(\mathbf{k}_{\beta_1} r) + b_l \mathbf{L}_{0l}^+(\mathbf{k}_{\alpha_1} r)] \tag{1a}$$

for $r > r_0$, $r \leq a$ and

$$\mathbf{u}_2 = \sum_{l=0}^{l=\infty} (2l+1)[c_l \mathbf{N}_{0l}^-(\mathbf{k}_{\beta_2} r) + d_l \mathbf{L}_{0l}^-(\mathbf{k}_{\alpha_2} r)] \tag{1b}$$

for $r \geq a$, where $k_\beta = \omega/\beta$; β is the shear velocity; and $\beta^2 = \mu/\rho$. The boundary conditions to be satisfied at $r = a$ are

$$\mathbf{u}_1 = \mathbf{u}_2 \tag{2a}$$

$$\mathbf{e}_r \cdot \Xi(\mathbf{u}_1) = \mathbf{e}_r \cdot \Xi(\mathbf{u}_2) \tag{2b}$$

, where Ξ is the stress dyadic. The displacement and stress dyadic can be conveniently expressed in terms of the Hansen vectors, which are the eigenvector solutions of the force-free Navier equation (Ben-Menahem and Singh 1981, Chapter 2). The Hansen vectors in terms of spherical harmonics are

$$\mathbf{L}_{ml}^\pm(\xi) = \frac{d}{d\xi} f_l^\pm(\xi) \mathbf{P}_{ml}(\theta,\phi) + \frac{1}{\xi} f_l^\pm(\xi)[l(l+1)]^{\frac{1}{2}} \mathbf{B}_{ml}(\theta,\phi)$$

$$\mathbf{N}_{ml}^\pm(\eta) = \frac{1}{\eta} f_l^\pm(\eta) l(l+1) \mathbf{P}_{ml}(\theta,\phi) + (\frac{d}{d\eta} + \frac{1}{\eta}) f_l^\pm(\eta)[l(l+1)]^{\frac{1}{2}} \mathbf{B}_{ml}(\theta,\phi)$$

where

$$\mathbf{P}_{ml}(\theta,\phi) = \mathbf{e}_r P^m_l(\cos\theta) e^{im\phi} = \mathbf{e}_r Y_{ml}(\theta,\phi)$$

$$\sqrt{l(l+1)} \mathbf{B}_{ml} = (\mathbf{e}_\theta \frac{\partial}{\partial\theta} + \mathbf{e}_\phi \frac{\partial}{\sin\theta\partial\phi}) P^m_l(\cos\theta) e^{im\phi}$$

and where $\xi = k_\alpha r$, $\eta = k_\beta r$, $f_l^+(z) = j_l(z)$, and $f_l^-(z) = h_l^{(2)}(z)$.

The corresponding stresses are given by

$$\mathbf{e}_r \cdot \Xi(\mathbf{L}) = 2\mu k_\alpha [F_{l,3}(\xi)\mathbf{P}_{ml} + F_{l,1}(\xi)[l(l+1)]^{\frac{1}{2}}\mathbf{B}_{ml}]$$

$$\mathbf{e}_r \cdot \Xi(\mathbf{N}) = \mu k_\beta [2l(l+1)F_{l,1}(\eta)\mathbf{P}_{ml} + F_{l,2}(\eta)[l(l+1)]^{\frac{1}{2}}\mathbf{B}_{ml}]$$

The functions $F_{l,i}$ are given by

$$F_{l,1}^{\pm}(z) = \frac{1}{z}(\frac{d}{dz} - \frac{1}{z})f_l^{\pm}(z) = \frac{(l-1)}{z^2}f_l^{\pm}(z) - \frac{1}{z}f_{l+1}^{\pm}(z)$$

$$F_{l,2}^{\pm}(z) = [\frac{2}{z^2}(l^2-1) - 1]f_l^{\pm}(z) + \frac{2}{z}f_{l+1}^{\pm}(z) = \frac{d_2 f_l^{\pm}}{dz^2} + \frac{(l-1)(l+2)}{z^2}f_l^{\pm}(z)$$

$$F_{l,3}^{\pm}(z) = [\frac{1}{z^2}l(l-1) - \frac{1}{2}(\frac{\alpha}{\beta})^2]f_l^{\pm}(z) + \frac{2}{z}f_{l+1}^{\pm}(z) = \frac{d^2}{dz^2}f_l^{\pm} - \frac{\lambda}{2\mu}f_l^{\pm}(z)$$

Substituting the above into equation (1), we have for the l th components of the displacements

$$\mathbf{u}_{1l} = i k_{\alpha_1}^2 g(\omega)A_0(2l+1)j(k_{\alpha_1}r_0)[f_l^{-'}(\xi_1)\mathbf{P}_l\mathbf{e}_r + \frac{1}{\xi_1}f_l^-(\xi_1)\frac{d}{d\theta}\mathbf{P}_l\mathbf{e}_\theta]$$

$$-(2l+1)a_l\frac{N^2}{\eta_1}f_l^+(\eta_1)\mathbf{P}_l\mathbf{e}_r - (2l+1)a_l(\frac{d}{d\eta} + \frac{1}{\eta_1})f_l^+(\eta_1)\frac{d}{d\theta}\mathbf{P}_l\mathbf{e}_\theta$$

$$-(2l+1)b_l f_l^{+'}(\xi_1)\mathbf{P}_l\mathbf{e}_r - (2l+1)b_l f_l^+(\xi_1)\frac{1}{\xi_1}\frac{d}{d\theta}\mathbf{P}_l\mathbf{e}_\theta$$

$$(3)$$

$$\mathbf{u}_{2l} = (2l+1)c_l\frac{N^2}{\eta_2}f_l^-(\eta_2)\mathbf{P}_l\mathbf{e}_r + (2l+1)c_l(\frac{d}{d\eta} + \frac{1}{\eta_2})f_l^-(\eta_2)\frac{d}{d\theta}\mathbf{P}_l\mathbf{e}_\theta$$

$$+(2l+1)d_l f_l^{-'}(\xi_2)\mathbf{P}_l\mathbf{e}_r + (2l+1)d_l f_l^-(\xi_2)\frac{1}{\xi_2}\frac{d}{d\theta}\mathbf{P}_l\mathbf{e}_\theta$$

and the l th components of the spherical surface tractions

$$\mathbf{e}_r \cdot \Xi(\mathbf{u}_{1l}) = i k_{\alpha_1}{}^2 g(\omega) A_0 (2l+1) j_l(k_{\alpha_1} r_0) [F^-_{l,3}(\xi_1) P_l(\cos\theta) \mathbf{e}_r$$

$$+ F^-_{l,1}(\xi_1) \frac{d}{d\theta} P_l(\cos\theta) \mathbf{e}_\theta]$$

$$-(2l+1) a_l \mu_1 k_{\beta_1} [2N^2 F^+_{l,1}(\eta_1) P_l(\cos\theta) \mathbf{e}_r + F^+_{l,2}(\eta_1) \frac{d}{d\theta} P_l(\cos\theta) \mathbf{e}_\theta]$$

$$-2(2l+1) b_l \mu_1 k_{\alpha_1} [F^+_{l,3}(\xi_1) P_l(\cos\theta) \mathbf{e}_r + F^+_{l,1}(\xi_1) \frac{d}{d\theta} P_l(\cos\theta) \mathbf{e}_\theta]$$

$$\mathbf{e}_r \cdot \Xi(\mathbf{u}_{2l}) = (2l+1) c_l \mu_2 k_{\beta_2} [2N^2 F^-_{l,1}(\eta_2) P_l(\cos\theta) \mathbf{e}_r + F^-_{l,2}(\eta_2) \frac{d}{d\theta} P_l(\cos\theta) \mathbf{e}_\theta]$$

$$+2(2l+1) d_l \mu_2 k_{\alpha_2} [F^-_{l,3}(\xi_2) P_l(\cos\theta) \mathbf{e}_r + F^-_{l,1}(\xi_2) \frac{d}{d\theta} P_l(\cos\theta) \mathbf{e}_\theta]$$

where $N^2 = l(l+1)$ and the prime ,($'$), denotes differentiation by the functions argument, and where $\xi_1 = k_{\alpha_1} a$, $\eta_1 = k_{\beta_1} a$, $\xi_2 = k_{\alpha_2} a$, and $\eta_2 = k_{\beta_2} a$.

Using equations (2), and comparing the coefficients of $P_l(\cos\theta) \mathbf{e}_r \cdot \mathbf{u}_l$, $\frac{d}{d\theta} P_l(\cos\theta) \mathbf{e}_\theta \cdot \mathbf{u}_l$, $P_l(\cos\theta) \mathbf{e}_r \cdot \Xi(\mathbf{u}_l) \cdot \mathbf{e}_r$, and $\frac{d}{d\theta} P_l(\cos\theta) \mathbf{e}_r \cdot \Xi(\mathbf{u}_l) \cdot \mathbf{e}_\theta$, we have the matrix equation

$$YC = D \tag{4}$$

where

$$D = i k_{\alpha_1}^2 g(\omega) A_0 j_l(k_{\alpha_1} r_0) [f_l^{-'}(\xi_1), \frac{1}{\xi_1} f_l^{-}(\xi_1), 2\mu_1 k_{\alpha_1} F^-_{l,3}(\xi_1), 2\mu k_{\alpha_1} F^-_{l,1}(\xi_1)]^T \tag{5}$$

$$C = (a_l, b_l, c_l, d_l)^T \tag{6}$$

$$
\mathbf{Y} = \begin{bmatrix}
\dfrac{N^2}{\eta_1} f\,_l^{+}(\eta_1) & f\,_l^{+'}(\xi_1) & \dfrac{N^2}{\eta_2} f\,_l^{-}(\eta_2) & f\,_l^{-'}(\xi_2) \\[2ex]
(\dfrac{d}{d\eta}+\dfrac{1}{\eta_1}) f\,_l^{+}(\eta_1) & \dfrac{1}{\xi_1} f\,_l^{+}(\xi_1) & (\dfrac{d}{d\eta}+\dfrac{1}{\eta_2}) f\,_l^{-}(\eta_2) & \dfrac{1}{\xi_2} f\,_l^{-}(\xi_2) \\[2ex]
2\mu_1 k_{\beta_1} N^2 F\,_{l,1}^{+}(\eta_1) & 2\mu_1 k_{\alpha_1} F\,_{l,3}^{+}(\xi_1) & 2\mu_2 k_{\beta_2} N^2 F\,_{l,1}^{-}(\eta_2) & 2\mu_2 k_{\alpha_2} F\,_{l,3}^{-}(\xi_2) \\[2ex]
\mu_1 k_{\beta_1} F\,_{l,2}^{+}(\eta_1) & 2\mu_1 k_{\alpha_1} F\,_{l,1}^{+}(\xi_1) & \mu_2 k_{\beta_2} F\,_{l,2}^{-}(\eta_2) & 2\mu_2 k_{\alpha_2} F\,_{l,1}^{-}(\xi_2)
\end{bmatrix}
$$

$$(7)$$

where T denotes transpose. We can now determine the coefficients (6) of the expansion (1) and equation (3) by equation (4).

Even though the potential relations in APPENDIX A are convenient for for including this source in propagator and generalized ray calculations, they are awkward for evaluating the whole space wave fields. For this, we introduce an alternative approach. If the source is located at $(r_0,0,0)$, the displacement fields are given by equations (1). Generally, if the source is located at (r_0,θ_0,ϕ_0), Figure 1, θ and ϕ should be changed to δ and γ, with $\cos\delta=\cos\theta\cos\theta_0+\sin\theta\sin\theta_0\cos(\phi-\phi_0)$. The range of δ is 0 to 360°, and δ is defined as the angle measured clockwise from the position vector of the source to the position vector of the receiver. For this source geometry, the coordinate system with $\mathbf{e}_{r_0}$ as the north pole has unit base vectors $(\mathbf{e}_r,\mathbf{e}_\delta,\mathbf{e}_\gamma)$, and coordinates (r,δ,γ) . Eventhough there are no displacements in the γ direction for this symmetry, the most straight forward way of defining δ is in terms of $\mathbf{e}_\gamma$, the normal to the plane containing r_0 and r. The displacement fields are now written as:

$$
\mathbf{u} = (u_P^r + u_{SV}^r)\mathbf{e}_r + (u_P^\delta + u_{SV}^\delta)\mathbf{e}_\delta,
$$

$$(8)$$

where

$$\mathbf{e}_\delta = \mathbf{e}_\gamma \times \mathbf{e}_r$$

$$= \frac{1}{\sin\delta}(\mathbf{e}_r(\mathbf{e}_r \cdot \mathbf{e}_{r_0}) - \mathbf{e}_{r_0}).$$

since

$$\mathbf{e}_\gamma = \mathbf{e}_{r_0} \times \mathbf{e}_r / \sin\delta$$

The P and SV displacements, u^r and u^δ, are obtained by summing over l the coefficients of $\mathbf{e}_r$ and $\mathbf{e}_\delta$ in the second of equations (3). Resolving the angular displacements, u^δ into the more general coordinate system (r,θ,ϕ), we can write the displacement fields as:

$$\mathbf{u} = u^r \mathbf{e}_r + u^\theta \mathbf{e}_\theta + u^\phi \mathbf{e}_\phi, \tag{9}$$

with

$$u^r = u_P^r + u_{SV}^r,$$

$$u^\theta = -(u_P^\delta + u_{SV}^\delta)(\sin\theta_0\cos\theta\cos(\phi-\phi_0) - \cos\theta_0\sin\theta)/\sin\delta,$$

and

$$u^\phi = (u_P^\delta + u_{SV}^\delta)\sin\theta_0\sin(\phi-\phi_0)/\sin\delta.$$

When $\delta = 0 \, or \, 180^o$, equations (9) no longer hold. This is when the source and receiver are on a line through the sphere origin and then we should use equations (3).

Before going on to numerical examples, there is one further point to discuss; the inferred seismic moment. In the following, we assume that the observed seismic radiation can be inverted back to the source region using

appropriate Green's functions. We further assume that the observers either do not know the details of the source's environment, such as in this case the material properties of the embedded sphere, or if they do have this knowledge, they decide not to correct for it. Then, the source region properties used in the Green's functions are that of the exterior medium and we will refer to this inverted moment as the inferred or "observed" seismic moment. For our source, the "observed" seismic moment is

$$M_{obs} = \frac{\rho_2 \alpha_2^2}{\rho_1 \alpha_1^2 + \frac{4}{3}(\rho_2 \beta_2^2 - \rho_1 \beta_1^2)} M_0 \tag{10}$$

where M_0 is the input moment of the explosion. By input moment, we mean the moment which would be measured if the confining or shot point medium of the sphere was a whole-space. This equation is obtained by using equation (B4) of Appendix B and letting ω go to zero. Since nuclear explosion sources are frequently characterized by A_0 or the more familiar notation, $\Psi(\infty)$, which is the asymptotic value of the reduced displacement potential for a long time, and

$$M_0 = 4\pi\rho\alpha^2\Psi(\infty),$$

we can write equation (10) as

$$\Psi(\infty)_{obs} = \frac{1}{1 + \frac{4}{3}\frac{\beta_1^2}{\alpha_1^2}\left[\frac{\mu_2}{\mu_1} - 1\right]} \Psi(\infty) \tag{11}$$

where the elastic rigidity $\mu = \rho\beta^2$ and as before the subscript 1 denotes the inclusion or shot point material and 2 denotes the exterior medium. Thus

the difference between "observed" and shot point $\Psi(\infty)$ is independent of density contrast and in source media with similar Poisson ratios is only a function of the rigidity ratio of the material in which the $\Psi(\infty)$ is measured and the shot point material. The smaller the shot point rigidity, the smaller the "observed" $\Psi(\infty)$ while large shot point rigidities cause amplification. Since the minimum realistic ratio of P to S wave ratios is $\sqrt{2}$, which corresponds to a Poisson ratio of zero, the maximum possible amplification is a factor of 3.

RESULTS

In this section, we present some numerical results. For all of the synthetics, we assume that the moment time history is a step function, i.e.,

$$g(\omega)=1/i\,\omega,$$

and

$$M_0=4\pi\rho_1\alpha_1^2\times10^{20}dyne-cm\,,$$

where ρ is in g/cm^3, and the velocities, α and β, are in $km/$sec, and distances in km. Thus $\Psi(\infty)$ is kept the same for the different spherical source media models. The distances are in km and the displacement is in cm. The spectral band-width is from 102.4 seconds in period to 10 Hz. As our standard model, we assume the elastic parameters and dimensions given in Table 1. The receiver is located 10 km from the center of the elastic sphere unless otherwise indicated. The material model for the whole-space outside of the sphere is reasonable for sedimentary regions, see for example Zhao et al.

Table 1. Model

α	β	ρ	radium
(km/sec)	(km/sec)	(g/cm^3)	km
1.80	0.41	1.84	0.5
4.55	2.57	2.45	

(1991). When investigating the effect of different elastic properties of the sphere, Nafe's velocity-density relation (Ludwig et al. 1970) is used to obtain densities and S wave velocities for a given P velocity. We used 20 terms to sum up the wave fields, see Equation (1). The error induced from truncation of order m, is approximately the order $m^6(r_0/r)^m$. This error determination is from the eccentricity expansion or addition theorem of Equation (1) and depends on the ratio of the arguments of the Bessel and Hankel functions used in the series expansion, which in turn removes any frequency dependence.

Figure 2 gives a comparison of displacement fields calculated by our infinite series formulation, i.e., inversion of equation (4), and by the numerical evaluation of two analytic closed form solutions. The upper pair of synthetics show the whole space results, while the lower pair show the results for a source located at the center of the solid sphere in a whole-space. The formulation for the wave field outside of the solid sphere due to a centered explosion is given in Appendix B. The solutions, both closed and series, are calculated in the frequency domain, and then transformed to the time domain, so that each pair of time histories show almost identical precursor artifacts, which are caused by the numerical transforms. The agreement within pairs is excellent.

In the following figures, we will refer to P and S wave arrivals as radial and azimuthal. These are u_P^r, u_P^δ, u_S^r, and u_S^δ respectively in the notation of the previous section. The P waves are the contribution to the displacement field from the P potential, they begin at the P wave arrival time,
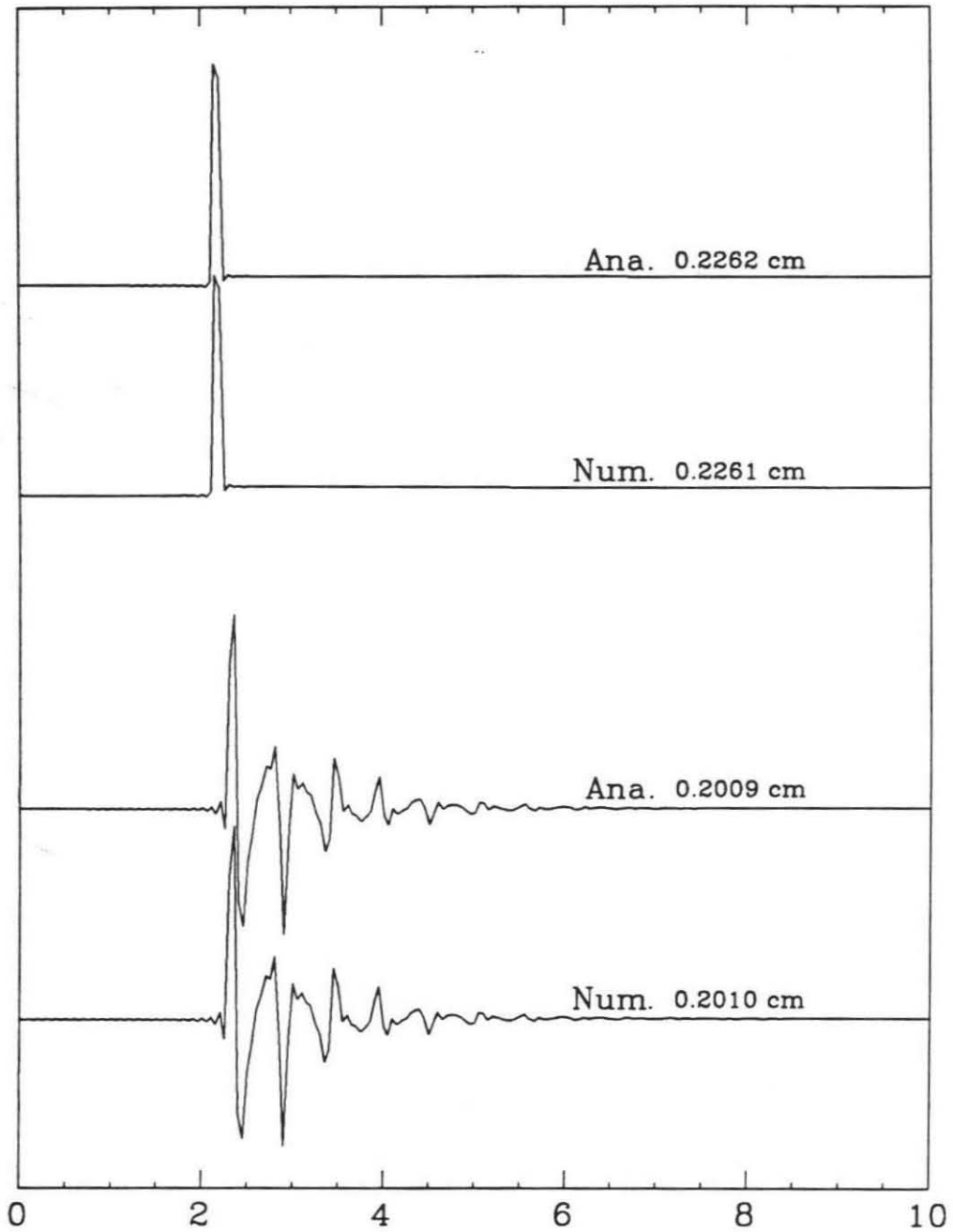
Figure 2. Comparisons of numerical results with two known analytical solutions. The upper is for the wavefields of whole space, while the lower is for the wave fields from a centered source in an embedded sphere. " Num. " denotes numerical and " Ana. " denotes analytic.

and physically correspond to P or compressional waves arriving at the receiver which have undergone multiple refections and conversions between P and S in the spherical source region. An analogous statement applies to the S waves with P replaced by S and compressional by shear. At a range, r, of 10 km for the standard model , the near-field P arrival u_P^δ, which is the displacement component perpendicular to the propagation direction, and the near-field S arrival u_S^r, which is the component in the radial or propagation direction, are about 10% of the far-field arrivals u_P^r and u_S^δ. For a dynamic point source, one would expect far-field dispacements to fall off as $1/r$ and the near-field to attenuate as $1/r^2$. This was investigated by generating wave fields at ranges from 5 to 40 km in 5 km intervals for the standard model. The wave form of each of these displacement components was found to be independent of range and by 10 km, the displacements fields indeed attenuated as predicted.

In most of the following examples, θ is set to 90°, i.e., the source and receiver are both in the horizontal plane. This was done to check our numerical algorithms for the transformations given in equation (8), which are used to obtain SV and SH displacements from the initial SV only shear displacement field.

Figure 3 shows displacements at a receiver located at (r,θ,ϕ)=$(10,90^\circ,90^\circ)$, with the source at $(0.45,90^\circ,180^\circ)$. At these coordinates, the source and receiver position vectors are 90° to each other with respect to the sphere origin. We see that, strong shear waves, as evidenced by the azimuthal component of S waves, are generated at receiver azimuths 90°
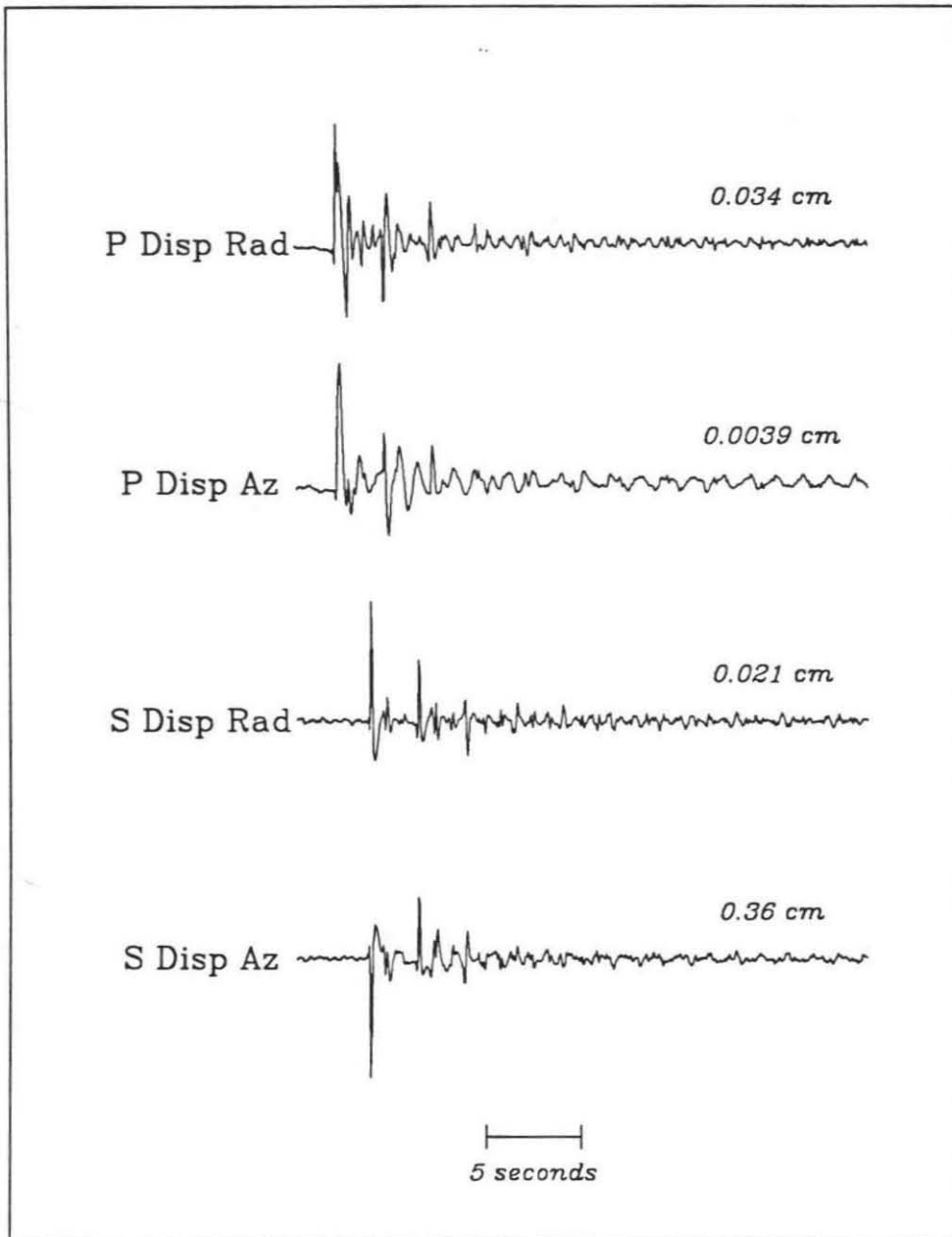
Figure 3. A example of wavefields from an off-centered source in a embedded sphere with a radium of 0.5 km. " P " is for the P waves, " S " is for the S waves. " Rad " is for the e_r component, " Az " is for the e_ϕ component. The numbers are the peak amplitudes.

from the symmetry axis of the source and the center of the sphere. Also the time difference between the two biggest arrivals in both the P and S waveforms, is about 2.5 seconds, which is the time needed for an S phase to travel through the sphere. This interval can be detected between many arrivals. Thus the bigger arrivals in the seismograms, except for direct P and S generated at the sphere boundary can be interpreted as phases, which have traveled through the sphere at least once as S. The S wave displacement is about a factor of 10 greater than the P wave displacement. This is somewhat misleading, since as we shall see in later examples, this is the azimuth of minimum P displacement and of maximum long period S.

The change in displacement fields as a function of source asymmetry is displayed in Figure 4 . The model and the geometry are the same as that used for Figure 3, except that the source radius, r_0 is varied from 0 to 0.45 km, the location in Figure 3, in 0.05 km increments. From this figure, we see that only P waves are generated when the source is at the center of the sphere, r_0 equal to 0. At this azimuth, as r_0 increases, the P wave maximum amplitude is reduced by about a factor of 10, while the S wave amplitude is increased to almost 50% greater than the P waves due to the centered source. The bottom traces, r_0=0.45 km , are the same as those in Figure 3 except on a common scale.

Figure 5 illustrates the effects on the wave fields as the velocity-density structure of the spherical source region is varied. The exterior medium properties are the same for all cases and are given in Table 1. The first row of traces are the same as those in Figure 3. For the bottom row,
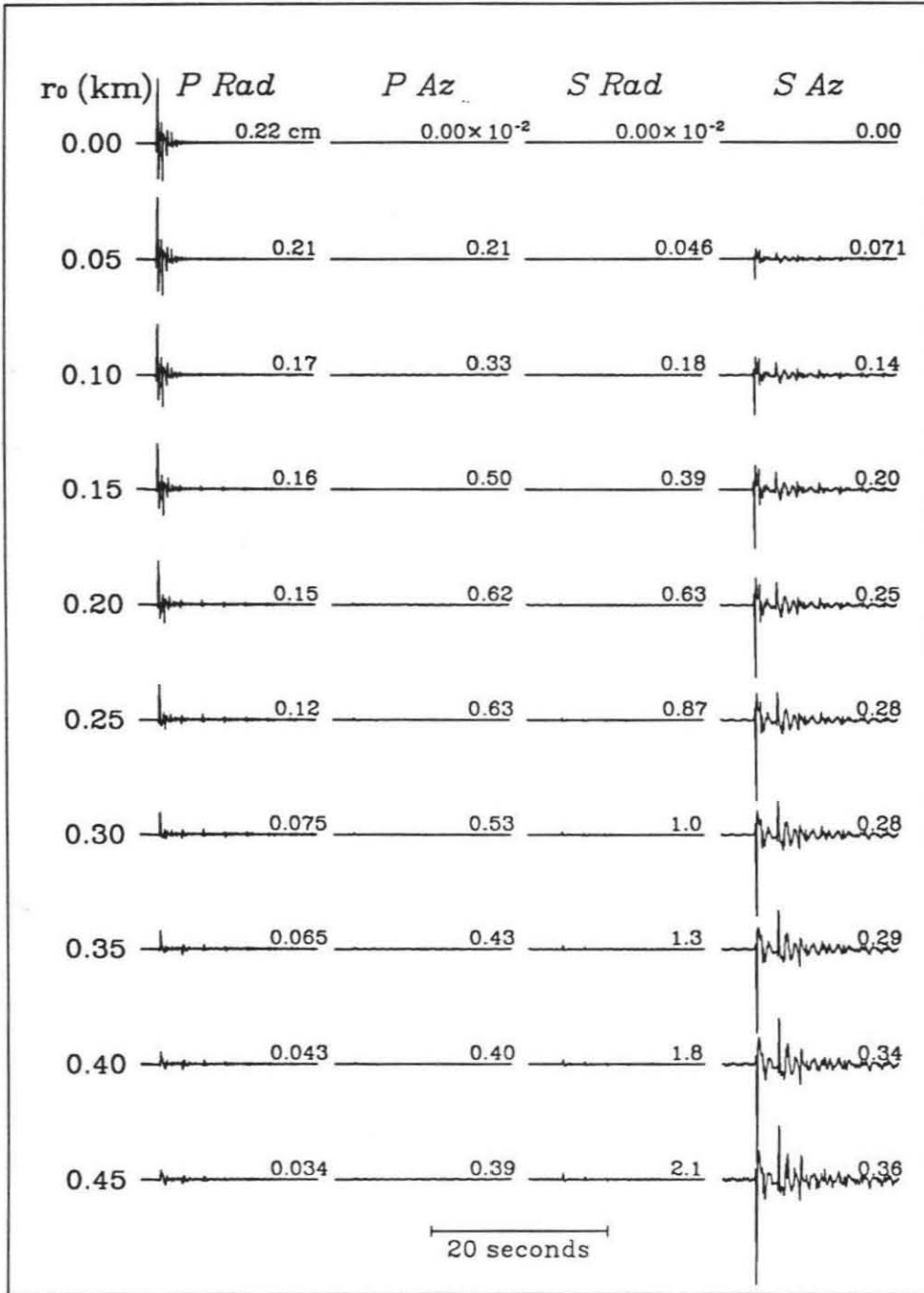
Figure 4. Wave fields for different source distances to the center of the embedded sphere with a radium of 0.5 km. The 10^{-2} on the second and third traces of the first line, apply to all the traces in the second and third columns. r_0 is the distance from the source to the center. The vertical scale is the same for all seismograms.
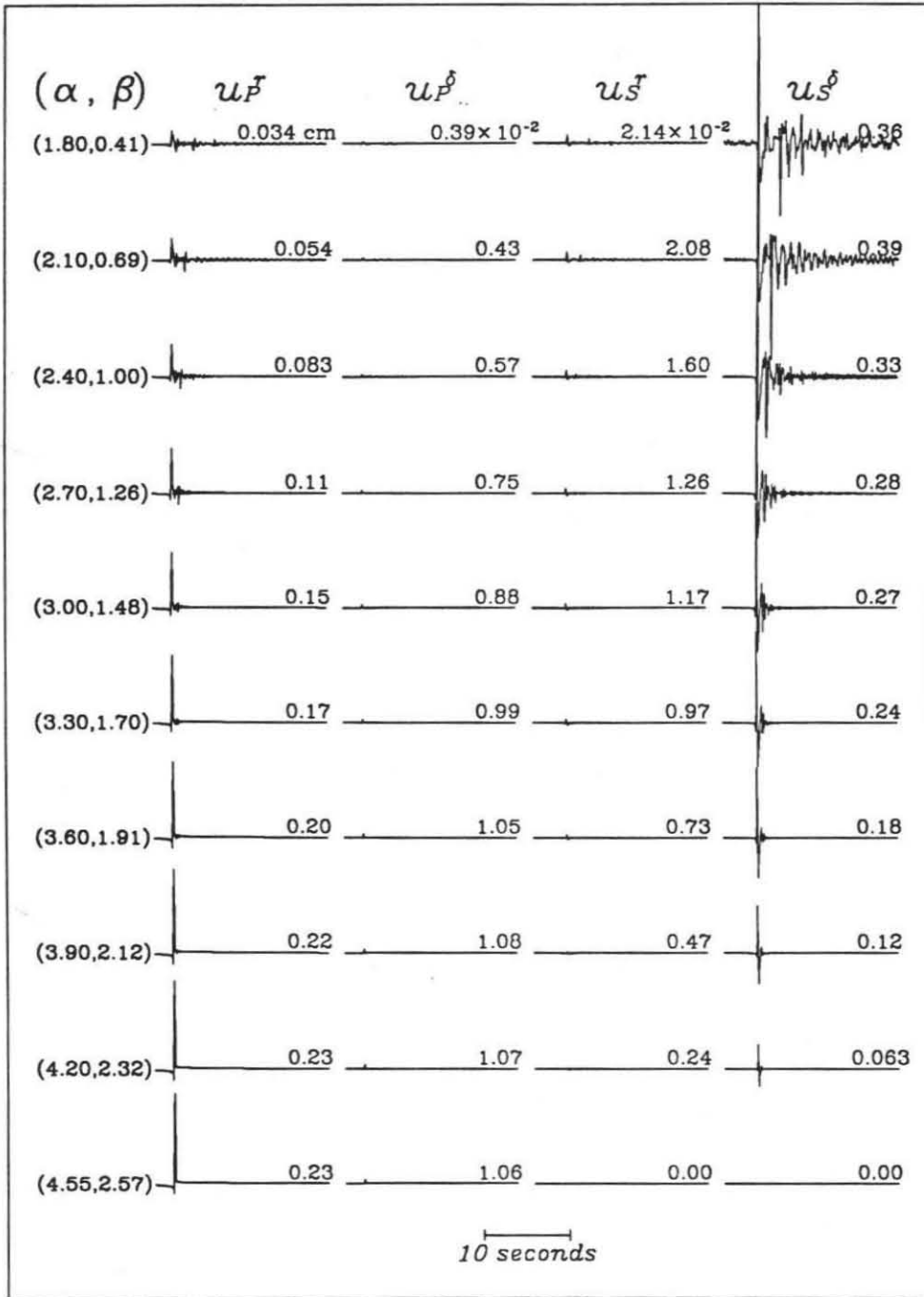
Figure 5. Wave fields for different materials in the embedded sphere. α is compressional velocity, and β is shear velocity. Nafe's velocity-density relation is assumed for the shear velocity and density ρ.

the sphere and surrounding space have identical properties and thus these traces are the results for an explosion in a whole space. The source-receiver geometry is the same as Figure 3. We see that, the greater the elastic contrast between the spherical source region and exterior medium, the greater the S waves generated. This is evidenced by the relative excitation between P and S on any given row. In making amplitude comparisons between differing source media in the figure, one must remember that the moment increases as one moves down the row with increasing velocities and density while $\Psi(\infty)$ remains unchanged.

Figure 6 shows the wave field variations as the angle, δ, between the source and receiver position vectors changes. When $\delta=0$, the source, the receiver, and the center of the sphere are in a line. At this angle, no P or S δ components are generated. The near-field S r components are P to S conversions at the boundary which are focused back on the axis. The elastic sphere acts as a contact lens magnifying the wave fields, like the Earth does at the antipode of an earthquake (Rial, 1980). When δ increases, the P amplitude decreases, and S amplitude increases. The bottom traces are again those of Figure 3. Comparing the bottom row with the top row and then with the top row of Figure 4, we see that the maximum S wave amplitude is almost 3 times the maximum P wave amplitude for this the maximum degree of asymmetry investigated and is more than 50% greater than the P wave amplitude for the center explosion. Thus from Figures 4,5 and 6, we see that the degree of asymmetry of the source region and the contrast between the media determine the intensity of the S wave fields.
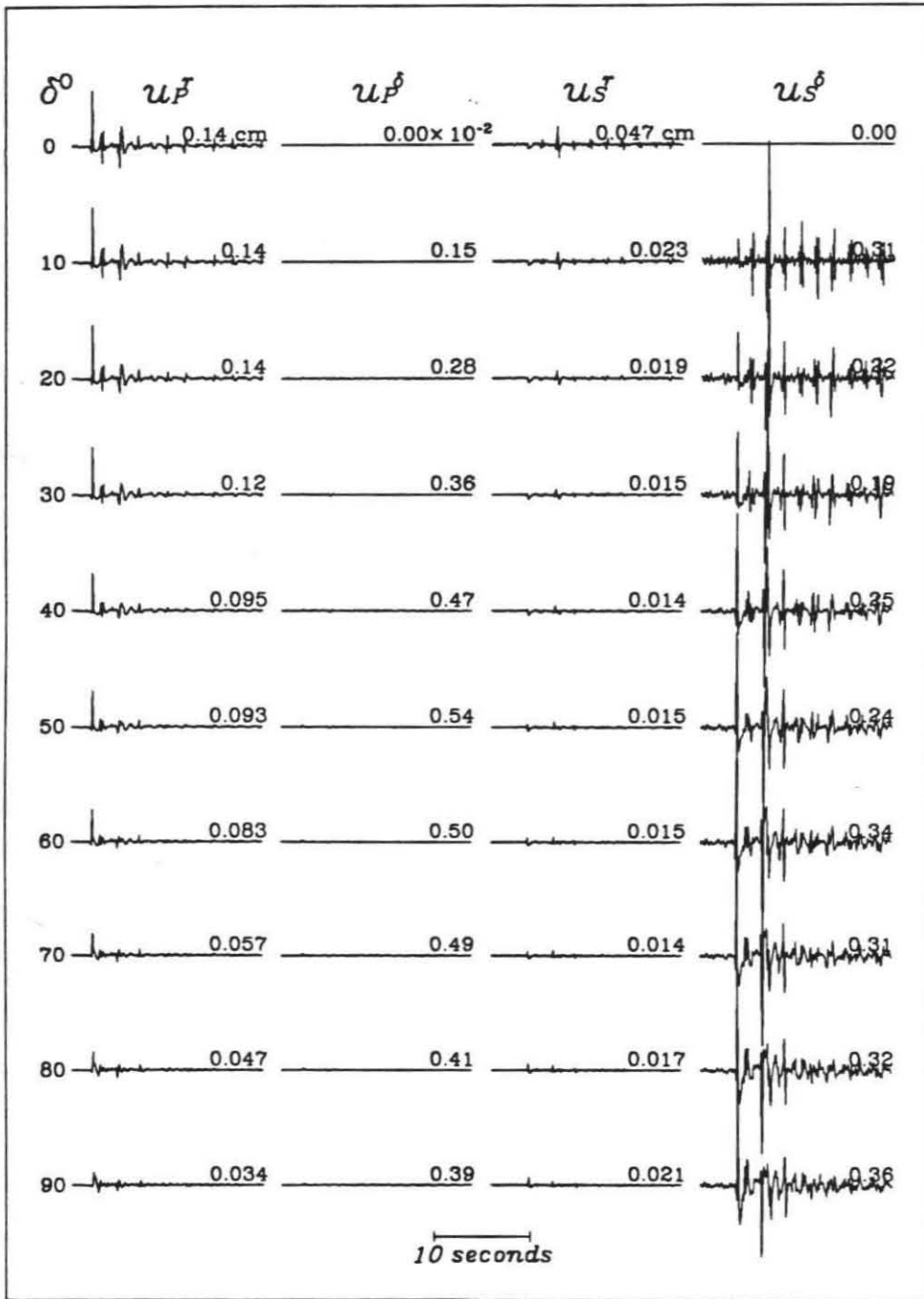
Figure 6. Wave fields as a function of δ for the standard model. δ ranges from 0 to 90°.

In Figure 7, we show the results for different sizes of the elastic sphere. The source radius is kept at the same fraction of the sphere's radius as in previous cases, i.e., r_0 is $0.9a$. The fourth row in the figure is the same as the last row in Figure 6 since the radii and source-receiver angles are the same, i.e., 0.5 km and 90°. Most of the observed effects can be explained by noting that increasing the radius under these conditions is similar to decreasing the velocity. Thus we expect time differences between arrivals to increase and a decrease in frequency content as the radius increases.

Figure 8 displays the radial components of the P waves on the symmetry axis for different source radii with $\delta{=}0$, i.e., source and receiver on the same side of sphere center and 180°, i.e., opposite sides. The distance used is 10 km from the source while in previous figures the receiver was 10 km from the sphere center. If the source is located at the center of the solid sphere, the wave fields for $\delta{=}0$, and 180° are of course identical. The numerical evaluation of the analytical solution was shown in Figure 2. As the source is moved toward the boundary of the sphere, the early arrivals separate and diminish in amplitude for $\delta{=}0$. For $\delta{=}180°$, they converge and grow in amplitude as the source passes through an effective focus in the sphere and then decrease in amplitude as the source is moved closer to the boundary.

In Figure 9, we keep the dimensions and source-receiver angles the same as Figure 8 but vary the sphere elastic properties using the same relationship between velocities and densities as before. The source radius is 0.45. The first row is the radial P wave field for velocities and density, which are the same as the previous figure. They can be considered an
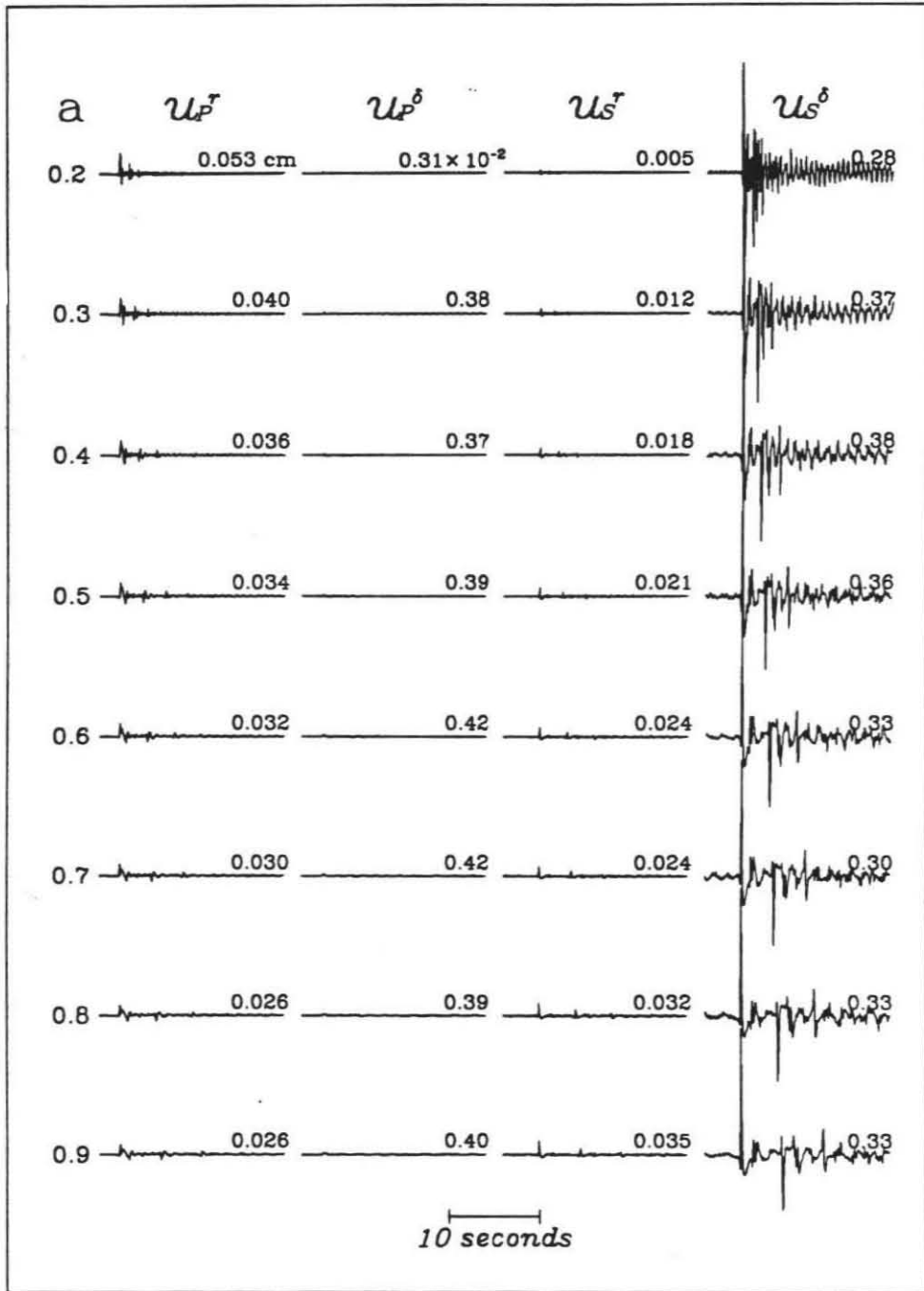
Figure 7. Wave fields for different radii, 0.2 - 0.9 km, of the embedded sphere.
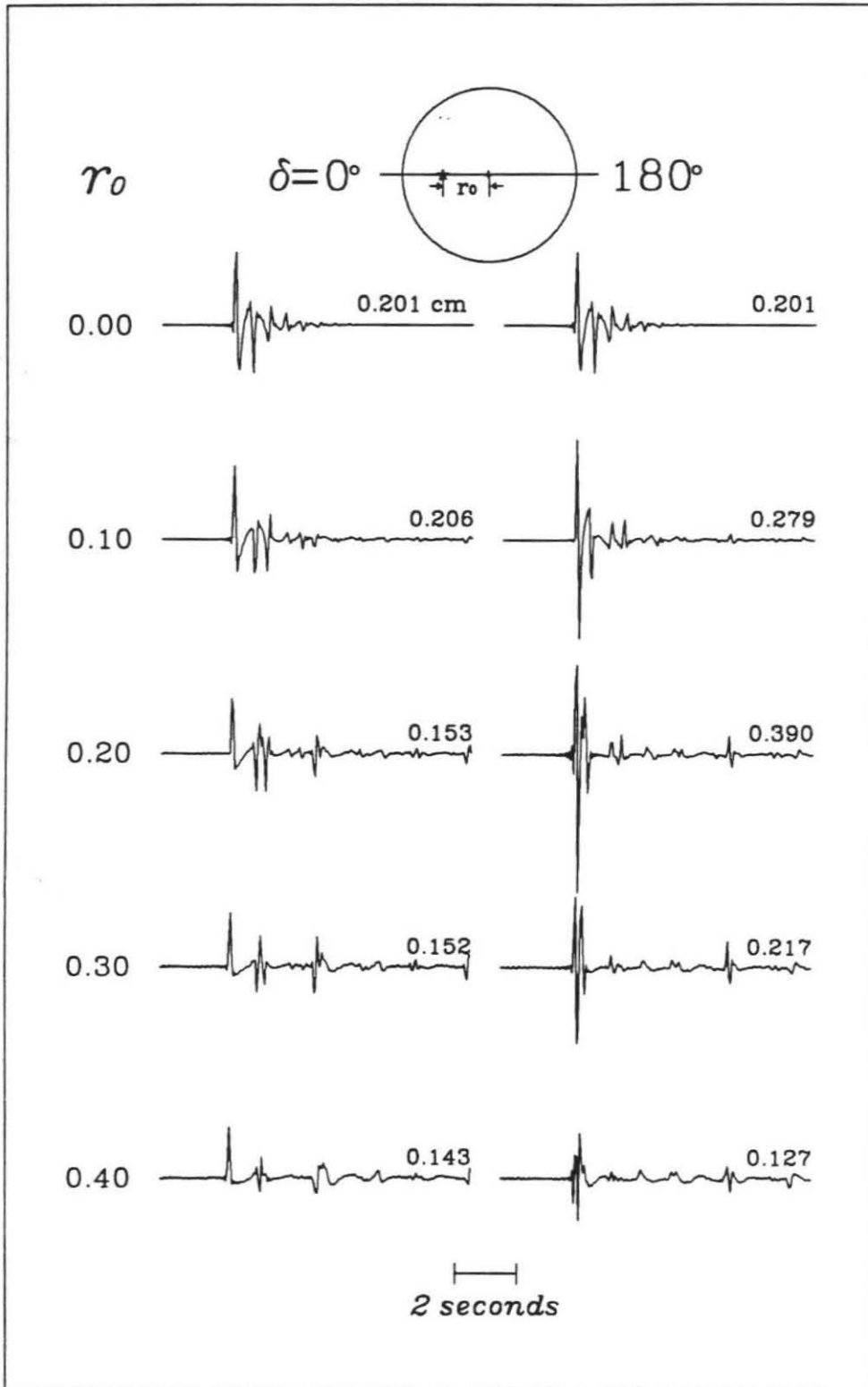
Figure 8. Radial components of P waves at $\delta=0$ and $180°$ for the different source locations. In the cartoon of the sphere at the top, the star indicates the source.
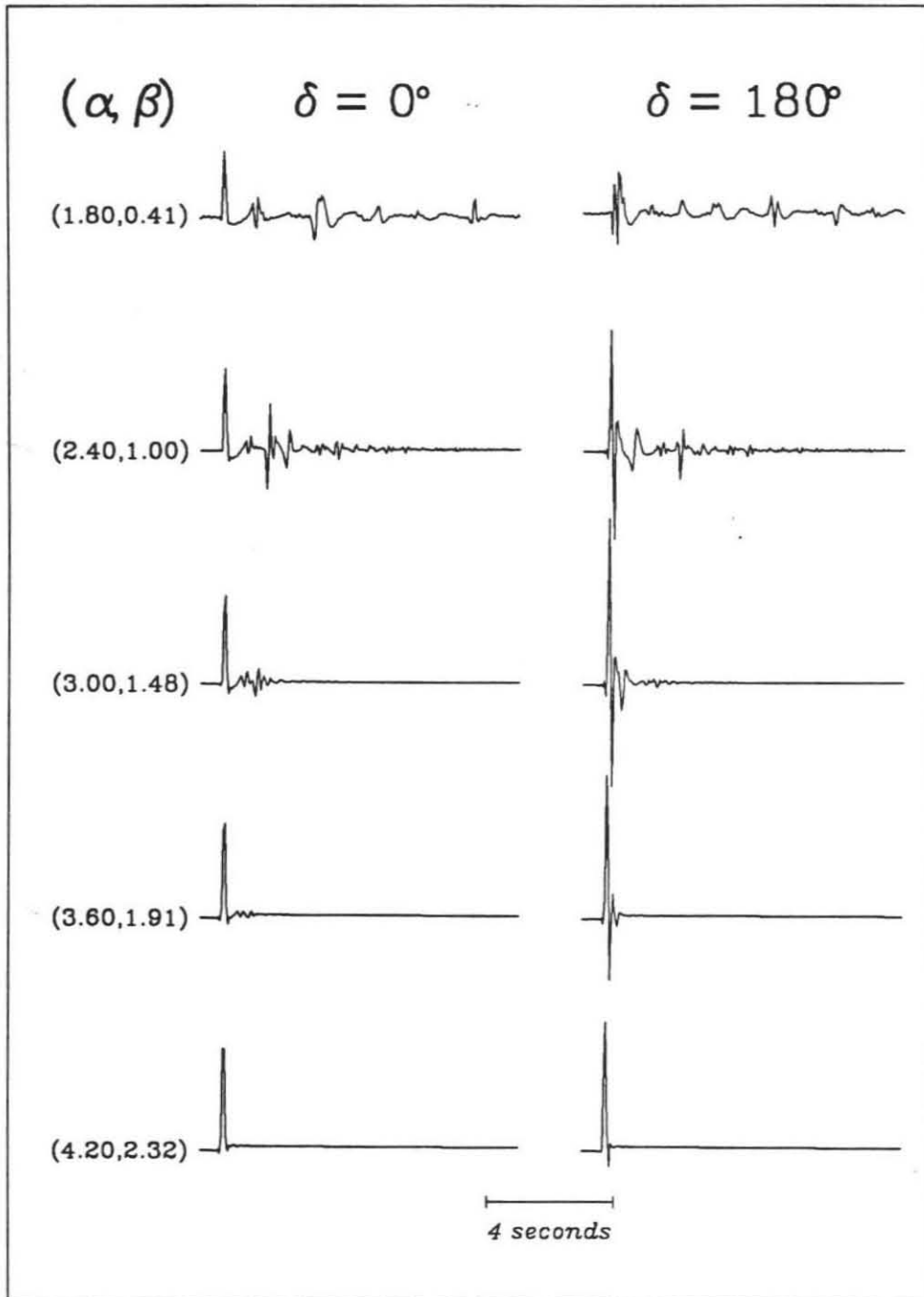
Figure 9. Radial components of P waves at δ=0 and 180° for different P and S velocities and density in the sphere.

additional row to the previous figure with the source radius increased from 0.4 to 0.45 km. All traces on this figure are on a common scale in order to demonstrate the increase in amplitude of the early arrivals at $\delta=0^o$ and the reduction in amplitude of the later arriving S coupled internal reflections at both receiver positions as the velocities and density of the sphere are increased to that of the whole-space. The whole-space result is only slightly larger than the $\delta=0^o$ trace on the bottom and of course smaller than the $\delta=180^o$ bottom trace. The effect of decreasing the impedance contrast and of reducing the travel time for reflections in the sphere reduces the partitioning of direct P into later arrivals. The increase in moment while keeping $\Psi(\infty)$ constant as we go down the rows seems to have only a minor effect on the direct P amplitude. It is notable that the largest amplitude of direct P is in the middle rows where the elastic contrast is intermediate and in the receiver direction where the path is longest in the sphere, i.e., $\delta=180^o$. This is due to the source being near the focus which changes position relative to source point as we change velocities. This is similar to the previous figure where we moved the source relative to the fixed focus.

With the exception of Figure 6, we have investigated the time histories at either the long period maxima for the S waves, ie $\delta=90^o$ or at the P wave maxima, i.e., $\delta=0^o$ or 180. Even in Figure 6, δ ranged only from 0 to 90°. In the next three figures, we show the radiation pattern for P and S at periods of 1 and 20 seconds as a function of source radius, elastic parameters and radius of the sphere. The periods were chosen for their obvious significance to seismic magnitudes. The asymmetry of the source region is

seen to have significant effects on short period radiation patterns, but to have only minor effects on the long period.

Figures 10, 11 and 12 show radiation patterns for different configurations. "P" and "S" in these figures denote the radial component of P waves and the δ component of S waves respectively. The distance used for these calculations is 1000 km to void the near-field contributions. The source is on the horizontal line for all these figures. The direction of δ is indicated on the diagram of the sphere at the top of Figure 10 with a star marking the source. The sphere center is shown as a "+" in all the radiation patterns. The dashed circles with the same centers as the P radiation patterns are the P wave radiation pattern for the source located at the center for the particular model and demonstrate the amplitude effect due to source asymmetry. The dashed line part of the S wave radiation pattern indicates negative amplitude compared to the solid line. In this case positive indicates a clockwise displacement and negative is counter clockwise. The number at the right hand side of the S wave radiation pattern is the multiplyer of the S wave pattern used to plot on the figure, i.e., the larger the number the smaller the actual pattern compared to other S wave patterns on the figure and the P wave pattern next to it.

Figure 10, using the standard model, shows the radiation patterns for different source locations, r_0. Figure 12 uses the same elastic model but different radii of the solid sphere. In Figure 11, the sphere's elastic parameters are varied in the inverse order to Figure 9. Similar effects are seen in all three numerical experiments. As the source radius is increased, the elastic
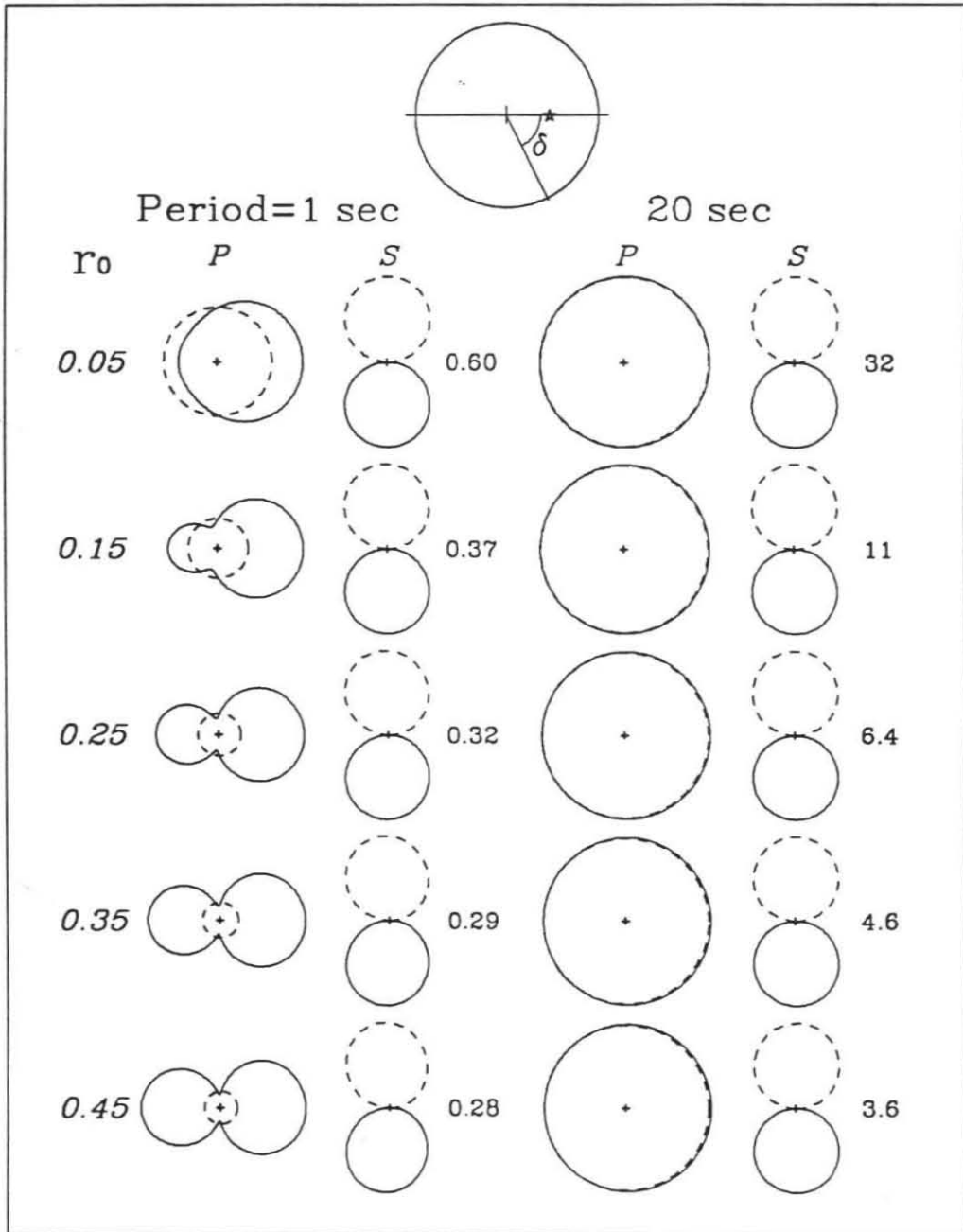
Figure 10. Spectral radiation patterns at periods of 1 and 20 seconds for different source locations. "P" is for the radial component of P waves, "S" is for the δ component of S waves. On the cartoon of the sphere at the top, the direction of δ is indicated. The star indicates the source. "+" is the center. Dash circles with the same centers as the P radiation patterns are the P wave radiation patterns for a source located at the center. The numbers on the right of the S wave radiation patterns are the multicative factors used to adjust the the size of S wave radiation patterns for comparison with the corresponding P wave radiation patterns in the figure.
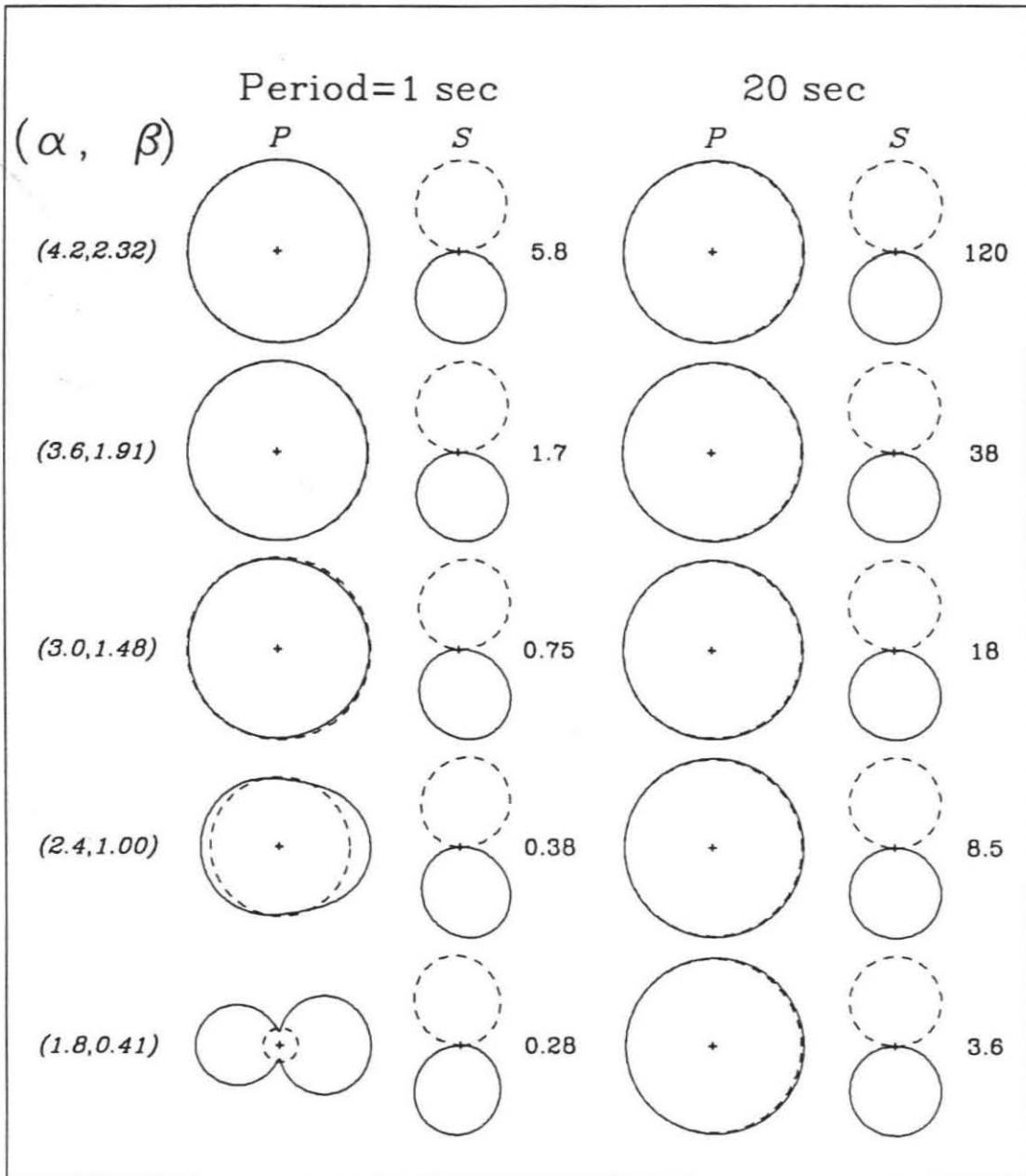
Figure 11. Spectral radiation patterns for different elastic media of the embedded sphere.
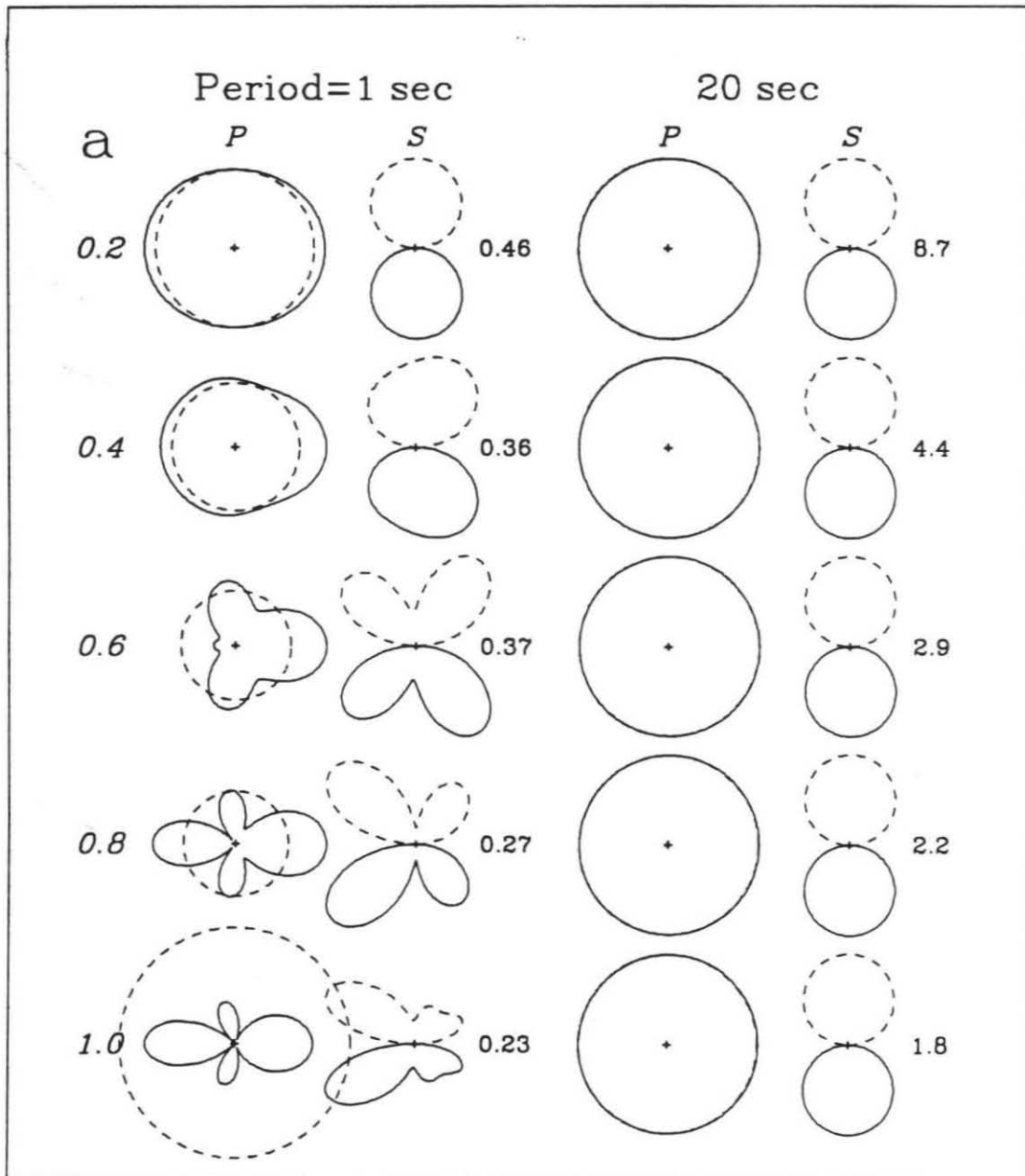
Figure 12. Specral radiation patterns for different radii of the elastic sphere.

parameters of the sphere are decreased, or the sphere radius is increased, the radiation patterns become more asymmetric. In other words, the P wave radiation becomes less spherical and the 20 second S wave pattern, which is essentially the radiation pattern for a point force pointed away from the source, becomes larger. From these figures, we also see that the intensity of the P waves radiated by an off-center explosion is greater than that by the corresponding center explosion with the same $\Psi(\infty)$ except in Figure 12 where increasing the source and sphere radius beyond the dimensions of the standard model, the opposite is true. Also by comparison within each row, we can see that S wave generation is much smaller and that the P wave fields are closer to the excitation of a center explosion for longer periods than for shorter periods.

An interesting feature is the shape of the radiation patterns at short periods. For the P wave in Figures 10 and 11, we see that the radiation pattern is similar to a dipole. The radiation patterns are reminiscent of those of far-field P and S waves scattered from localized inhomogeneities when plane P waves are incident (Aki and Richards, 1981, pg. 732). This should not be surprising since in our case the incident wave is a spherical P wave interior to the scatterer. In comparing the Aki and Richards figure with ours, one must remember that our P wave radiation patterns include the transmitted spherical wave perturbed by the scattering or asymmetric contribution where theirs is only the scattered wave.

Another interesting feature in all three figures is that the maximum long period 20 second P wave amplitudes are at least twice (≈ 1.8) as large

as the corresponding maximum S wave amplitudes for all cases calculated. This is in agreement with the empirical formula for explosions in axisymmetric cavities of Rial and Moran (1986). But because their sources were in the symmetry center of the cavity, the resulting S wave radiation was more like a dipole than a point force at low frequencies.

In Figure 13, we investigate the error introduced if we estimate the moment by using a finite time length which may include only the initial few pulses. The synthetics in Figure 13 are calculated for our standard velocity and density model keeping only $1/r$ terms, i.e., the far-field approximation. The distance used is 10 km from the center. The top trace is the response of a centered explosion; the lower one is the response of an off-center explosion. The source is 0.45 km from the center of the sphere and the angle,δ, between the source and receiver is 45°. From the long period P wave radiation patterns, we know that the angle is irrelevant as long as we are interested in moment. The moment is calculated from the area using the zero frequency spectra and corrected from "observed" to actual moment by equation (10). From the figure, the longer the time interval we use, the better the estimate we get. The first few pulses hold more than 80 percent of the moment in these two examples. Even though the first pulse holds about 90 percent of the moment, in a real situation it would be difficult to separate the effect of local reverberation. In this case, if we take a long enough window, the reverberations finally die down and we get a good estimate.

Figure 14 shows M_{obs}/M_0 as a function, equation (10), of the sphere compressional velocity,α_1, for different values of the whole-space compression
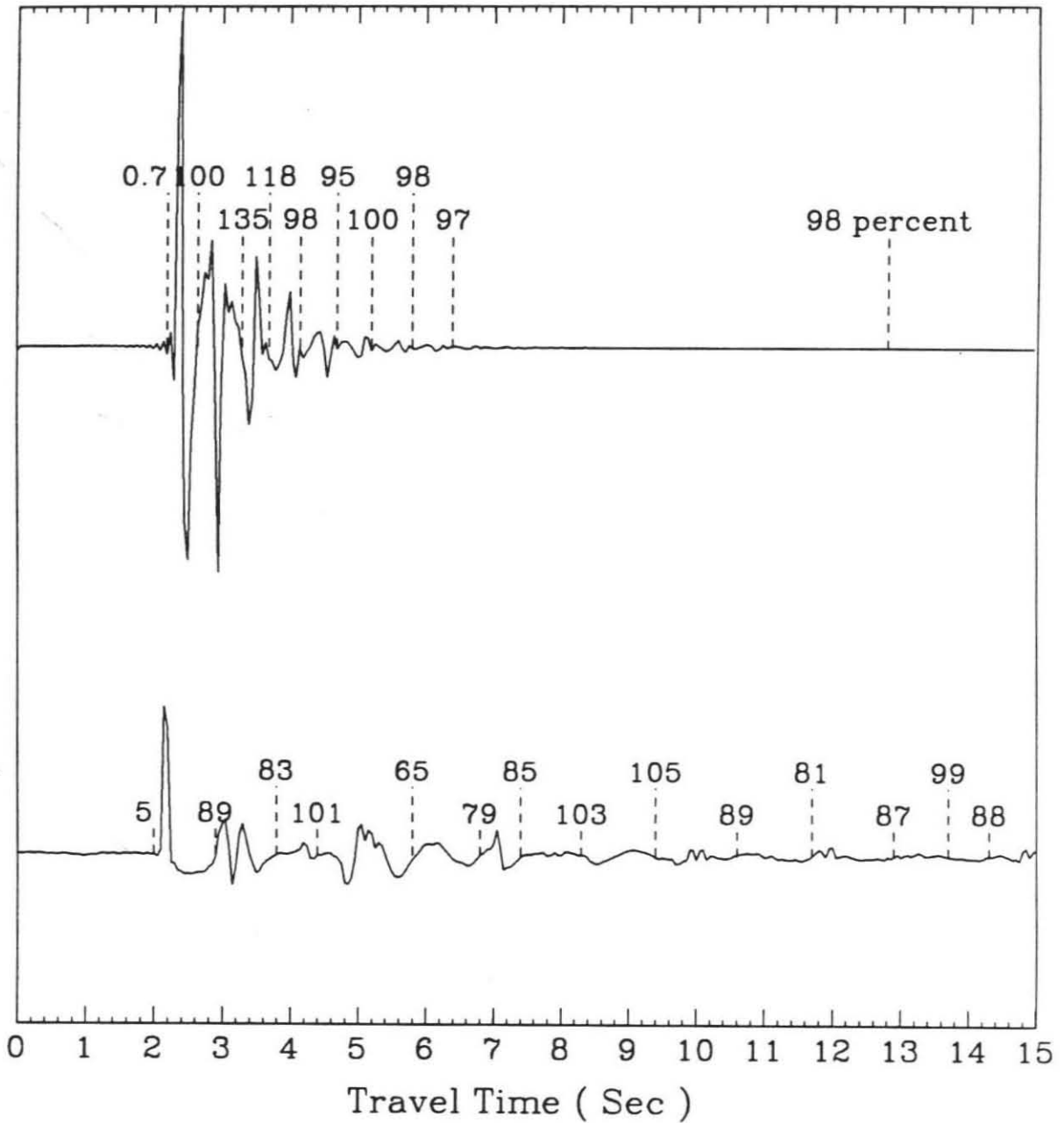
Figure 13. Moment estimates as a function of record length. The numbers are the percentage of estimated moment to input moment obtained using the time length from the beginning to the dash line mark on the record below the number. The upper trace is the seismogram of a centered explosion. The lower one is the seismogram of an off-center explosion. Detailed parameters are given in the text.
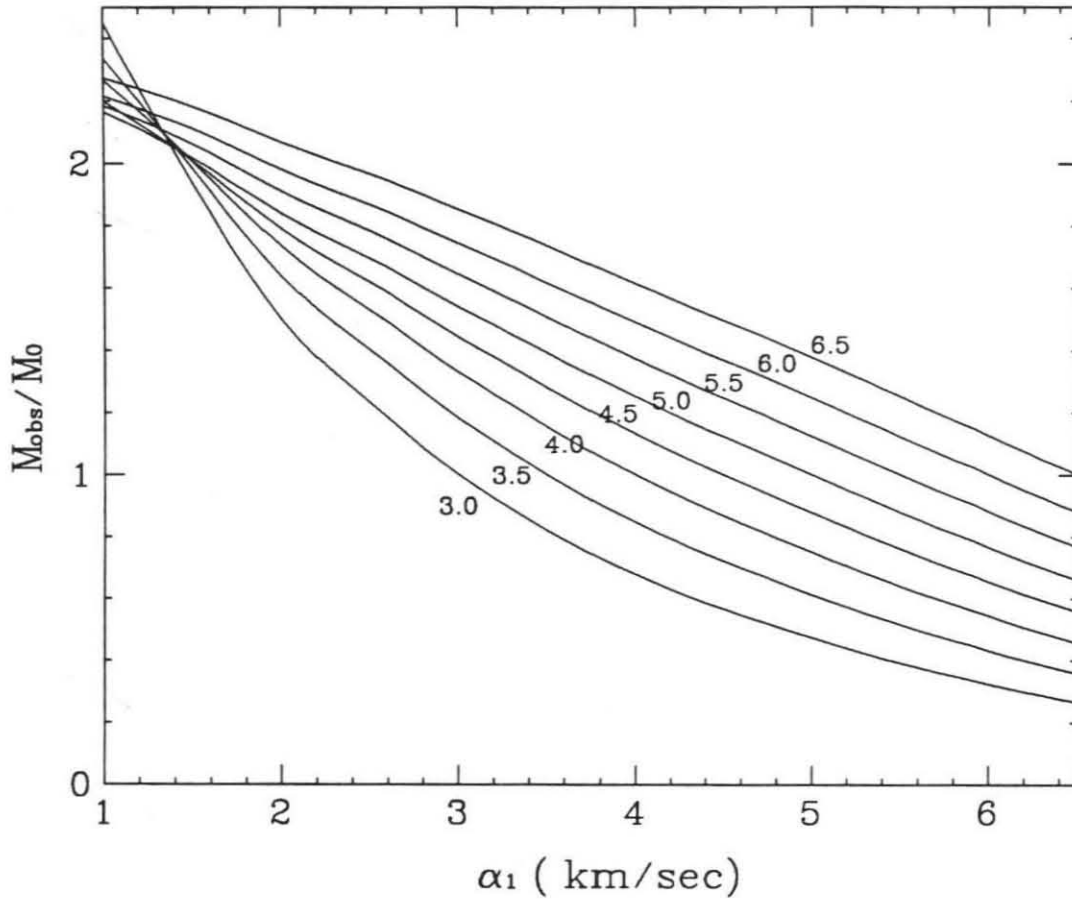
Figure 14. Ratio of the observed moment to the input source moment, M_{obs}/M_0, as a function of the compressional velocities α_1 of the embedded sphere for different whole-space velocities, α_2, assuming Nafe's velocity-density relation.

velocities, α_2, assuming Nafe's velocity-density relation. For exterior velocities greater than those of the sphere, the "observed" moment M_{obs} is greater than the input M_0. And for velocities less, the opposite is true.

How and to what degree the energy for a given explosion is converted into seismic energy is beyond the expertise of the authors. We also do not know whether seismic moment or $\Psi(\infty)$ is the least effected by the physical properties of the shot point material and thus best characterizes an explosion of a given yield. For the numerical results given above, we have kept $\Psi(\infty)$ constant and thus moment has varied as we changed the shot point medium. This was done for convenience and does not express an opinion on "seismic coupling".

CONCLUSIONS

In this study, we gave the analytical formulae for the wave fields from an off-center explosion in an embedded sphere. Numerical calculations were compared with the known analytic solutions. We also calculated P and S wave fields for different r_0, the source distance to the center (Figure 4), for different sphere materials (Figure 5), for different azimuths, δ (Figure 6), and for different sphere radii (Figure 7). The degree of media contrast and the asymmetry of the source determined the size of S wave generation. For the most extreme case investigated, we found that the maximum S wave amplitude in the time domain is almost 3 times the maximum P wave amplitude and is more than 50% greater than the P wave amplitude for the center explosion. Before extrapolating these time-domain results to more realistic

environments, one must remember that this is a very high frequency source with a contribution to the far-field displacement, which is essentially flat in frequency.

In the frequency domain the asymmetry of the source region has significant effects on the radiation patterns of short period, but has only minor effects on that of long period. We also found that the the maximum long period P wave amplitude was at least a factor of two greater than the S wave maximum amplitude for our models. We also investigated the amount of moment error caused by using a finite time window. With care one can obtain meaningful estimates using only a short duration which contains relatively few pulses. Since the moment relation, which is obtained in the limit of zero frequency, is independent of the source location in the sphere and does not involve the geometry or dimensions of the sphere, we infer that it probably holds for embedded homogeneous source regions of any shape.

The long period SH wave radiation, which would be generated if the symmetry axis is in the horizontal, has a dipole radiation pattern. This is not the quadrupole radiation pattern proposed for known underground test sites.

ACKNOWLEDGMENTS

REFERENCES

Aki, K. and P. G. Richards (1980). *Quantitative Seismology: Theory and Methods*, W. H. Freeman, San Francisco, California.

Aki K. and Y. B. Tsai (1972). Mechanism of Love-wave excitation by explosive sources ,*J. Geophys. Res.*, **77**, 1452-1475.

Ben_Menahem, A. and A. G. Sena (1990). The elastodynamic Green's tensor in an anisotropic half-space, *Geophys. J. Int.*, **102**, 421-444.

Ben-Menahem, A. and S. J. Singh (1981). *Seismic Waves and Sources*, Springer-Verlag, New York.

Dubrovskiy, V. A. and V. S. Morochnik (1989). Nonstationary scattering of elastic waves by spherical inclusion, *Izvestiya, Earth Physics*, **25**, 679-686.

Glenn, L. A., A. J. C. Ladd, B. Moran, and K. A. Wilson (1985). Elastic radiation from explosively-loaded ellipsoidal cavities in an unbounded medium, *Geophys. J. R. astr. Soc.*, **86**, 231-242.

Glenn, L. A., B. Moran, A. J. C. Ladd, K. A. Wilson and J. A. Rial (1986). Elastic radiation from explosively-loaded axisymmetric cavities, *Geophys. J. R. astr. Soc.*, **86**, 119-136.

Harkrider, D. G., J. L. Stevens and C. B. Archambeau (1992). Theoretical Rayleigh and Love waves from an explosion in prestressed source regions. Submitted to *Bull. Seis. Soc. Am.*.

Ludwig, W. J., J. E. Nafe and C. L. Drake (1970). Seismic refraction, in *The Sea*, edited by A. E. Maxwell, **4**, Part I, 53-84, Wiley-Interscience.

Mandal, B. and M. N. Toksoz (1990). Computation of complete waveforms in general anisotropic media - results from an explosion source in an

anisotropic medium, *Geophys. J. Int.*, **103**, 33-45.

Pao, Y.-H. (1978). Betti's identity and transition matrix for elastic waves, *J. Acoust. Soc. Am.*, **64**, 302-310.

Pao, Y. H. and C. C. Mow (1973). *Diffraction of Elastic Waves and Dynamic Stress Concentrations*, Crane, Russak and Co., New York.

Press, F. and C. B. Archambeau (1962). Release of tectonic strain by underground nuclear explosions. *J. Geophys. Res.*, **67**, 337-343.

Rial, J. A. and V. F. Cormier (1980). Seismic waves at the epicenter's antipode, *J. Geophys. Res.*, **85**, 2661-2668.

Rial, J. A. and B. Moran (1986). Radiation patterns for explosively-loaded axisymmetric cavities in an elastic medium: analytic approximations and numerical results, *Geophys. J. R. astr. Soc.*, **86**, 855-862.

Thompson Jr., W., (1973). Acoustic radiation from a spherical source embedded eccentrically within a fluid sphere, *J. Acoust. Soc. Am.*, **54**, 1694-1707.

Varatharajulu, V. and Y.-H. Pao (1976). Scattering matrix for elastic waves. I. Theory, *J. Acoust. Soc. Am.*, **60**, 556-566.

Waterman, P. C. (1969). New formulation of acoustic scattering, *J. Acoust. Soc. Am.*, **45**, 1417-1429.

Waterman, P. C. (1976). Matrix theory of elastic waves scattering, *J. Acoust. Soc. Am.*, **60**, 567-580.

Zhao L.-S., D. V. Helmberger, and D. G. Harkrider (1991). Shear-velocity structure of the crust and upper mantle beneath the Tibetan Plateau and southeastern China, *Geophys. J. Int.*, **105**, 713-730.

PART II

Seismic Waveform Modeling of Regional Phases

CHAPTER 2

Broadband Modeling Along a Regional Shield Path, Harvard Recording of the Saguenay Earthquake

ABSTRACT

The Saguenay earthquake, November 25, 1988, is one of the first large shield type events recorded by a broadband - high dynamic range instrument, the Streckeisen system, installed at Harvard station (HRV). The event is sufficiently large enough to be well recorded teleseismically and thus the source characteristics can be determined by independent means and considered known. This allows a detailed study of the propagational effects along this path, at an epicentral distance of 625 km, where the strengths of the surface waves can be compared with the crustal body phases. Broadband modeling using standard analytical techniques and flat layered models works amazingly well over the period range of 0.5 to 20 seconds. A detailed strategy for modeling broadband regional phases is given in terms of a decomposition of the vertical and radial seismograms into three segments: P_{nl} (containing P_n, pP_n, sP_n, P_mP, P coupled PL waves) ; S_{nl} (containing S_n, sS_n, S_mS, etc.) ; and the fundamental Rayleigh waves. Information about the upper crust is obtained from the fundamental Rayleigh waves

while crustal thickness and velocity gradients in the mantle are obtained from P_{nl} and S_{nl}. This particular crustal model has a thickness of 35 km with a sharp Moho and a substantial gradient in the top 20 km of the mantle, 0.01 km/sec per km for both P and S velocities. The mantle velocities, α=8.2 and β=4.55 km/sec are slower than expected for a shield environment. Attenuation is not required for waveform modeling or for absolute amplitude estimation.

INTRODUCTION

In recent years, short-period seismology has concentrated on small events and local crustal structure while long-period seismology has concentrated more on inverting source mechanisms of larger earthquakes and deep earth structure. Long period seismograms at regional distances have not received much attention in either source studies or in studies of the Earth's shallow structure. One reason is that only small events, $4<m<5$, remain on scale on the standard long-period WWSSN at these distances. The source properties of these events are generally poorly understood, since they can not be easily studied teleseismically. Thus, these events are not so useful in Earth structure investigations. Larger events produce visible P_n and PL waves and these waveforms have been used in earthquake studies (e. g. Helmberger and Engen, 1980; Wallace and Helmberger 1982), but the surface waves of the events go off-scale. Most digital systems have, unfortunately, not performed well at regional distances for assorted reasons.

With the installation of the Streckeisen seismometer and high dynam-
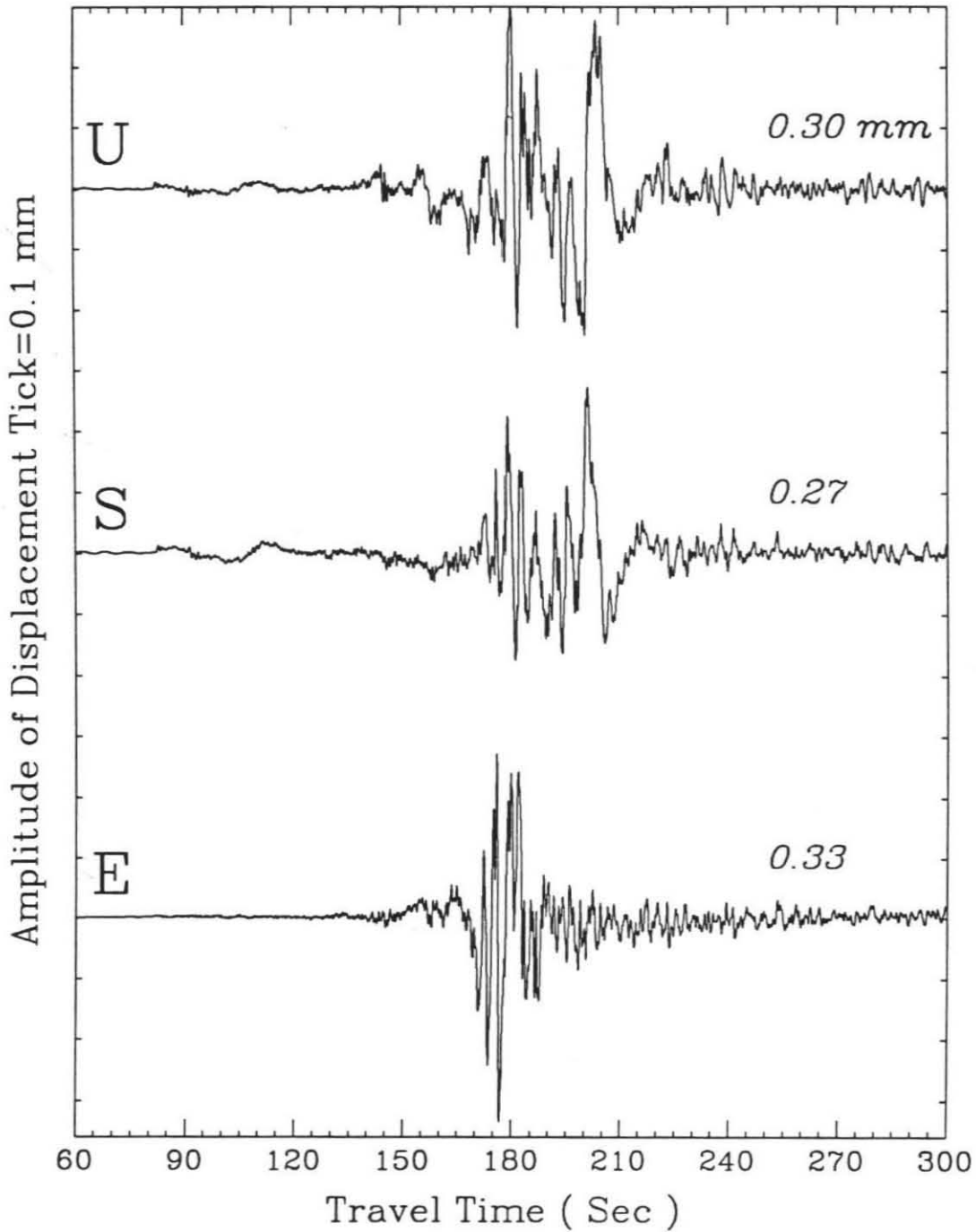
Figure 1: The Broadband displacement data recorded by Harvard station (HRV) of the November 25, 1988 Saguenay earthquake. The first trace is vertical component, where upward is positive; second trace is radial component, positive southward; and the third trace is tangential component, positive eastward. The numbers on the right are the maximum amplitudes in *mm*. The instrument response is flat in velocity between 0.0027 Hz to 7 Hz. Integrating within this band produces the displacement records displayed.

ic range digitizer, the broadband nature of regional phases can now be appreciated (see Figure 1). The HRV recording of the Saguenay earthquake, at an epicentral distance of 625 km, is one of the first such unclipped recordings of a sizable earthquake occurring in a predominantly shield region. This event is the largest earthquake to occur in over 50 years in Eastern North America and was recorded both locally and teleseismically (e. g. North et al., 1989; and Somerville et al., 1989). These studies provide seismic source parameters for the event (strike $=323°$, dip $=65°$, rake $=78°$, moment $=5.0\times10^{24}$ dyne-cm, depth $=28$ km), as well as some constraints on the time history.

Figure 2 gives the three component long-period WWSSN recordings obtained by convolving the broadband data displayed in Figure 1 with the WWSSN instrument response. The peak to peak amplitude of the Rayleigh wave is about 1.1 meters. If the gain of the instrument is taken as the average WWSSN (2250), the Rayleigh wave goes off-scale on conventional records. The first 40 seconds of these records is controlled by the $(P-SV)$ system. This wavetrain begins with P_n and evolves into PL and has been called P_{nl} (Helmberger and Engen, 1980). The later arriving phases begin with S_n, sS_n, etc. and go off-scale somewhere near the direct S arrival. The beginning portion of this group which arrives before the fundamental Rayleigh wave will likewise be called S_{nl} for convenience.

Figure 3 displays a comparison of the broadband data and synthetics constructed from a flat-layered model. A brief comparison of these waveforms indicates that quantitative methods based on layered models
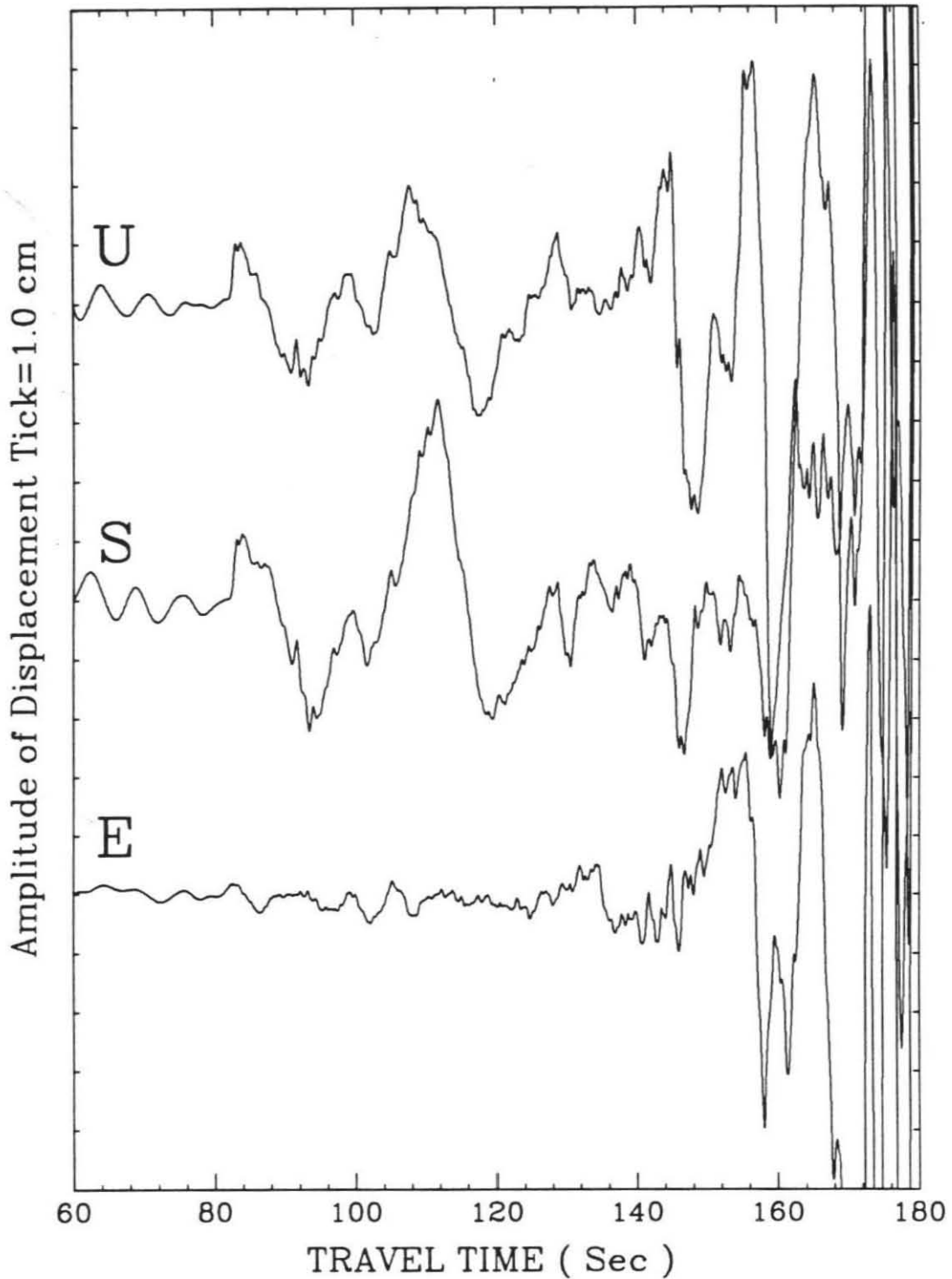
Figure 2: The broadband data convoluted with the WWSSN long - period instrument response. These would be the real long period record with a gain of 2250. The three components are the vertical, radial and tangential. The letters on the left indicate the positive directions.
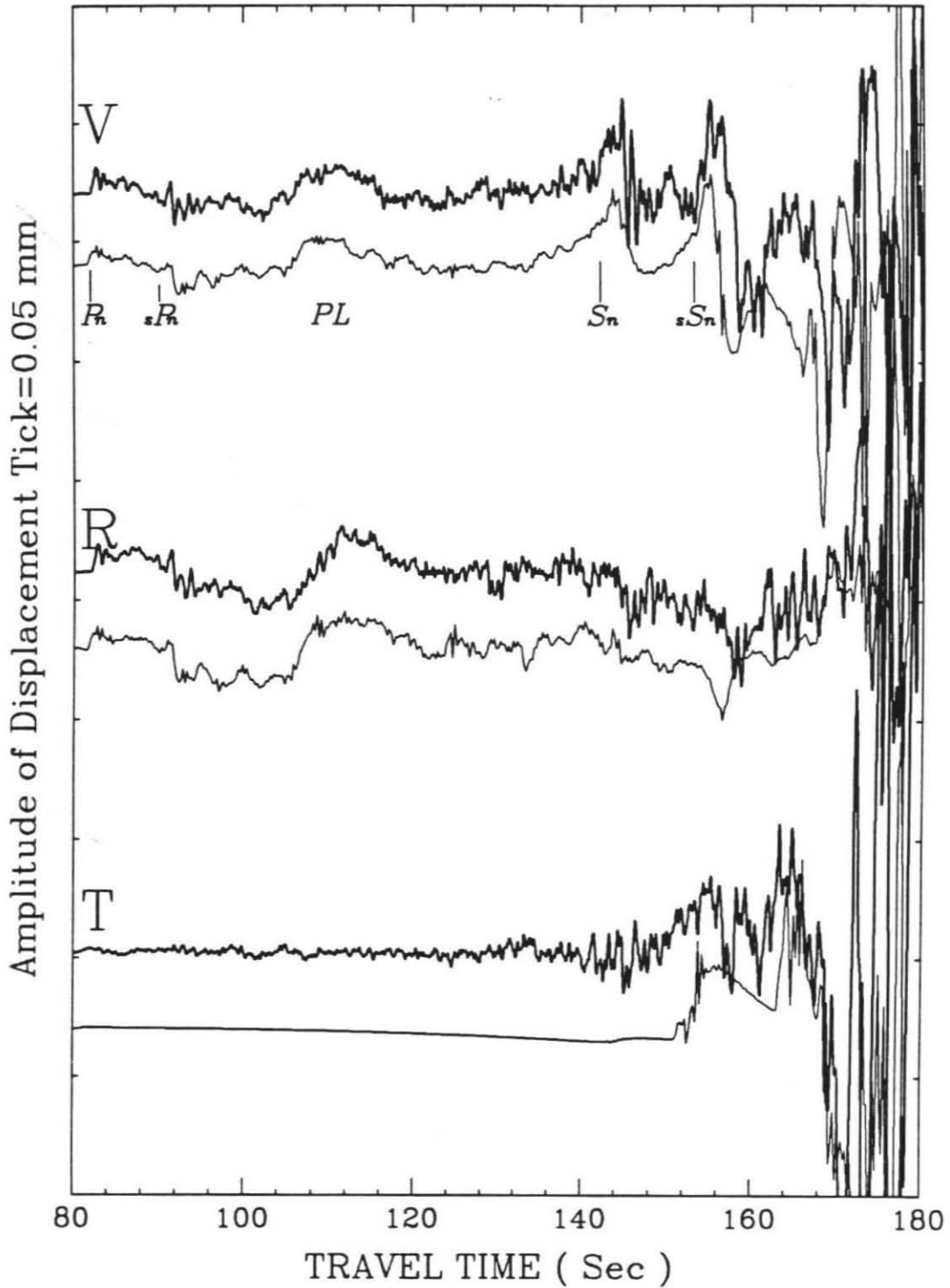
Figure 3: This figure displays the first hundred seconds of the broadband waveform data along with the synthetics generated by a flat-layered model found in this study. The main phases such as P_n, sP_n, and PL, S_n, and sS_n are labeled.

work quite well, at least in a shield environment. This chapter addresses some techniques and strategies which were used in deriving the above model along with numerous sensitivity studies. What can be learned from regional broadband seismograms is our main concern in this study.

NUMERICAL METHODS

There are many different techniques available for generating synthetics for a flat-layered model (see Aki and Richards, 1980 for example). The reflectivity method (Mallick and Frazer, 1988) and various modifications essentially perform a double integration and produce accurate results if the integration windows are properly placed with respect to the range of ray parameter and frequency. This technique lends itself to vectorization and looks more attractive than the other methods with the availability of vector computers. Comparison of synthetics generated with this approach and with generalized rays (Helmberger, 1983), has been discussed by Apsel and Luco (1983) for simple models where it is possible to sum enough rays to construct the entire wavefield. The advantage of rays is that insight can be gained into the timing of individual pulses. However, in strong waveguides the number of significant multiples become large and the method becomes impractical. Fortunately, the normal mode method or mode summation method (Harkrider, 1964) works well for modeling surface waves at about this time window, as we discuss next.

In this study, the earthquake will be represented by a simple point source dislocation, which can be computed by constructing a linear combina-

tion of responses for pure strike-slip, dip-slip and 45° dip-slip sources, as discussed by Helmberger and Harkrider (1978). Synthetics of these three types of source descriptions are displayed in Figures 4 and 5, where the generalized ray results are compared with those of reflectivity and the normal mode method. The model used is the same as that considered by Apsel and Luco (1983), in their study of the various methods of generating synthetics. The bottom traces display P_n, P_mP and direct P, followed by pP_s , pP_mP and sP_s , etc. A similar set of S phases occurs near the surface waves, which appears to be included in the mode solution and produce synthetics in good agreement with the ray solution. It is difficult to prove theoretically that the direct S-arrivals and multiple reflected S phases are handled properly in the modal approach because of the neglect of head waves. Although the amplitudes predicted by reflectivity and rays differ somewhat, the waveforms predicted by them are almost identical. The differences in amplitudes are caused by an assortment of analytical approximation in each individual method, however, in this particular application it appears to produce accurate enough results for our purposes. The locked mode approach (Harvey, 1981) could be used to construct the entire solution but this involves considerably more computing effort. We will use all these methods in this study, exploiting the particular advantages of each as appropriate.

MODELING STRATEGY

Given a stack of 10 layers with 30 parameters, we would predict a synthetic match comparable to that displayed in Figure 3 by letting each
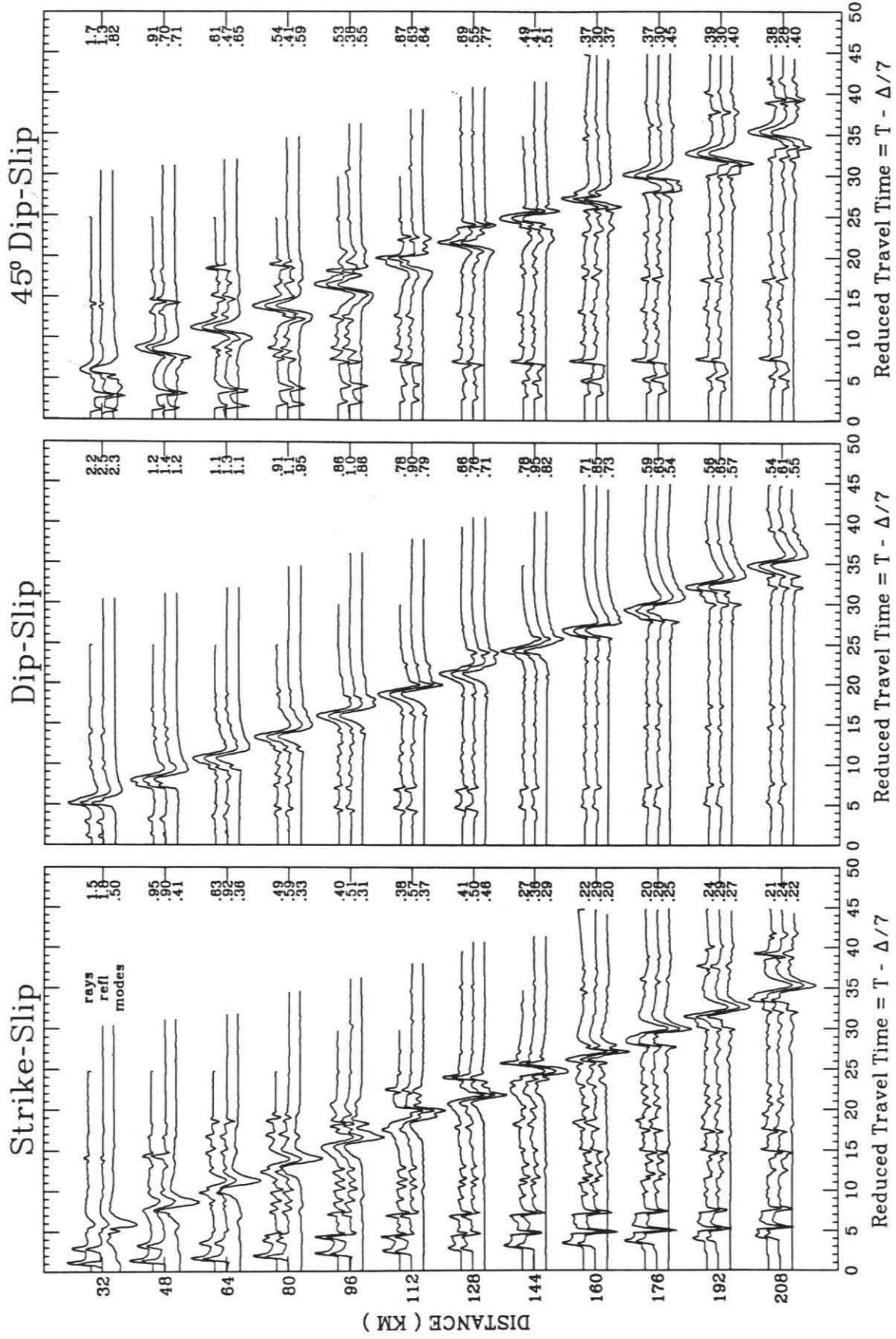
Figure 4: Comparison of the radial components of the synthetics generated by Generalized Ray Method (GRM), " rays" in this figure, reflectivity, refl, and Mode Summation Method (MSM), modes. The numbers on the left are the distances of the three nearest traces. The left column is for the strike slip source; the middle for dip slip source; and the right for 45° dip slip source. The source function is a 0.2 0.2 0.2 trapezoid. The moment is $10^{25} dyne \cdot cm$. The source depth is 8.0 km. The numbers on the right margin of each column are the amplitudes for the corresponding traces in centimeters. The parameters of the model are: $\alpha=6.2 km/sec$, $\beta=3.5 km/sec$, with a 32 km thick crust; mantle velocities are $\alpha=8.2 km/sec$, $\beta=4.5 km/sec$. Mode synthetics include 12 modes. The parameters used for reflectivity synthetics are: decay factor 50, slowness window (0.0-0.5), frequency band (0.0025-5) Hz, $Q_\alpha(80000)$ and $Q_\beta(40000)$.
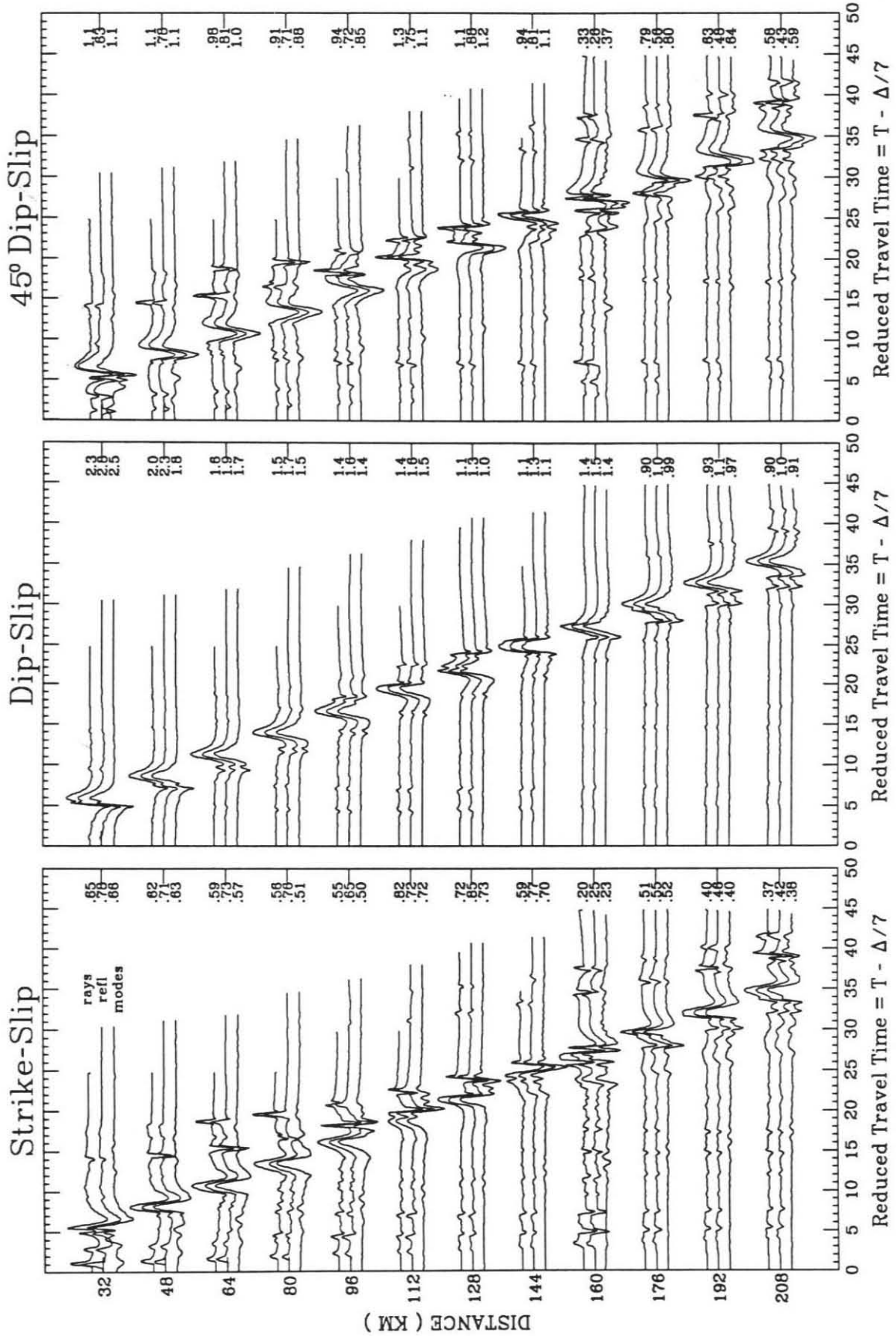
Figure 5: Comparison of the vertical components of the synthetics generated by GRM method, reflectivity and MSM methods. The left is for strike slip source; the middle for dip slip source; and the right for 45° dip slip source.

parameter vary over 10 values. In this section we discuss a strategy of finding a good fitting model without wandering through this large parameter space. Two basic elements are necessary for this strategy to work, namely, broadband signals and the bag of seismological tools just discussed.

The strategy has four stages. First, we model a long-period version of the data assuming a single crustal layer. We find that the long-period P_n and S_n depend only on the upper-mantle velocities and the average properties of the crust. Five parameters are sufficient for initial modeling, that is two velocities in the mantle, two average velocities in the crust, and crustal thickness. These parameters are easily found by mostly timing and identifying particular phases, P_n, S_n, etc. The next stage, we add some layers to the crust with the above constraint to model the fundamental Rayleigh wave.

In the third stage we model the broadband waveforms by adding some upper-mantle structure, which controls the short-period signals riding on top of P_n and S_n, etc. This is achieved by assuming the single layered crustal model and working with rays.

In the fourth stage, we compute complete synthetics using reflectivity for the layered stack and make some final adjustments by trial-and-error. A possible fine-tuning operation, or fifth stage, would involve a formal waveform inversion. We will not perform such an inversion here but we will show a number of parameter sensitivity studies of the models near our preferred model.

a) Long-Period Modeling

The data used in this section contain the WWSSN long-period response, and will be referred to as conventional long-period data. The beginning portion of these records are displayed at the top of the Figure 6, essentially the P_{nl} and S_{nl} wavetrains. Since a layer-over-half space model has proved effective in modeling the P_{nl} portion of these records it is natural to examine the S_{nl} portion assuming the same models and summing generalized rays. Possible models are give in Table 1 with corresponding synthetics displayed in Figure 6. The S_n phase arriving just after 140 seconds, as labeled in Figure 3, appears to be phase-shifted relative to P_n. This is the case, that can be seen by examining the receiver functions describing the vertical (SZ) and radial components (SR) of motion for an incoming SV signal:

$$R_{SZ} = \frac{\eta_\alpha \eta_\beta}{\beta^2 R(p)}$$

$$R_{SR} = \frac{2\eta_\beta(\eta_\beta{}^2 - p^2)^{1/2}}{\beta^2 R(p)}$$

where

$$\eta_\alpha = (\frac{1}{\alpha^2} - p^2)^{1/2}$$

$$\eta_\beta = (\frac{1}{\beta^2} - p^2)^{1/2}$$

$$R(p) = (\eta_\beta{}^2 - p^2)^2 + 4p^2 \eta_\alpha \eta_\beta$$

and where α is compressional velocity, β shear velocity, p ray parameter (Helmberger, 1983). For $p = 1/\beta_n$, the parameter appropriate for the S_n head wave, we obtain

$$R_{SZ} = -0.28i \text{ and } R_{SR} = -0.013 .$$

Table 1 models for Pnl waves

Model	1	2	3	4	5	6	7
α	6.50	6.40	6.40	6.30	6.40	6.40	6.40
β	3.70	3.65	3.70	3.70	3.65	3.70	3.70
Thick	40.0	40.0	40.0	40.0	35.0	40.0	40.0
α	8.10	8.20	8.20	8.20	8.20	8.20	8.20
β	4.70	4.70	4.70	4.70	4.70	4.65	4.68
Thick							

α is compressional velocity, β is shear velocity.
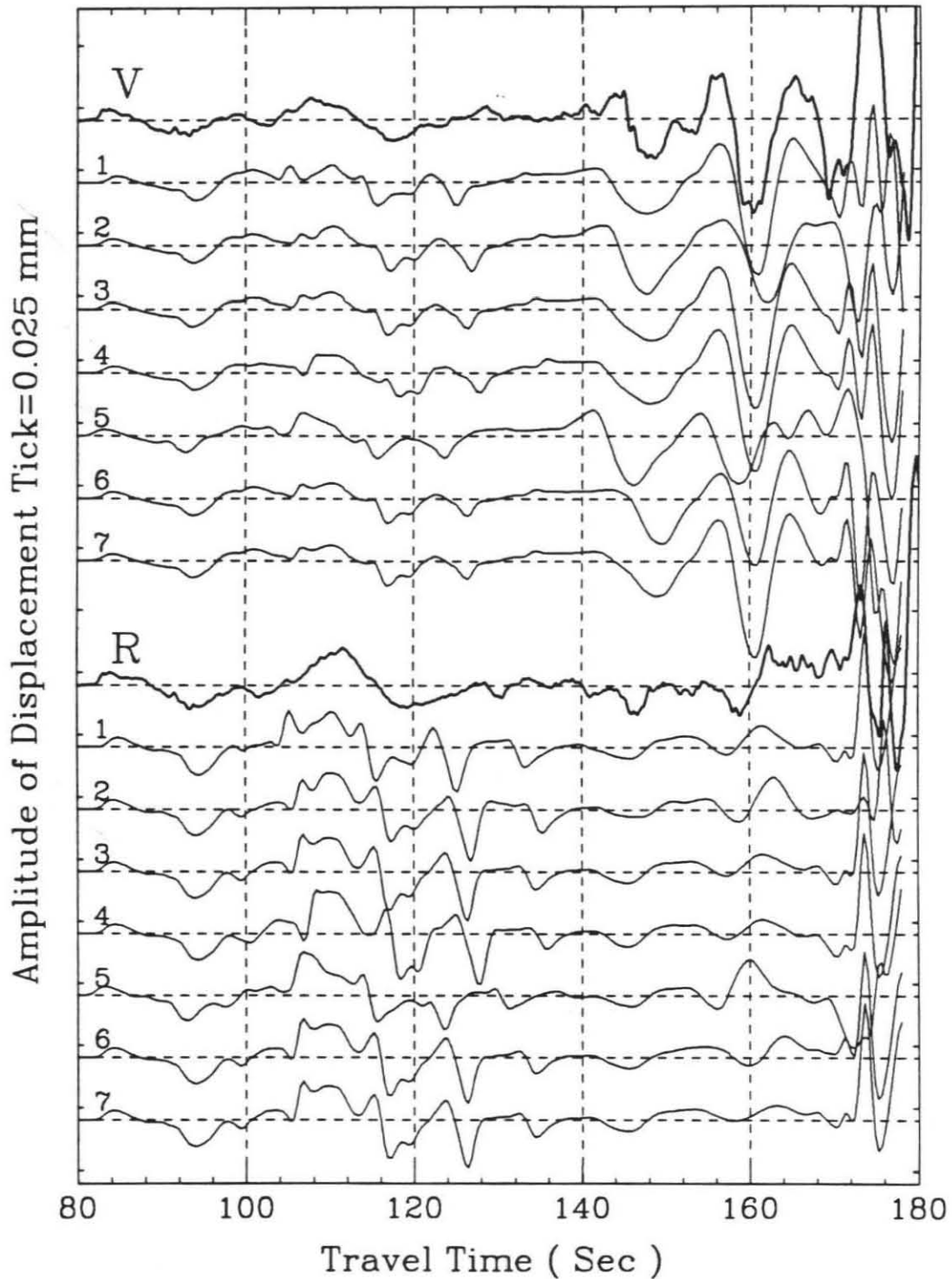
Figure 6: Comparison of the long period P_{nl} and S_{nl} data and the synthetics generated for different models. The upper group of traces are vertical components, the lower are radial components. The models used are given in Table 1. The numbers on the left are the model numbers. The source function is a triangle (1,0,1).

Thus, we expect S_n and sS_a to be much stronger on the vertical component than on the radial component. Since these receiver functions are very sensitive to the station site conditions we would expect to see considerable variation in observed phase shifting from station to station.

Models 2 and 5 predict better fits to radial components, whereas models 6 and 7 do better on the vertical components. Since S_{nl} is the strongest on the vertical component we chose model 7 as a preferred starting model, noting that phase shifts will be expected when we add more layers to the crust.

The best fitting model of the complete long-period seismograms, LPM, is given in Table 3 and contains five layers in the crust yielding the average crustal velocities found in Table 1, Model 7. The synthetic comparison of LPM is given in Figure 7. These synthetics were computed by summing 10 modes and assuming a one-second triangle source function. These synthetics are aligned in absolute time except the tangential component which is shifted 4.5 second to the left, implying a slightly faster SH velocity than SV velocity. Several dozen models were investigated but this particular model explains the timing of most of the phases the best. Note that S_n (SH) is nearly nodal at HRV and, therefore, any source complexity or errors in mechanism produce strong changes in the synthetics. For this reason we have concentrated our efforts in fitting the more stable ($P-SV$) system where the source can be assumed known.

b) Broadband Modeling
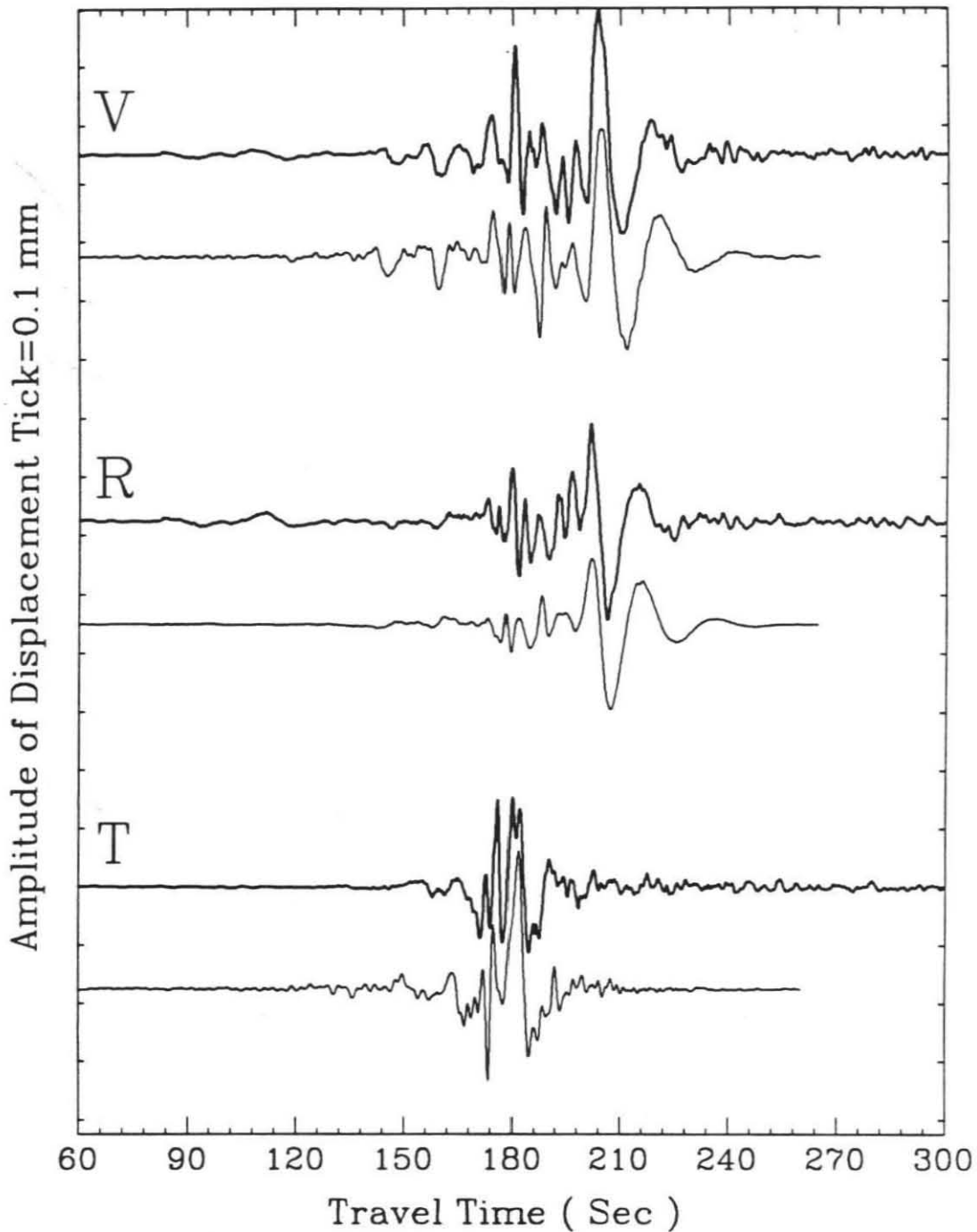
Figure 7: Comparison of the synthetics of the long period model, LPM, and the long period data. Ten modes were used in constructing synthetics for model MPM. The tangential component of the synthetics has been shifted to the left by 4.5 seconds. The upper traces are the observed waveforms. The observations and synthetics are on the same scale.

The source function was assumed known in the previous section but as we move to shorter periods we must be more concerned about source complexity as mentioned in the introduction. We will discuss time history sensitivity later, but in this section we have assumed an asperity type model consisting of three different trapezoids in which the δts are (0.4, 0.05, 0.25), (0.2, 0.15, 0.15), and (0.08, 0.31, 0.23), after Somerville et al. (1989). The broadband synthetics displayed in Figure 8 are appropriate for the long-period model, LPM. The overall fit is promising but lacks the shorter-period signals arriving on top of S_n and sS_n. To model these we return to summing generalized rays. Figure 9 gives the comparison of synthetics of the preferred model short-period model, SPM, (Table 3, Figure 11), to the waveform data. The model was derived by adding some shallow mantle structure.

The shear velocity gradient at the top of the mantle has a strong effect on the S_n and sS_n behavior as displayed in Figure 10. The models used in constructing these synthetics are given in Table 2. The blank boxes in Table 2 indicate that the layers have the same parameters as Model 209. Each model is different from Model 209 in one parameter, namely the shear velocity or thickness. The numbers on the left of Figure 10 are model names. We tried dozens of models with a crustal thickness of 40 km, and concluded that the crust should be thinner to match the gradients and appearances of waveforms of S_{nl}. If we use a faster crust, Model 218, see Table 2, we can see the earlier arrivals of sP_mP group (letter a on the radial component of the synthetics of model 218, Figure 10) and sP_mSP_mP group
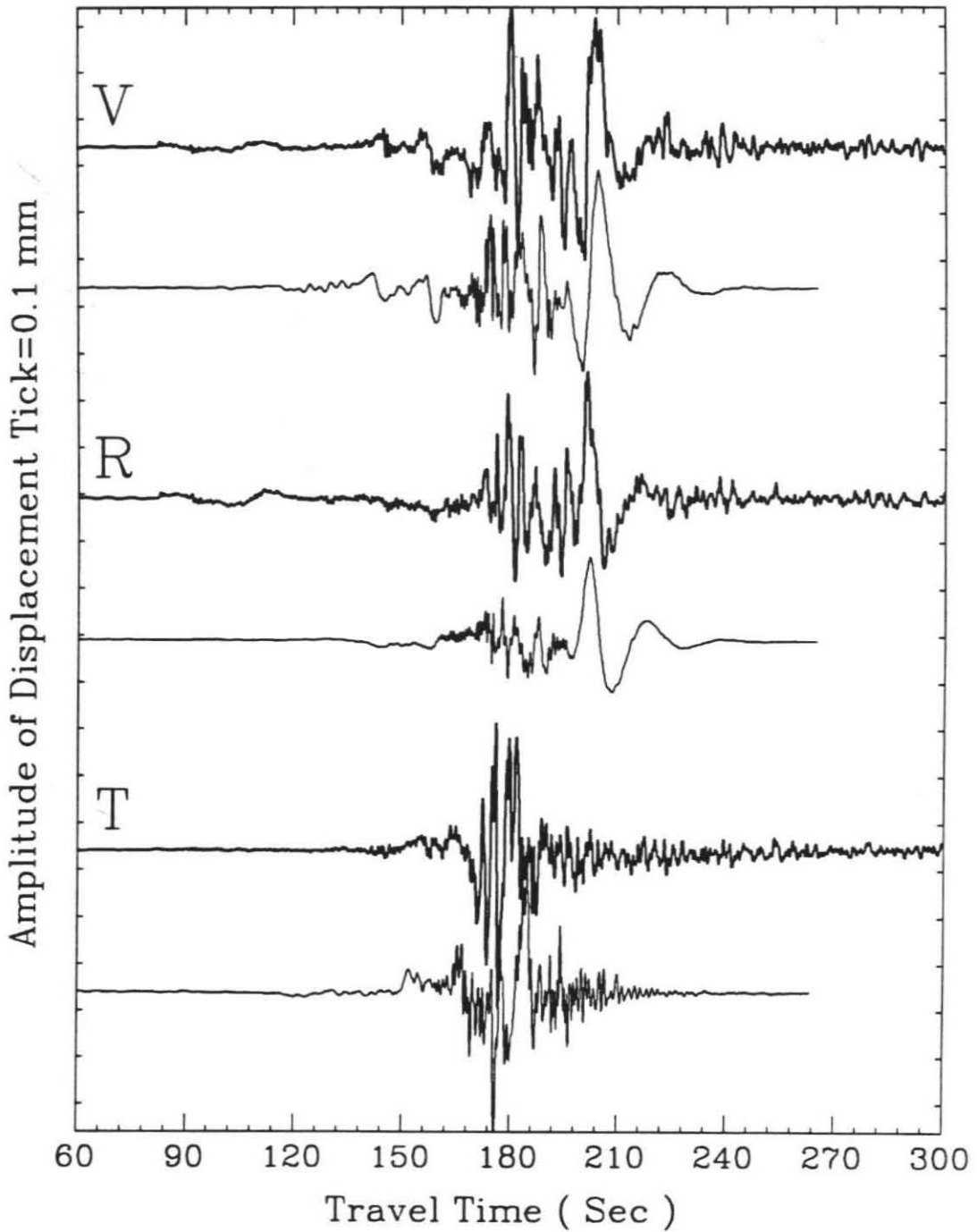
Figure 8: Comparison of the broadband data and the synthetics of the long period model, LPM. Eight modes were used to make these synthetics. The tangential component of the synthetics has been shifted to the left by 1.5 seconds.
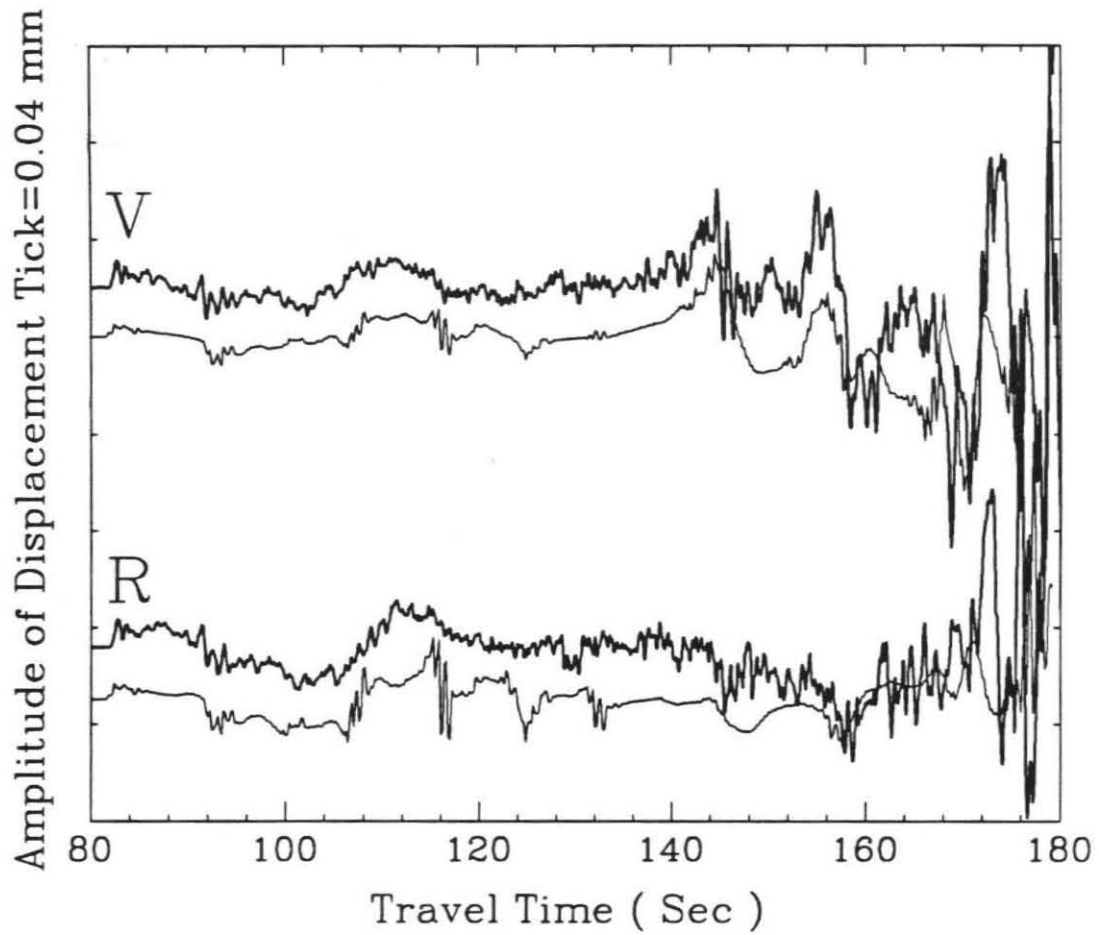
Figure 9: Comparison of the broadband data and the synthetics of the final short period model, SPM. The synthetics were generated with the GRM.

Table 2. Models for sensitivity study of Pnl - Snl, figure 10

MODEL	209	211	212	213	214	215	216	218
α	6.23							6.4
β	3.6							3.7
thickness (km)	35.0							35.0
α	8.06			8.06		8.06		
β	4.6			4.6		4.6		
thickness (km)	10.0			20.0		5.0		
α	8.2	8.2			8.2		8.2	
β	4.7	4.65			4.7		4.7	
thickness (km)	10.0	10.0			20.0		5.0	
α	7.97		7.8					
β	4.55		4.45					
thickness (km)								
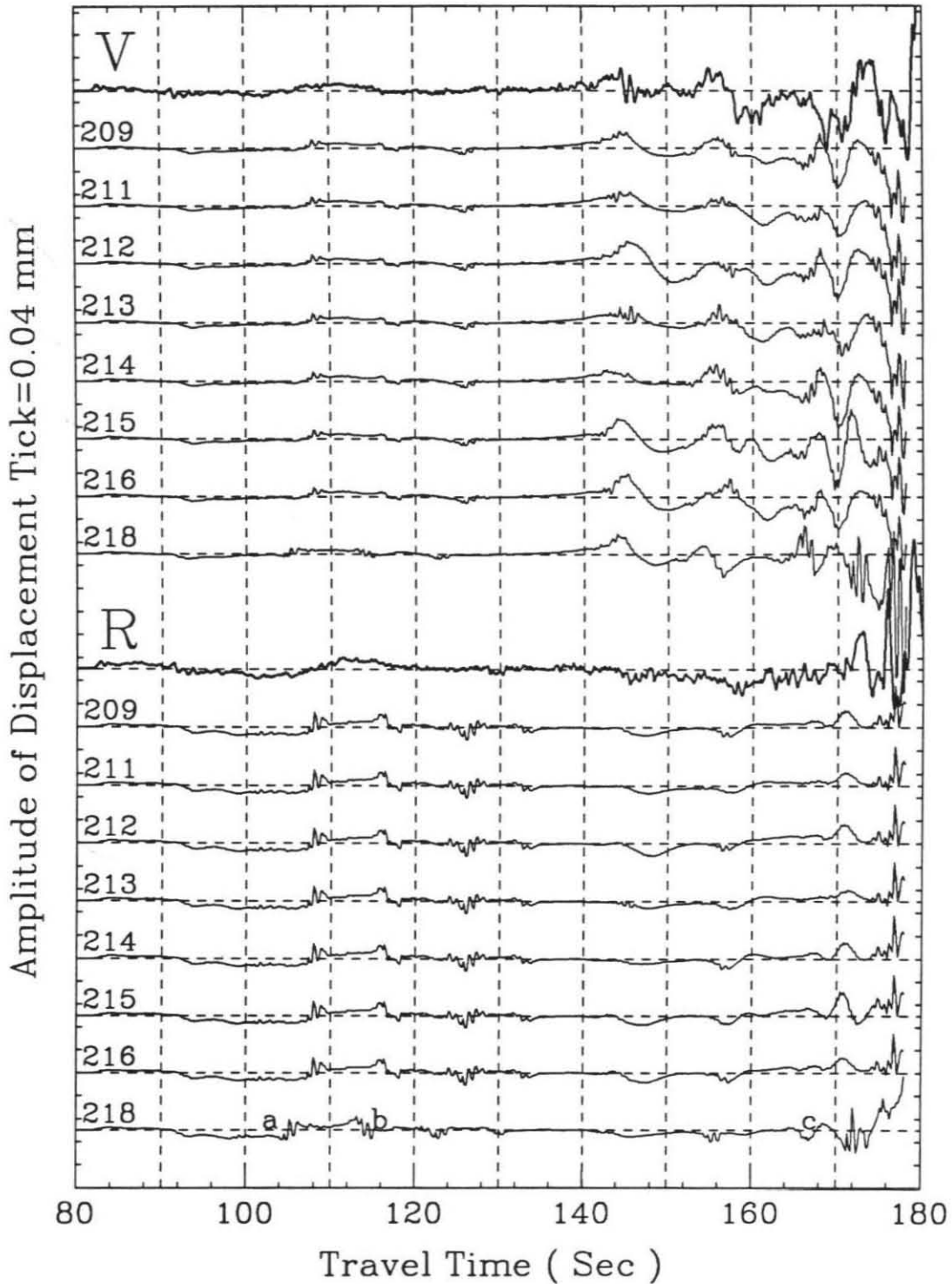
Figure 10: Sensitivity study of the waveforms of S_{nl} and P_{nl} waves to model parameters. The numbers on the left are model numbers indicated in Table 2. The letters *a*, *b* and *c* on the bottom radial component of the synthetics indicate $_sP_mP$, $_sP_mSP_mP$, and $_sS_mSS_mS$ groups of phases respectively.

(letter b), and the $sS_m SS_m S$ group (letter c) phase, and the S_{nl} waveforms predictions are too early. Model 213, and 215 are similar to Model 209 except that the thicknesses of the second layer are 20 km and 5 km respectively. Model 213 predicts smaller amplitudes of S_n and sS_n phases, and discordant waveforms of $sS_m SS_m S$ group phases. Model 215 predicts a nice fit on the radial component of the S_{nl} wave, but the vertical component fit is not so good. The thickness of the second layer can also be estimated from the S_{nl} data. The shear velocity of the third layer can be inferred from comparing the synthetics of models 209, and 211. Comparing the synthetics of models 209 and 212, we can see that Model 209 is better. We also have tried other velocities for this layer, but 4.55 km/sec appears to be the best. Model 209 is the shear velocity model of the SPM, short period model, while the compressional velocities are obtained by modeling the broadband P_n data described below.

A similar sensitivity study of the P_{nl} waveform was applied and used to adjust the P-velocity gradient while holding the shear velocity structure fixed. The best fitting short period model, SPM, found in this fashion is given in Table 3. Note that the lower portion of this model can not be resolved by this data and therefore we have simply adopted a model extended at constant compressional and shear velocities. The appearance of S_n synthetic waveforms of Mode summation Method suggests that this constant velocity layer may not have a shear velocity as high as 4.775 km/sec in a layer of thickness of at least 90 km.

c) Fine-Tuning

In order to fit the surface waves better, we combine the long-period model and the short period model and arrive at the best model, MPM, see Figure 11, and Table 3. At this step, we fix the gradient at the top of the mantle and make some adjustments in the five-layered crustal model discussed earlier. The normal mode method was applied here since the fundamental Rayleigh waveform is sensitive to the crustal velocity gradient.

Figure 12 displays the long-period data along with the synthetics of three models, LPM, MPM, and SPM. The second, third and fourth traces of each group are the synthetics of model MPM, SPM and LPM respectively. Models LPM and MPM predict a reasonable fit to the fundamental Rayleigh waveforms, and models SPM and MPM predict a good fit to the early portion of S_{nl} waveforms.

As a final check, we used the reflectivity method to construct synthetics for the model MPM. The synthetic comparisons are given in Figure 13. The first 100 seconds of the synthetics fit the data well. In this calculation, we used a slowness window of 0.0-0.4 and a frequency band 0.004-4 Hz, assuming an exponential decay factor of 50 (Q_{α}=8600 , and Q_{β}=6200).

SOURCE EFFECTS

Thus far, we have assumed that the earthquake source parameters were well determined by other studies, namely that the strike, dip and rake angles are roughly $323°$, $65°$ and $78°$ respectively. The source depth was estimated by regional P_{nl} and teleseismic depth phases to be near 28 km (So-

Table 3. Model comparison, SPM, LPM, and MPM

LPM			SPM			MPM		
α	β	Th	α	β	Th	α	β	Th
5.97	3.44	8.0				6.04	3.49	8.0
6.18	3.57	8.0				6.24	3.61	8.0
6.36	3.68	8.0	6.30	3.60	35.0	6.30	3.70	8.0
6.52	3.77	8.0				6.52	3.77	8.0
6.57	3.80	8.0				6.58	3.80	3.0
			7.90	4.60	10.0	7.90	4.60	10.0
8.20	4.68	40.0	8.10	4.70	10.0	8.10	4.70	10.0
8.36	4.775	65.0	8.20	4.55	90.0	8.20	4.55	90.0
8.27	4.723	35.0	8.27	4.723	35.0	8.27	4.723	35.0
8.13	4.64	45.0	8.13	4.64	45.0	8.13	4.64	45.0
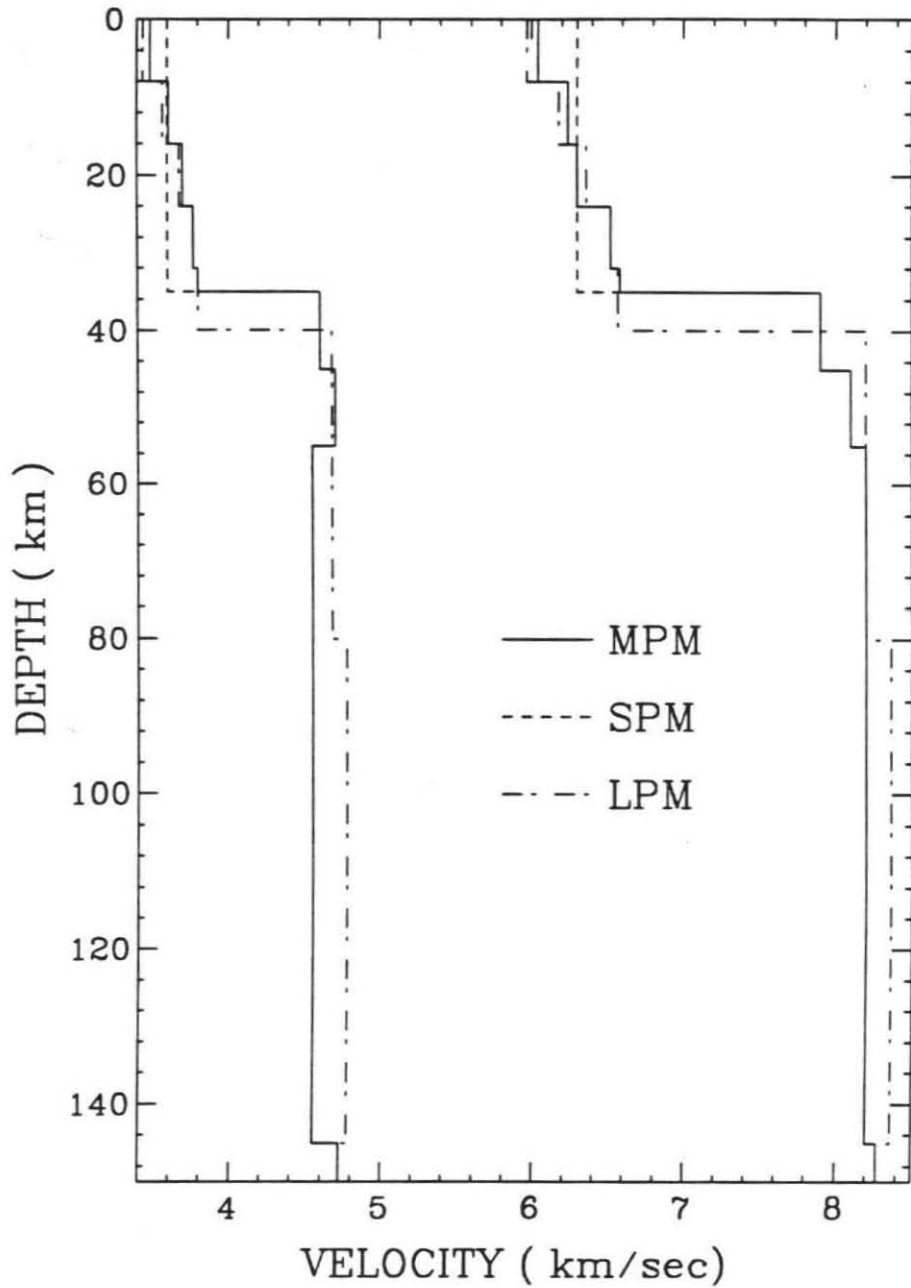
Figure 11: The upper 150 km of the models: long period model, LPM; short period model, SPM and final model, MPM. The bottom portion of SPM is the same as that of MPM.
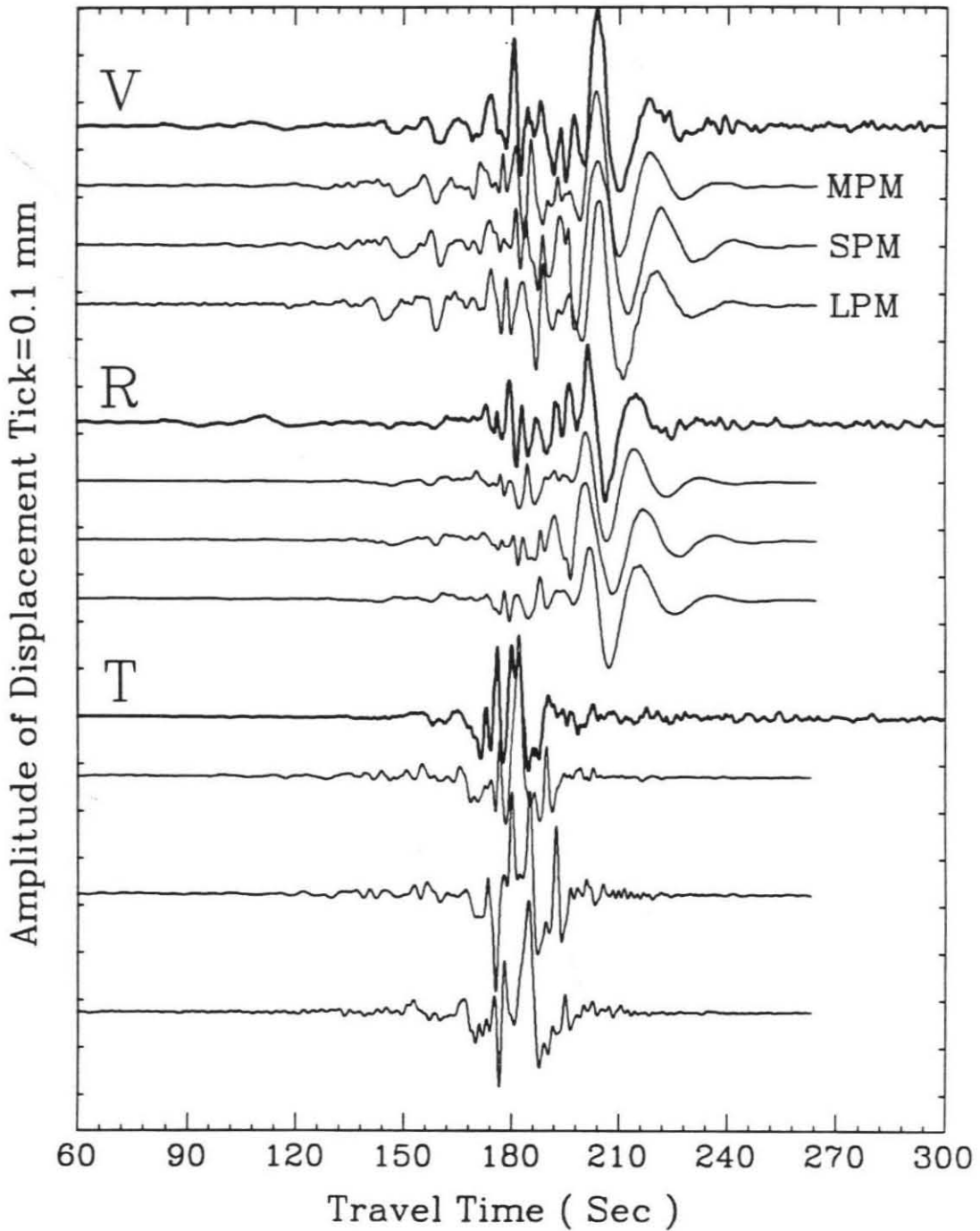
Figure 12: Comparison of the synthetics of the different models with the long period data. The top traces are observed; the second is the synthetics of the final model, MPM; the third is that of the short period model, SPM; and the fourth is that of the long period model, LPM. A 1.5 second time shift to the left was applied to all the tangential components of the synthetics.
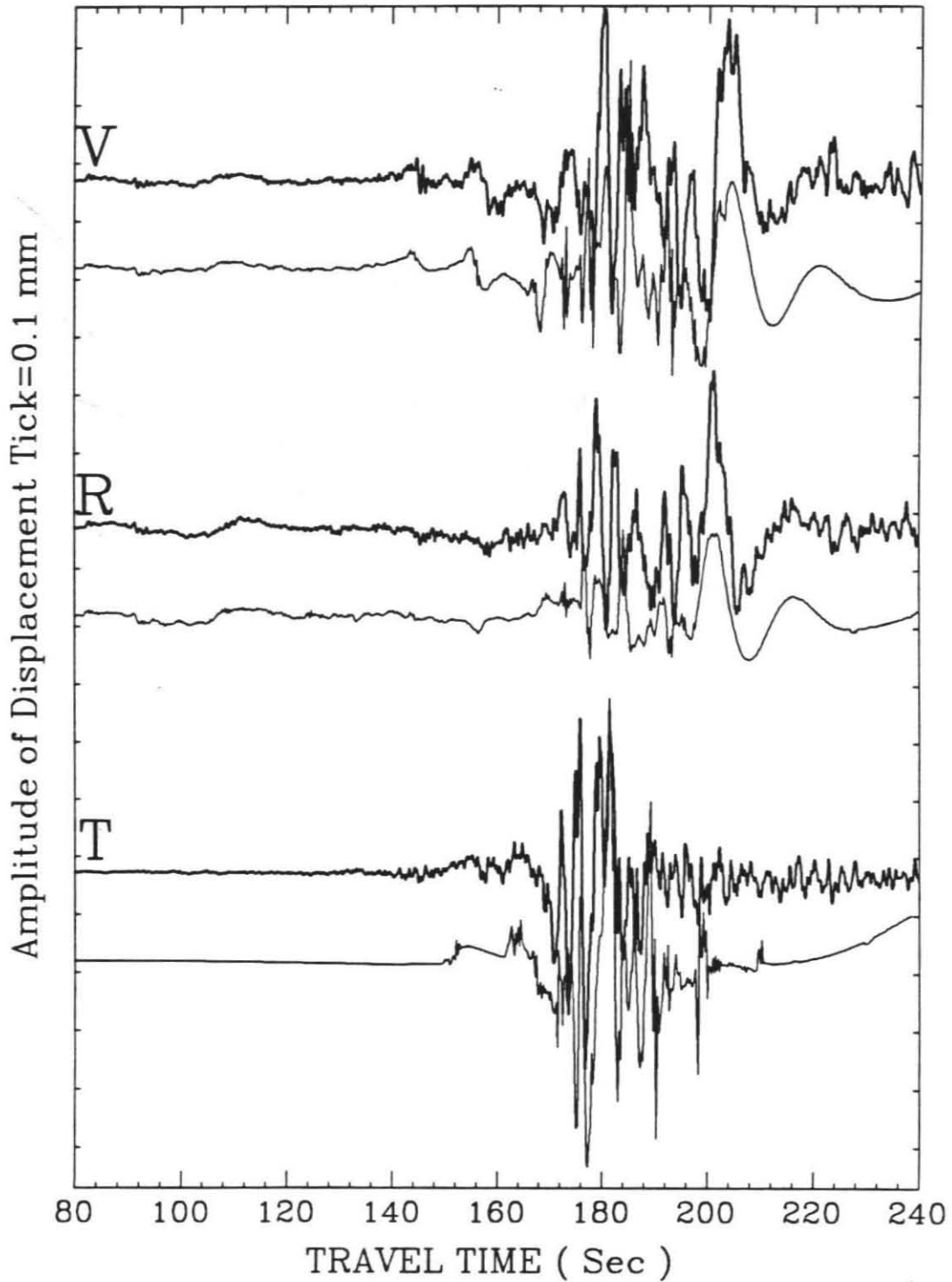
Figure 13: Comparison of the whole broadband data with the synthetics of model MPM. The synthetics were generated using the reflectivity method. The tangential component of the synthetic was shifted 1.5 seconds to the left.

merville et al. 1989; North et al. 1989). The source time history is not so well known nor are the rupture properties. The latter became important for regional phases, especially at short periods.

In this section, we will discuss what can be inferred from these single station regional broadband records if we know the velocity structure of the path. Assuming that our velocity model is correct; we now perturb the above source parameters and test the sensitivity of the broadband waveforms. Because of the amplitude difference between the weak P_{nl} waves relative to the surface waves, we have displayed these sensitivity results in two sections, namely P_{nl} and S_{nl} together and a separate scale for the larger S_{nl} and surface waves.

In Figure 14 we display the sensitivity of the strike, dip and rake angles, while holding the other two parameters fixed at the original values. Varying the strike appears to change the overall amplitude and the ratio without affecting the ratio of P_{nl} to S_{nl}. The ratio of P_n to PL drops somewhat for strikes less than $323°$ and does not match the observation as well. A similar feature occurs when the dip angle falls below $55°$. The original dip looks the best. Varying the rake produces the most interesting results where we see a change in the sS_n waveshape, becoming sharper for pure thrust angles. The radial synthetics for the $\lambda=88°$ looks the best, as determined by overlay, whereas the vertical fits $\lambda=78°$ are slighter better in terms of P_{nl} - S_{nl} amplitude ratio.

Figure 15 displays the long-period WWSSN data along with the synthetics of different source mechanisms. The source mechanisms do not have

Strike   Dip   Rake
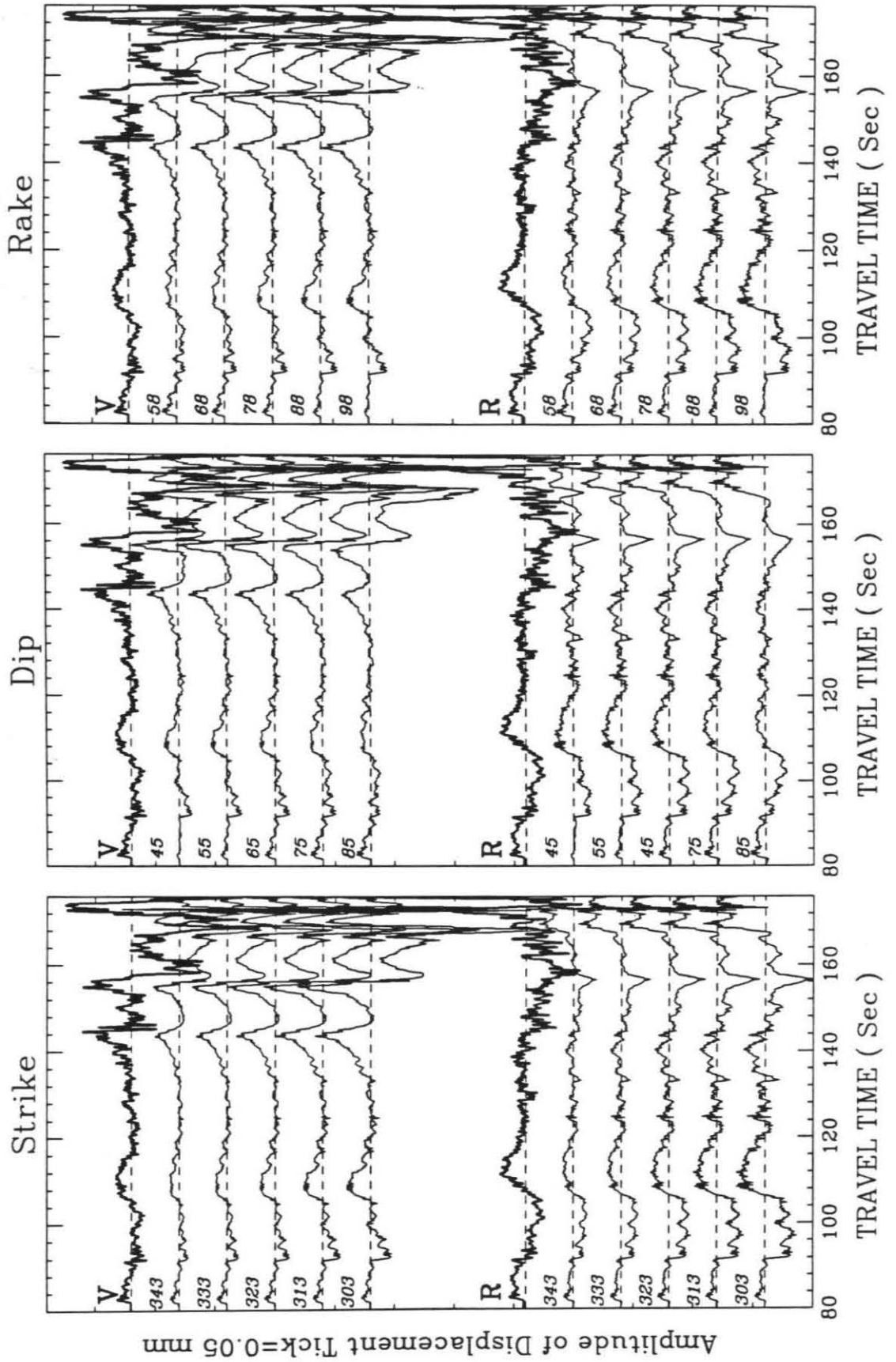
Figure 14: Sensitivity analysis of waveform changes due to variations in strike with $\delta=65°$, $\lambda=78°$ fixed, left column; in dip with $\theta=323°$, $\lambda=78°$ fixed, middle column; and in rake with $\theta=323°$, $\delta=65°$ fixed, right column. The Green's functions used here are the same as those in Figure 3 and 13.
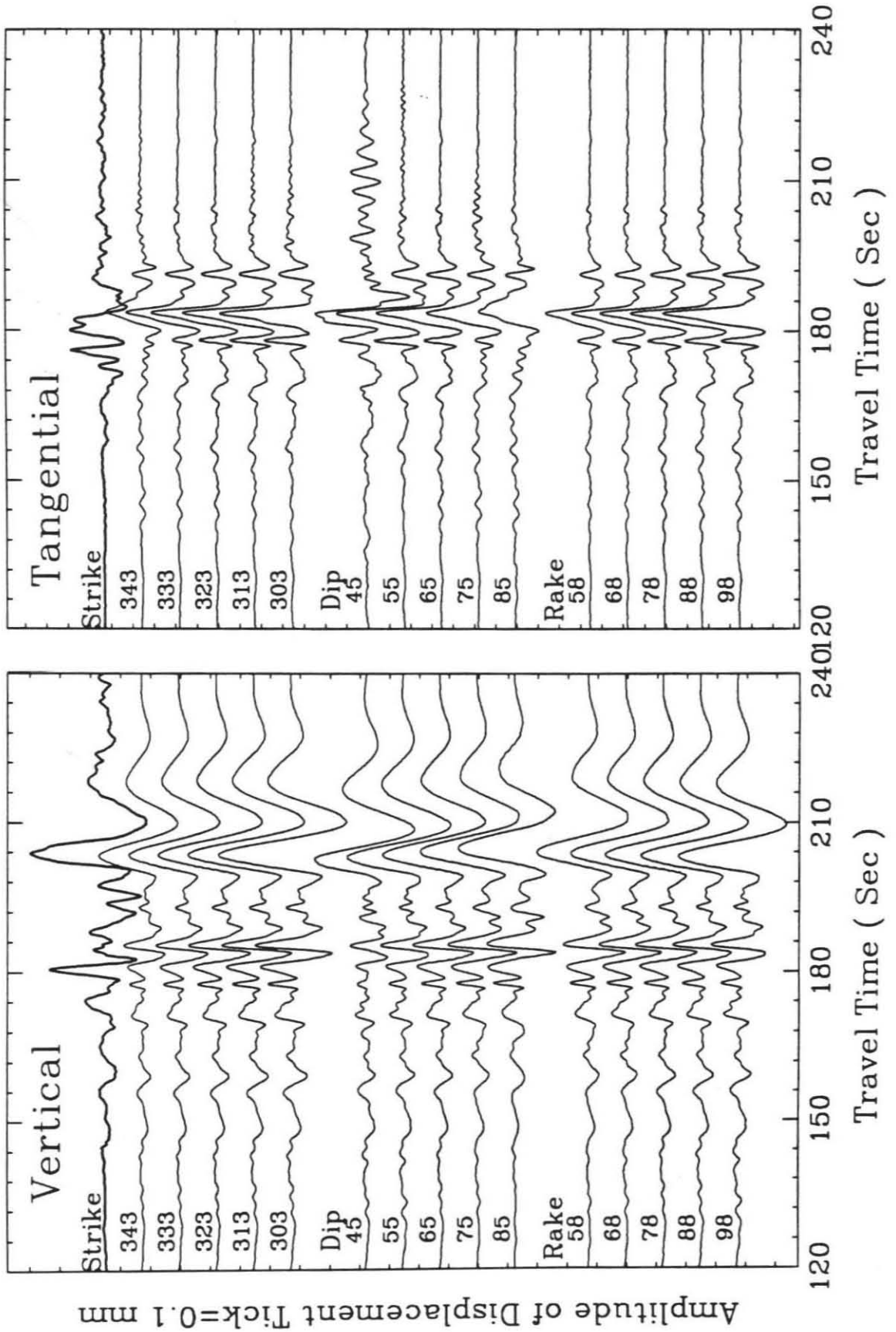
Figure 15: Sensitivity study of surface waveform data and amplitude to variations in strike, dip and rake. The MSM technique was used to generate these synthetics. The vertical components are given on the left and the tangential components on the right holding the other parameters fixed as in Figure 14.

much effect on the surface waveforms, but do affect the amplitudes. A smaller rake or a smaller dip appears to fit the Love waveform data better than the original orientation. Note that S (SH) is near a node and, thus, is susceptible to nonplanar fault effects. Since this event is known to contain at least two strong asperities it is possible that they have slightly different orientations and this could cause the above discordant behavior. One of the reasons for concentrating on the $P-SV$ system is the insensitivity to source descriptions relative to the unknown details needed to study SH as mentioned earlier.

Figure 16 shows the source depth effects on the P_{nl} and S_{nl} waveforms. The absolute travel time of P_n decreases with the depth as expected, as well as the time separation between P_n and sP_n . The S_{nl} wavetrain does not seem to change shape as much as one might have expected. The source depth should be not difficult to determine if the waveforms of the P_{nl} and S_{nl} waves are used for a well calibrated path. The synthetics for a depth of 28 km fit the data the best, which should be of no surprise. Clearly, the depth constraint is the most important of all the assumptions about source properties with respect to modeling. We could have easily adjusted the crustal thickness or velocities to compensate sP_n times, etc.

Source time history sensitivity is displayed in Figure 17 where various possible time histories are given on the right. These time histories originate from different data sets from this event, and are all idealizations of complicated phenomena. The simplest ones were derived from modeling teleseismic short and long-period P-waves as discussed earlier, namely (b) and (c).
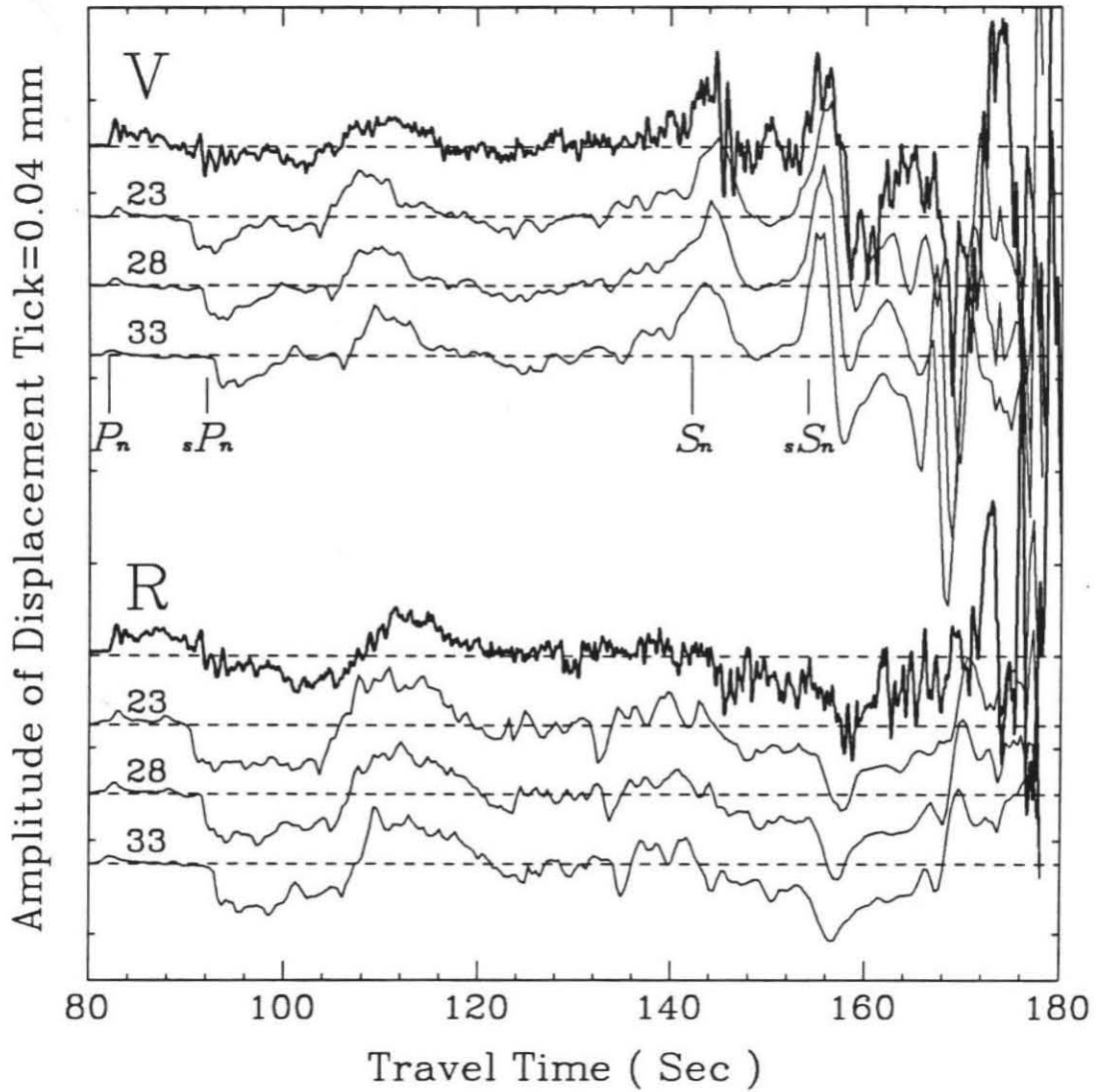
Figure 16: Source depth sensitivity analysis where the upper four traces display the vertical components, and the lower traces display the radial components. The first trace of each set is the broadband data followed by synthetics for various depths.
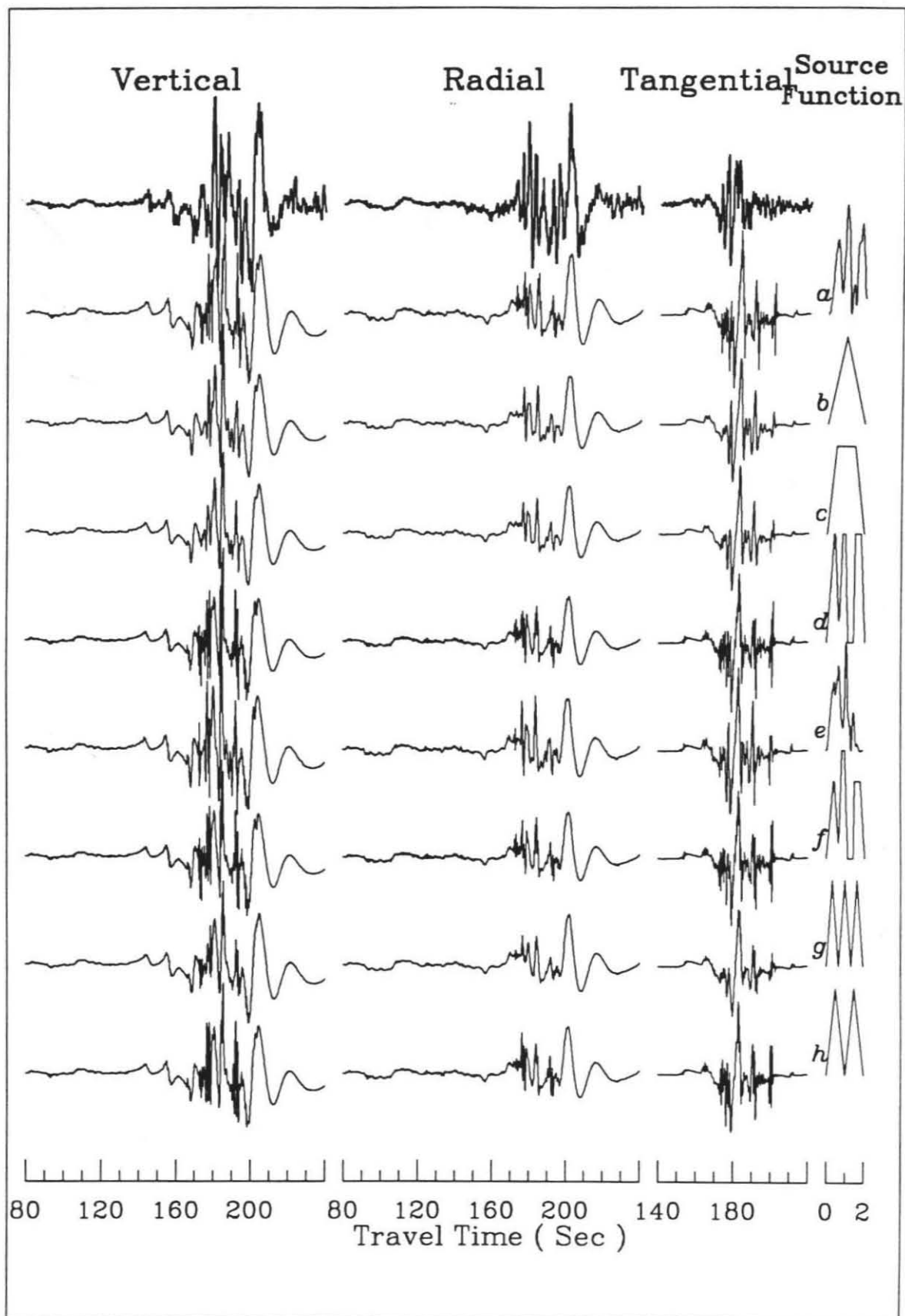
Figure 17: Sensitivity analysis of the waveform effects due to variations in source history. The left column are the vertical components of the data and synthetics. The middle two are radial and tangential components. The column on the right indicates the various source histories used with the corresponding synthetics on the left. These are reflectivity synthetics.

Case (b) was used in the long-period modeling where one usually uses a relatively coarse time sampling and thus a simple triangle is sufficient. The more detailed information about source complexity comes from the strong motion data. Far-field approximations of the time histories depend on direction with two possible sources (a) and (e) proposed by Somerville and Helmberger (1990) with case (e) preferred. Case (d) was used in the broadband modeling discussed earlier which is an analytical approximation to case (a) (Somerville et al. 1989) . Case (f), (g) and (h) are still more approximations. An overlay comparison of source function (e) with the data appears to be the best although there is not very much difference between the synthetics.

The point of this section was not necessarily to help constrain this particular earthquake but to display the source resolving power once these Green's functions are established. This model and associated Green's functions can be used to study other events roughly along this path such as older historic events recorded at Weston, etc.

DISCUSSIONS AND CONCLUSIONS

Our velocity structure along the path from Quebec to Harvard is distinctly slower than proposed in other studies. For example, the shear velocity of the lid of the model, 4.6-4.7 km/sec , is slower than that of either the ATL model, 4.75 km/sec (Grand and Helmberger, 1984a), or the SNA model, 4.8 km/sec (Grand and Helmberger, 1984b). In a tomographic inversion study for shear velocity beneath the North American Plate, Grand

(1987) concluded that the upper 140 km of the crust and mantle of this region was very fast although he did find a major velocity boundary along this path at greater depths. It seems that the data we used do not agree with this fast structure. Perhaps S wave splitting is occurring with the *SH* velocity exceeding the *SV* velocity by about 3%. This would be compatible with the results of Gee and Jordan (1989) for the Siberian plateau. Another explanation may arise from epicentral distance uncertainty, since the velocities are sensitive to the distance and origin time. For example, if the epicentral distance were 640 km instead of 625 km, the model would be 2 percent slower than the SNA model (Figure 18 and Table 4). Note that waveform fits are comparable to those found earlier. Errors in distances up to 15 km or more are possible, if the location is determined by teleseismic means. For instance, the distance between the location given by USGS and that given by HRV is 12 km for this event. However, in this particular case, the location, based on close-in aftershock data recorded by the Geological Survey of Canada (North et al., 1989) is probably accurate to 5 km. Finally, perhaps this path to Harvard, which runs along an old suture zone, is indeed slow and this slowness is caused by a regional anomaly (Sykes, 1978).

The Q_β estimates of eastern North America are of order 300 for the crust, and less than 200 for the mantle (Hwang and Mitchell, 1987). Synthetics generated with these values do not match the data as well as those generated with Q_β=6200, Q_α=8600 do, which we assumed to simulate the infinite Q case. However, these Q values were derived for periods greater than 50 seconds and are probably, not appropriate to these broadband

Table 4. Model comparison

625 km			640 km		
α	β	Th	α	β	Th
6.04	3.49	8.0	6.26	3.56	8.0
6.24	3.61	8.0	6.45	3.67	8.0
6.30	3.70	8.0	6.59	3.75	8.0
6.52	3.77	8.0	6.71	3.82	8.0
6.58	3.80	3.0	6.71	3.82	3.0
7.90	4.60	10.0	8.10	4.70	10.0
8.10	4.70	10.0	8.35	4.80	10.0
8.20	4.55	90.0	8.40	4.65	90.0
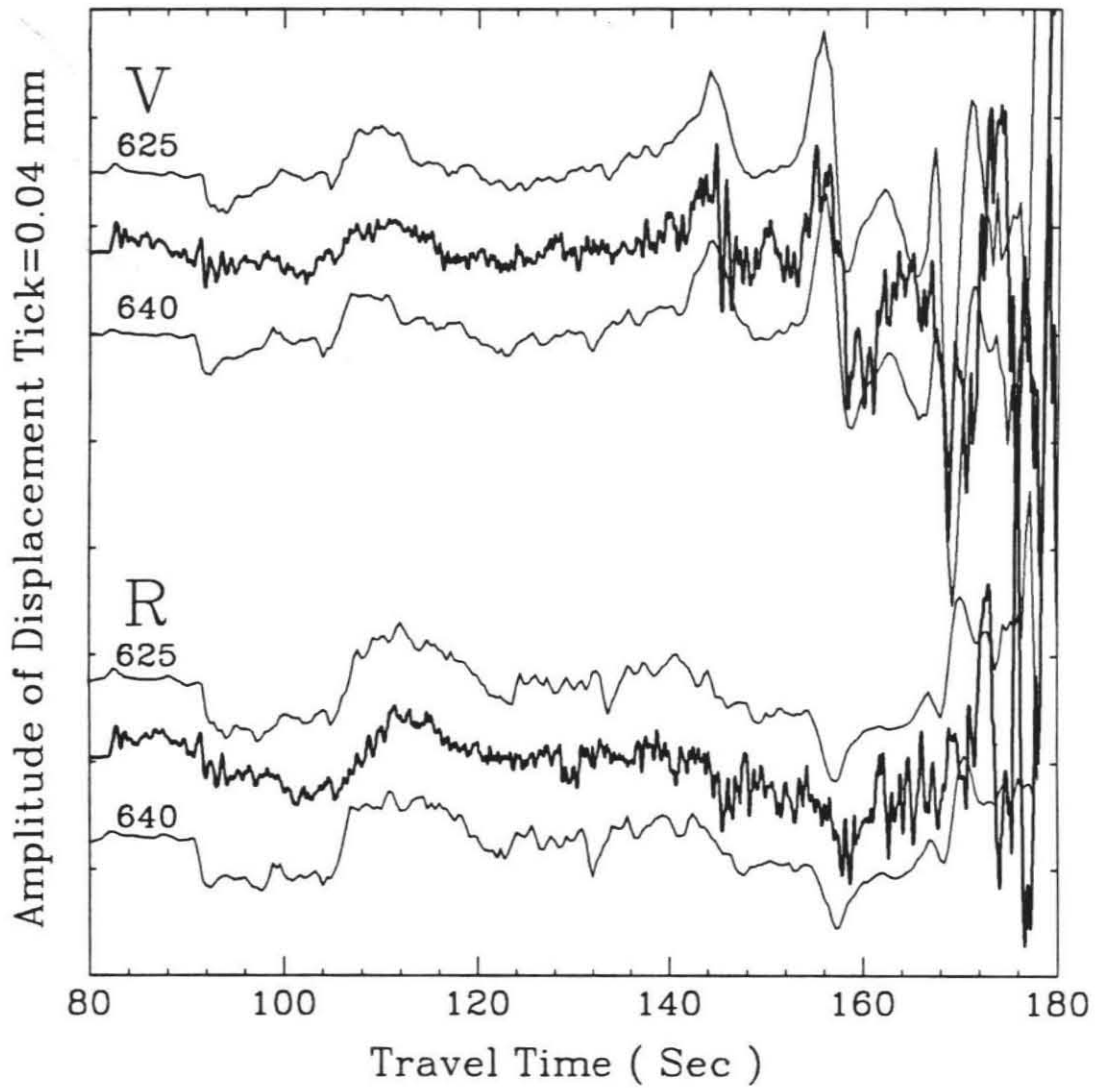
Figure 18: Comparison of the synthetics generated from model MPM, and the model for 640 km (Table 4) with the broadband data displayed as the middle trace of each set.

records. In any case, the observations have more high frequencies than the synthetics at large Q's and lowering Q does not look promising, at least for this particular path.

In summary, we presented a strategy for modeling broadband records at regional distances. The basic procedure consists of breaking the seismograms into segments where the waveforms of each segment prove sensitive to a particular portion of the waveguide. Three divisions appear to be the most useful, namely, a) the P_{nl} segment containing P_n , pP_s , sP_s, P_mP, its multiples and P -coupled PL; b) the S_{nl} segment containing S_n , sS_s , S_mS, its multiples and S-coupled PL, c) the fundamental Rayleigh wave segment.

(a) P_{nl} wavetrain

The long-period component of the P_{nl} wavetrain is controlled by the crustal thickness, the average crustal velocities, and the compressional velocity of the mantle. Its shorter period contributions are influenced by the sharpness of the Moho transition, the fine structure at the top of the mantle, compressional velocity gradients, etc.

(b) S_{nl} wavetrain

This segment is probably the most difficult to appreciate. It has been studied less, and produces the strongest short-period arrivals, usually called the L_g phase. The beginning portion of this wavetrain consists of S_n , and sS_s, as identified in this study, and can be used to study the shear velocity properties of the top of the mantle. Further into this wavetrain, one finds stronger arrivals associated with multiple-bounce S_mS and probably S-coupled PL from the uppermost surface layer. These phases are included in

the synthetics of both methods, the normal mode method and reflectivity, but have not been subdivided into individual ray groups for special study. The longer period S-coupled PL waves trapped in the crustal layer over a mantle waveguide have been studied extensively, and are responsible for contaminating teleseismic SV body waves to the extent that they are rarely used in source studies. The laterally varying surface waveguide consisting of the upper few kilometers of the Earth is likely to produce similar types of semi-trapped shorter period P waves. Such waves are easily identified in local records (Dreger and Helmberger, 1990), but have not been investigated at these ranges.

(c) Fundamental Rayleigh wavetrain

The fundamental Rayleigh waves are controlled by the shear velocity structure of the crust at these ranges and are not particularly sensitive to the mantle parameters. This statement is generally true for the fundamental Loves waves as well (Zhao et al., 1989). Normal surface wave modes are easily generated for possible models and fitting this portion of the record proved relatively easy.

In conclusion, this study demonstrates that broadband regional phases can be modeled. This study, thus, has several implications with respect to source discrimination and with respect to exploration of the lithosphere. Earlier studies have established the ease of modeling the beginning portion of a long period record in terms of P_n, pP_n, and sP_n; i.e., a layer over halfspace. Apparently, the S_n, pS_n, and sS_n window is also easily modeled on the vertical component. The phases can be seen at low magni-

tudes where teleseismic signals are no longer recorded above the noise. For example, the Saguenay earthquake produced only a few high quality teleseismic waveforms. Thus, S_{nl} and P_{nl} on standard long period WWSSN records can probably be used to study events down to magnitude 4.5 since P_{nl}'s have proved useful down to magnitude 5 and S_{nl}'s are considerably stronger. In addition, the strongest short period signals are related in timing with the long period arrivals. One can use the latter as a guide in constructing broadband models (many layers) and scattering models for still shorter periods.

Presently, it has proven quite difficult to discriminate small explosions from small earthquakes as well as the $m_b:M_s$ ratio does at larger magnitudes (see Taylor et al., 1989). One excellent method of establishing the identification of an event is by depth and, therefore, by depth phases. Calibrating crustal models and the development of regional Green's functions addresses this problem.

Exploration of the continental lithosphere in interesting regions has proven difficult. Molnar (1989) and his colleagues have spent a great deal of effort studying the collision zone between the Indian and Asian plates. The absolute velocities of P and S at the top of the mantle is one of the key factors in establishing temperatures there. Furthermore, velocity gradients can probably establish whether heating is taking place from the top-down or vice versa (Zhao et al. 1989). Thus, broadband modeling of regional data from southern platforms of the Soviet Union and transition zones of western China can provide some key information and will be presented in future re-

ports.

ACKNOWLEDGMENTS

REFERENCES

Aki, K. and P. G. Richards, 1980. *Quantitative Seismology, Theory and Methods*, W. H. Freeman and Company, San Francisco.

Apsel, R. J. and J. E. Luco, 1983. On the green's functions for a layered halfspace, *Bull. Seism. Soc. Am*, **73**, 931-952.

Dreger, D. and D. V. Helmberger, 1990. Broad-band modeling of local earthquakes, submitted to *Bull. Seism. Soc. Am.* .

Gee, L. S. and T. H. Jordan, 1989. Polarization anisotropy and fine-scale structure of the Eurasian upper mantle, *Geophys. Res. Lett.*, **8**, 824-827.

Grand, S. P., 1987. Tomographic inversion for shear velocity beneath the North American plate, *J. Geophys. Res.*, **92**, 14065-14090.

Grand, S. P., and D. V. Helmberger, 1984a. Upper mantle shear structure beneath the northwest Atlantic Ocean, *J. Geophys. Res.*, **89**, 11465-11475.

Grand, S. P., and D. V. Helmberger, 1984b. Upper mantle shear structure of North America, *Geophys. J. R. astr. Soc.*, **76**, 399-438.

Harkrider, D. G., 1964. Surface waves in multilayered elastic media, I. Rayleigh and Love waves from buried sources in a multilayered elastic halfspace, *Bull. Seism. Soc. Am.*, **54**, 627-679.

Harvey, D., 1981. Seismogram synthesis using normal mode superposition: The locked mode approximation, *Geophys. J. R. astr. Soc.*, **66**, 37-61.

Helmberger, D. V., 1983. Theory and application of synthetic seismograms, in *Proceedings of the International School of Physics << Enrico Fermi >>, Course LXXXV, Earthquakes: Observation, Theory and Interpreta-*

tion, edited by Kanamori, H. and E. Boshi, North-Holland Publishing Company.

Helmberger, D. V. and G. R. Engen, 1980. Modeling the long - period body waves from shallow earthquakes at regional distances, *Bull. Seism. Soc. Am.* , **70**, 1699-1714.

Helmberger, D. V. and D. G. Harkrider, 1978. Modeling earthquakes with generalized ray theory, in *Proceedings of IUTAM Symposium: Modern Problems in Elastic Wave Propagation*, edited by J. Miklowitz, and J. Achenback, New York, N. Y.

Hwang, H.-J. and B. J. Mitchell, 1987. Shear velocities, Q_β, and the frequency dependent of Q_β in stable and tectonically active regions from surface wave observations, *Geophys. J. R. astr. Soc.*, **90**, 575-613.

Mallick, S. and L. N. Frazer, 1988. Rapid computation of multioffset vertical seismic profile synthetic seismograms for layered media, *Geophysics*, **55**, 479-491.

Molnar, P., 1989. The geologic evolution of the Tibetan Plateau, *American Scientist*, **77**, 350-360.

North, R. G., R. J. Wetmiller, J. Adams, F. M. Anglin, H. S. Hasegawa, M. Lamontagne, R. Du Berger, L. Seeber and J. Armbruster, 1989. Preliminary results from the November 25, 1988 Saguenay (Quebec) earthquake, *Seism. Res. Let.* , **60**, 89-93.

Somerville, P. G., and D. V. Helmberger, 1990. The effect of crustal structure on the attenuation of strong ground motion in eastern north America. Submitted to Fourth U. S. National Conference of Earthquake En-

gineering at Palm Springs, May 1990.

Somerville, P. G., J. P. McLaren, C. K. Saikia and D. V. Helmberger, 1989. The November 25, 1988 Saguenay, Quebec earthquake, submitted to *Bull. Seism. Soc. Am.* .

Sykes, L. R., 1978. Intraplate seismicity, reactivation of preexisting zones of weakness, alkaline magmatism, and other tectonism postdating continental fragmentation, *Rev. Geophys. Space Phys.*, **16**, 621-688.

Taylor, S. R., M. K. Denny, E. S. Vergino, and R. E. Glaser, 1989. Regional discrimination between NTS explosions and western U. S. earthquakes, *Bull. Seism. Soc. Am.*, **79**, 1142-1172.

Wallace, T. C. and D. V. Helmberger, 1982. Determining source parameters of moderate-size earthquakes from regional waveforms, *Phys. Earth Planet. Inter.*, **30**, 185-196.

Zhao L. - S., D. V. Helmberger, and D. G. Harkrider, 1989, Shear-velocity structure of the crust and upper mantle beneath Tibetan and Southeastern China, submitted to *Geophys. J. R. astr. Soc.* .

CHAPTER 3

Shear-Velocity Structure of the Crust and Upper Mantle
Beneath Tibetan Plateau and Southeastern China

ABSTRACT

This chapter addresses the velocity structure of the crust and upper
mantle beneath Southern China with special emphasis on the Tibet region.
Waveform data from 48 earthquakes as recorded on the WWSSN and GDSN
are used in this detailed forward modeling study. Constraints on the upper
crustal section are derived from modeling local Love waves in the time
domain applying the mode-sum modeling technique. Lower crustal con-
straints are derived by modeling the P_{nl} wavetrain with the reflectivity
method. An average crustal thickness of 70 km is obtained beneath the Ti-
betan Plateau with a modest increase of velocity with depth. The lithospher-
ic and upper-mantle structure is deduced from modeling S and SS triplica-
tion waveform data and relative travel times by applying a combination of
WKBJ and generalized ray methods. $S-SS$ seismograms chosen with
bounce-points directly under Tibet allow remote sensing of this inaccessible
region. The resulting model is an averaged one-dimensional model where
corrections for lateral variation have been applied. We conclude that the

upper-mantle structure in the entire region is basically shield-like below 200 km (SNA). However, the velocity of the lithosphere is abnormally slow, roughly 5% beneath Tibet. The model derived for Tibet does not have a distinct lid, and has a positive velocity gradient in the crust, suggesting crustal shortening. A preliminary velocity model for Southeastern China is also suggested.

INTRODUCTION

China is a part of the Eurasian plate, but the margins of the Indian and Philippine plates are involved in the Himalayas and in the coastal ranges of Taiwan, respectively. Relative to the north of China, the Indian plate is moving NNE, and the Philippine plate is moving NW (Minster et al. 1974). The arrows in Figure 1 show the directions of the motions of the plates surrounding China (Wang and Xu, 1985). China is composed mainly of four major tectonic provinces, the Tarim Basin, Sino-Korea Craton, Yangtze Craton and the Tibetan Plateau. The Tarim basin, Sino-Korea craton, and northern part of Yangtze craton are precambrian massives (Yang et al. 1986; Zhang et al. 1984). The provinces are characterized by large variations in crustal thickness as indicated in the isopach map presented in Figure 2 . The thickness of the crust of the eastern part of China is about 35 km, that of northern China is 45 km, and that of the Tibetan Plateau is more than 50 km. Thus, we would expect the crustal and upper mantle velocity distributions beneath these four tectonic provinces to be much different.

The dynamic processes that lead to the formation and maintenance of
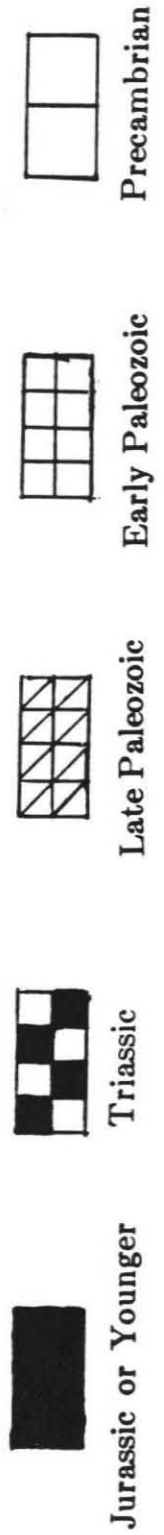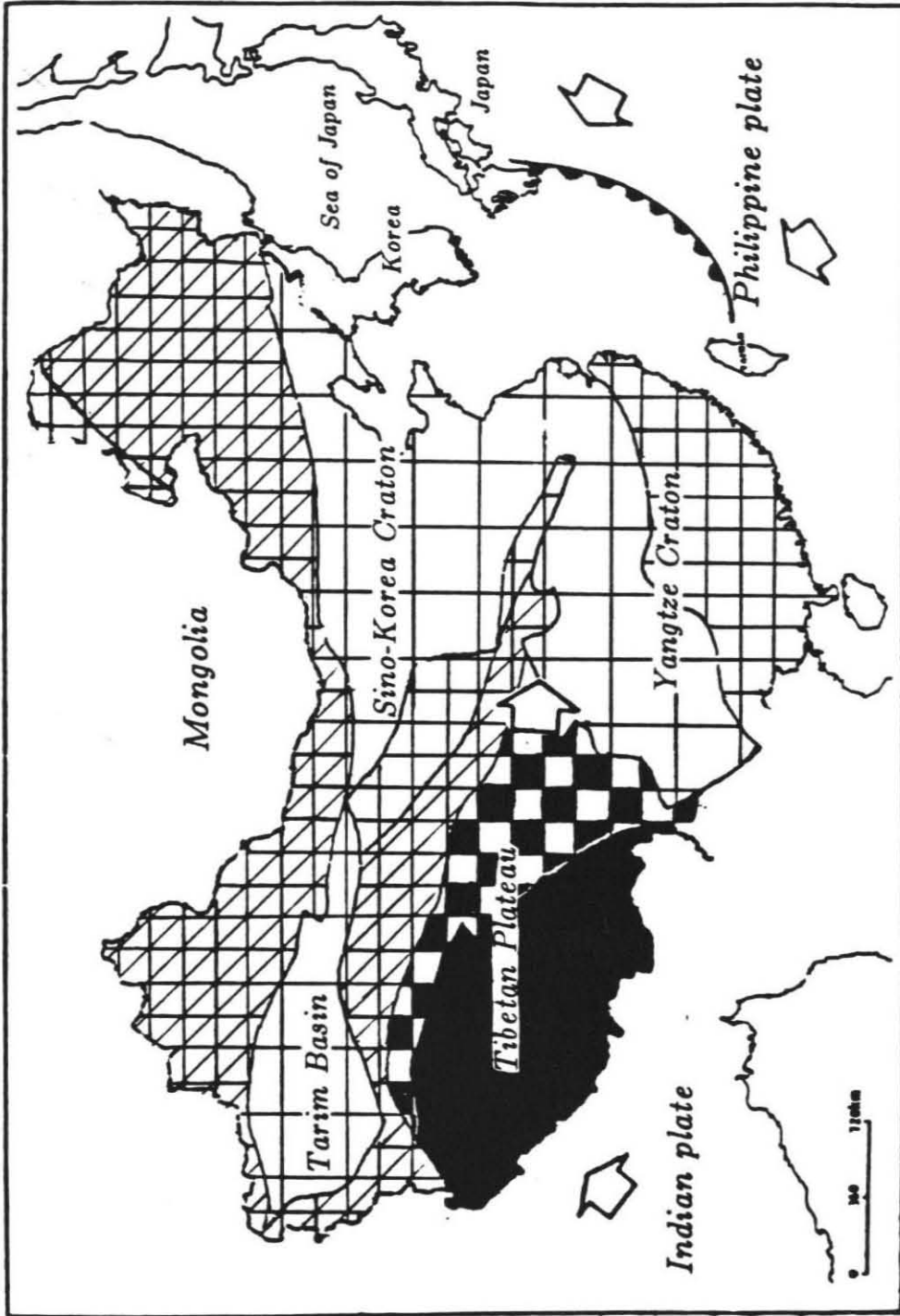
Figure 1. Sketch map of plate tectonics of China, and the directions of the motions of the plates surrounding China. China occupies the Eurasian plate, part of the Indian plate, and a small part of the Philippine Sea plate (Zhang et al. 1984).

ISOPACH MAP OF EARTH CRUST OF CHINA
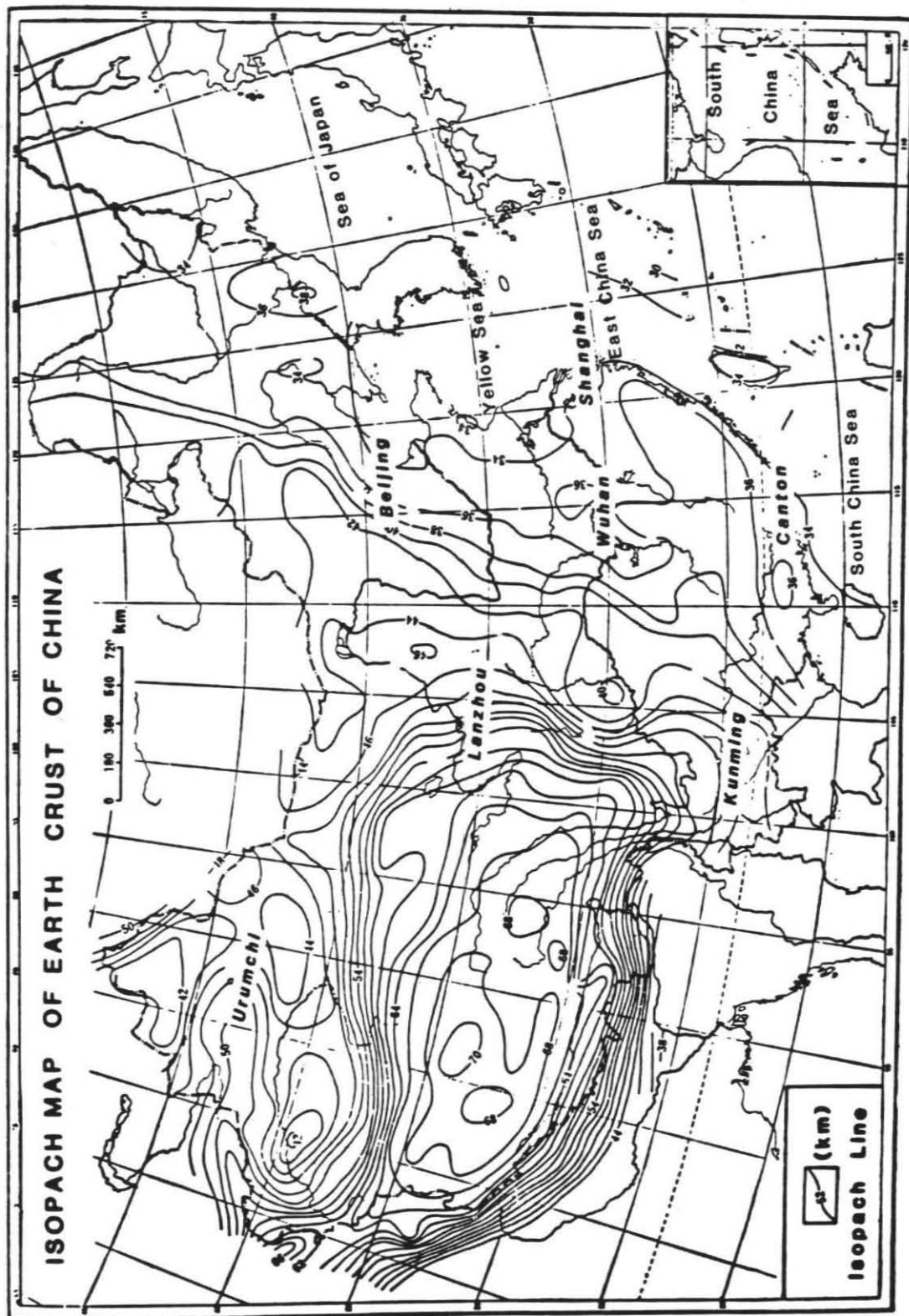
Figure 2. Isopach map showing crustal thickness (in kilometers, Zhang et al. 1984) in China. In eastern China, a distinct north-northeast-trending belt that contains a marked difference in crustal thickness is parallel to a subduction zone to the east of the Asian continent. The crustal thickness in western China, the Tibetan Plateau is more than 50 km.

a mean elevation of 5 km over the Tibetan Plateau are not well understood and are controversial. Because of its obvious importance for constraining these deep processes, the seismic velocity structure of the Tibetan Plateau has been the subject of many studies.

The three-year Sino-Franco joint research program (1980-1982) contributed significantly to both the geology and geophysics of the Tibetan Plateau. P-wave velocity profile of a 600 km line (from $(28.5°N,89.0°E)$ to $(32.2°N,91.7°E)$) was obtained from seismic soundings. The thickness of the crust changes from about 40 km to 75 km along this profile. The results of the program are published in a series of papers (see for example Hirn et al. 1984; Teng, 1987).

Some studies of the seismic velocity structure of the Tibetan Plateau used group and phase velocities of fundamental mode surface waves (e. g. Chen and Molnar, 1981; Romanowicz, 1982; 1984; Brandon and Romanowicz, 1986; Feng, 1982). Other studies used P_n and S_n waves (Barazangi and Ni, 1982; Ni and Barazangi, 1983, Holt and Wallace, 1989) to derive the velocity of the lid beneath the crust of the plateau. Recently, Lyon-Caen (1986) used the travel times and waveforms of long period SH wave data recorded at distances of 10-30 degrees and some $SS-S$ waveforms to constrain the upper mantle velocities down to a depth of 400 km beneath the plateau. She argues that the Indian plate is not underthrusting the whole of the Tibetan Plateau at the present time.

For the other parts of China, there are fewer studies reported in English. For the Yangtze Craton, there are surface wave studies (Wier, 1982;

Feng, 1982). Shedlock and Roecker (1987) used travel time inversion to study the elastic wave velocity structure of the crust and upper mantle beneath the Sino-Korea craton.

Wang and Yao (1989) gave one upper mantle shear velocity model for the Tibetan Plateau, and one upper mantle shear velocity model for North China (Tarim basin and Sino-Korea craton) by modeling the long-period $SS-S$ waveforms recorded at distances of 30-60 degrees.

The purpose of this study is to constrain the upper mantle shear velocity structure of southern China by using the travel times and waveforms of Love waves recorded at distances of 7-23 degrees; long-period S waves recorded at distances of 15-30 degrees; and long-period $SS-S$ waves recorded at distances of 30-60 degrees. Recent work using long-period body wave data have demonstrated that the travel times and waveforms of SH waves recorded at distances up to 30 degrees and of $SS-S$ waves recorded between 30 and 60 degrees can provide some constraints on the large-scale velocity structure of the upper 670 km of the mantle and particularly of the upper 400 km (Grand and Helmberger, 1984a; 1984b; Rial et al. 1984). In this distance range the waveforms are controlled by the interference of phases whose turning points are in the regions above the 400 km discontinuity, between the 400 km and 670 km discontinuities, and below the 670 km discontinuity. The differential travel times of SS waves and S waves are controlled mainly by the velocity structure of the neighborhood of the bounce points of the SS phases. This property makes it possible to constrain the shear velocity structure of an area not big enough for the pure path data. The search of models

can be achieved by comparing the synthetics with the data. The *WKBJ* method (Chapman, 1978), which is discussed at length by Grand and Helmberger (1984a), was used for constructing synthetic *S* and *SS* waves, and the mode summation method (Harkrider, 1964; 1970) was used in studying Love waves.

DATA AND METHODS

In this study, we used travel times and waveforms of long-period *SH* wave data from 48 earthquakes, magnitude 4.5 or larger, from 1965 to 1985, within or around China (Table 1), as recorded at the *WWSSN* stations around China (ANP, BAG, HKC, KBL, LAH, MAT, MSH, NDI, NIL, QUE, SEO, SHL, SHK), *SRO* stations (KAAO, TATO), and some Chinese stations (GYA, GZH, LZH, XAN). In Table 1, the source information is from Bulletin of the International Seismological Centre (ISC), otherwise indicated. The seismograms have high signal to noise ratios, and are not necessarily from earthquakes with known source mechanisms. There are only a limited number of Tibetan earthquakes carefully studied (e.g. Ni and Barazangi, 1984; Molnar and Chen, 1983; Tapponnier and Molnar, 1977; Baranowski et al. 1984). Because of lack of local station net, it is almost impossible to know the source mechanisms of the smaller Tibetan earthquakes, which generated on-scale surface waves. However, we can infer roughly the source mechanism from the *S*-waveforms (Langston and Helmberger, 1975). This rough source mechanism is sufficient for *S*-, *SS*-wave study as demonstrated by Grand and Helmberger (1985). The source depth effects on *S*- and *SS*-

Table 1. Earthquakes and stations used in this study.

	Date	Origin Time	Location (°N °E)	Depth (km)	Mag Mb Ms	Study area	Station	Δ	Phase
1	06 14 65	13:17:02.4	32.09 87.72	36	5.2	TP	SHL	7.5	Love
							LAH	11.4	Love
2	06 16 65	23:49:08.2	32.04 87.46	69	4.8	TP	NDI	9.5	Love
3	06 17 65	20:14:50.1	32.12 87.76	15	5.1	TP	LAH	11.4	Love
4	06 18 65	01:18:39.0	32.01 87.59	43	5.1	TP	NDI	9.6	Love
5	02 05 66	15:12:32.9	26.22 103.21	32	5.6	EC	SEO	23.1	S
6	02 07 66	23:06:37.4	30.25 69.89	28	5.6	TP	ANP	45.7	SS
7	03 14 66	04:42:50.7	32.47 97.46	33	4.8	TP	SHL	8.4	Love
							NDI	17.8	Love
8	03 17 66	05:44:47.9	31.60 82.76	11	4.7	TP	SHL	10.0	Love
9	03 29 66	06:12:00.8	37.52 114.99	33	5.3	EC	SHL	23.0	S
10	09 28 66	14:00:21.0	27.53 100.08	12	5.7	TP	MSH	35.3	SS
11	03 14 67	06:58:04.4	28.41 94.29	12	5.8	EC	HKC	19.0	S
							ANP	24.5	S
							SHK	33.2	SS
							MAT	37.7	SS
12	08 15 67	09:21:03.3	31.05 93.56	10	5.5	TP	SHL	5.7	Love[1]
13	08 30 67	11:08:50.0	31.57 100.31	8	4.9	TP	NDI	20.2	Love[1]
							LAH	22.9	Love
14	09 15 67	10:32:44.2	27.42 91.86	19	5.8	EC	SHK	35.5	SS
15	12 22 68	09:06:35.0	36.25 101.83	21	5.5	TP	KBL	26.7	S
16	10 17 69	01:25:11.5	23.09 94.70	124	6.1	EC	SHK	35.0	SS
							MAT	39.7	SS
17	06 05 70	04:53:07.4	42.48 78.71	24	5.9 6.8	TP	HKC	35.7	SS
18	07 30 70	00:52:20.3	37.85 55.94	22	5.7	TP	HKC	52.0	SS
19	04 03 71	04:49:03.1	32.16 94.99	27	5.6 6.4	EC	MAT	35.7	SS
20	05 31 71	05:13:58.6	25.22 96.51	22	5.2 6.1	EC	MAT	37.3	SS
21	07 22 72	16:41:02.1	31.38 91.41	17	5.4 5.8	TP	NIL	15.5	S
							QUE	21.0	S
22	08 30 72	15:14:7.5	36.65 96.35	17	5.5 5.5	TP	NDI	17.9	Love
23	08 30 72	18:47:40.3	36.56 96.35	16	5.5 5.3	TP	QUE	25.3	S
24	02 07 73	16:06:25.8	31.50 100.33	8	5.9	TP	NDI	20.2	Love[1]
							NIL	22.9	Love
25	03 18 75	18:44:16.3	35.12 86.54	31	5.1 5.8	TP	QUE	17.2	S
26	05 05 75	05:18:46.3	33.13 92.84	8	5.6 6.1	TP	NIL	16.4	S
27	10 03 75	17:31:35.6	30.44 66.41	24	5.5 6.4	TP	ANP	48.6	SS
28	04 08 76	02:40:23.9	40.31 63.72	10	6.2 6.4	TP	ANP	50.0	SS
							HKC	46.0	SS
29	05 31 76	05:08:30.0	24.37 98.62	25	5.5 6.2	EC	ANP	20.8	S
							MAT	36.0	SS
30	05 31 76	18:35:05.0	24.29 98.68	20	5.1 5.5	EC	MAT	35.9	SS
31	07 03 78	08:46:32.0	32.75 94.08	8	4.7 4.9	TP	NDI	15.1	Love
31a	01 10 79	01:26:04.1	26.55 60.95	4	5.5 5.9	TP	TATO	54.1	SS
31b	01 16 79	09:50:06.9	33.96 59.53	10	5.9 6.7	TP	TATO	54.0	SS
32	03 15 79	12:52:26.0	23.18 101.09	6	5.5 6.2	EC	MAT	34.6	SS
33	05 20 79	22:59:11.6	29.93 80.27	16	5.7 5.7	TP	XAN	24.6	S
33a	07 09 79	10:57:22.0	31.45 119.24	10	5.4 5.7	TP	KAAO	41.9	SS
34	01 12 80	15:31:40.0	33.58 57.26	14	5.3 5.8	TP	HKC	51.0	SS
35	02 13 80	22:09:30.8	36.47 76.86	74	6.0 5.4	TP	GYA	27.2	S
							ANP	39.7	SS
36	02 22 80	03:02:43.7	30.66 88.65	10	6.0 5.4	TP	NDI	10.1	P_{nl}[2]
							NIL	13.4	P_{nl}
37	07 29 80	12:23:07.7	29.34 81.21	3	5.7 5.5	TP	LZH	20.1	S
							XAN	24.0	S
37a	03 02 81	12:13:46.2	22.88 121.47	28	5.4 6.2	TP	KAAO	47.0	SS
38	01 23 82	17:37:29.2	31.68 82.28	25	6.0 6.5	TP	LZH	18.4	S
39	06 15 82	23:24:28.8	31.85 99.92	7		TP	NDI	20.2	Love[1]
40	04 18 83	10:58:49.1	27.78 62.07	44	6.4 6.3	TP	SEO	54.5	SS
							HKC	59.7	SS
41	12 16 83	13:15:57.3	39.34 72.96	35	5.7 5.9	TP	BAG	47.2	SS
42	02 01 84	14:22:09.2	34.57 70.48	44	5.9 5.9	TP	ANP	44.8	SS
							TATO	44.9	SS
43	10 26 84	20:22:21.8	39.15 71.35	7	5.9 6.2	TP	HKC	40.1	SS
							ANP	44.2	SS
44	10 29 85	13:13:40.0	36.75 54.81	13	6.0 6.0	TP	GZH	51.8	SS

[1]Holt and Wallace, 1989; [2]this study. TP Tibetan Plateau; EC Eastern China.

waveforms are corrected by using teleseismic S-waveforms as the source time history since the ray parameter changes very slowly with distance for distances greater than 15.0 degrees. The orientation of the fault effects the amplitude ratio of SS- to S-waves, which was not used. These various approximations have been used in previous $SS-S$ studies, see for example Rial et al. (1984).

The crustal velocity structure has not been well determined in the Tibetan Plateau. To constrain this portion of the model we used relatively high-frequency Love waves. But instead of applying the conventional dispersion analysis, we chose to match the Love-wave synthetics to the observations directly. The appropriateness of the model is then judged on the overall fit of the synthetics to the observed waveform in absolute travel time.

Since Love wave data are not normally used in this fashion, we start with a brief sensitivity study to test the resolving power of this approach by discussing some numerical experiments. Figures 3 and 4 summerize the results of these numerical experiments. Figure 3 shows the sensitivity of synthetics to changes in the models, source depths, and source mechanisms. Figure 4 displays the synthetics appropriate for different Moho discontinuities.

In Figure 3, the left column are the models used to generate the synthetics of fundamental Love waveforms at various depths and mechanisms. These synthetics were generated at a distance of 1000 km, assuming a the source time history of a (1, 1, 1) trapezoid. All synthetics begin at 260
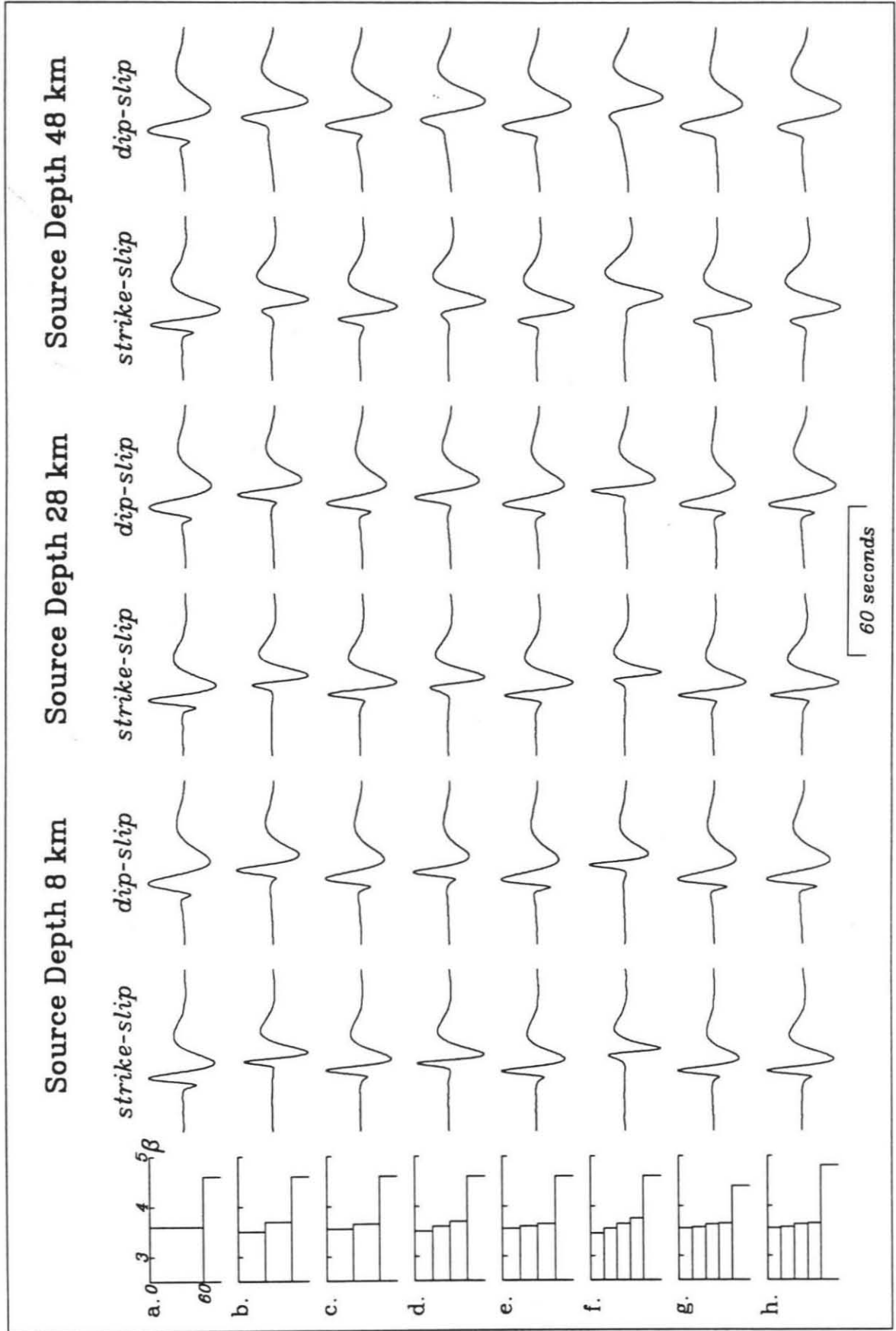
Figure 3. Fundamental Love wave synthetics for a variety of models, source mechanisms, and depths. The column on the left are the models used to generate the synthetics on their right. The crustal thickness is 60 km, and the average velocity of the crust is 3.6 km/sec. The velocity of the mantle is 4.6 km/sec, except for models g., 4.4 km/sec, and h., 4.8 km/sec. The distance is 1000 km, and the source function is a trapezoid (1, 1, 1) .

a) Crustal Thickness 40 km

S_n

b) Crustal Thickness 50 km

S_n

c) Crustal Thickness 70 to 40 km

S_n

d) Crustal Thickness 70 to 35 km

35 km   25 km

35 km

S_n

e) Crustal Thickness 60 km

S_n

f) Crustal Thickness 70 km

β_1 3.6 km/sec   31.8 km

β_2 3.8 km/sec

β_m 4.6 km/sec

S_n

1000 km

240   260   280   300

Travel Time (sec)
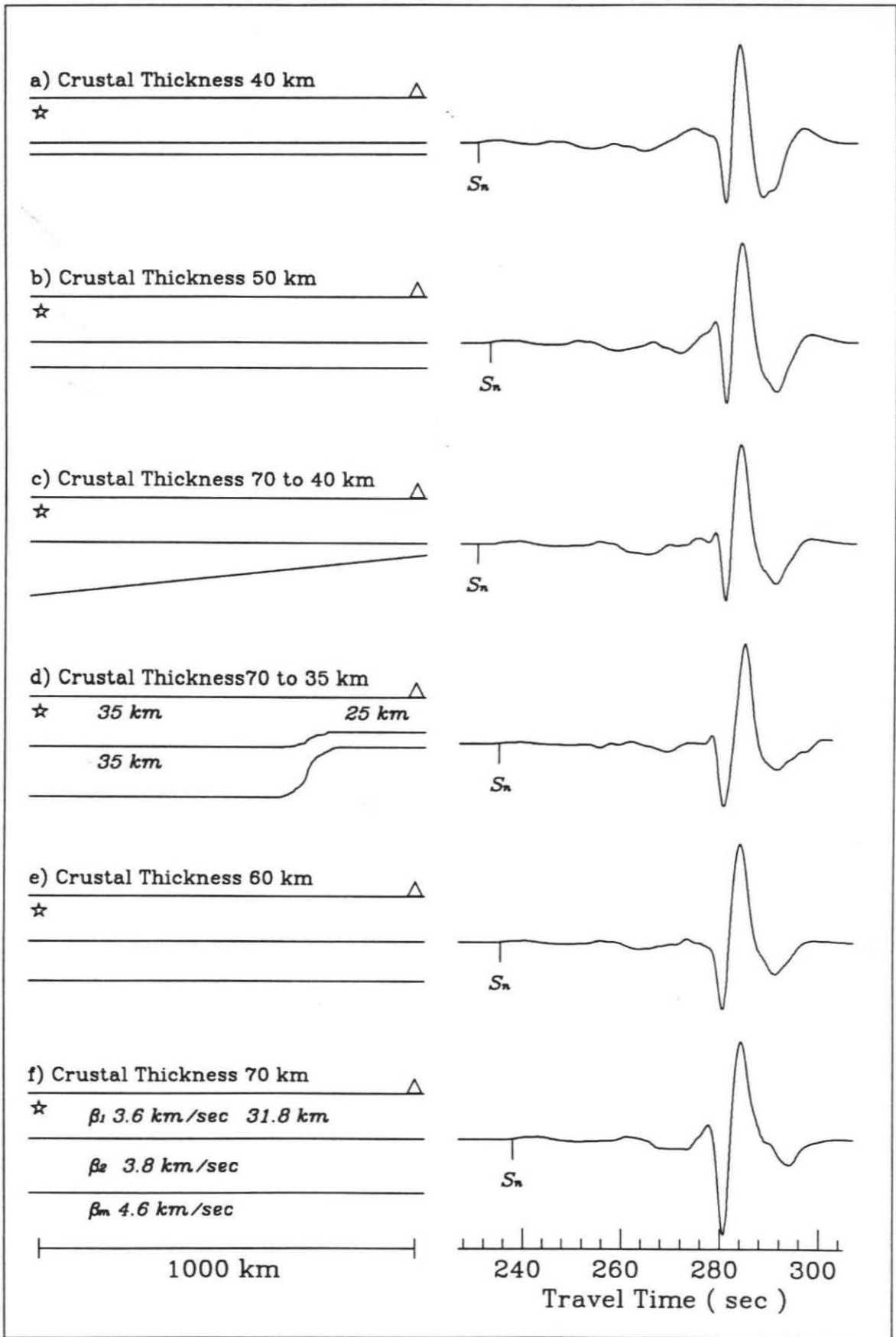
Figure 4. A comparison of Love wave synthetics for different models. The column on the right displays the synthetics derived from the models on the left. The models are of a two-layer crust over half space mantle. The shear velocities of the upper layer is 3.6 km/sec, that of the lower layer is 3.8 km/sec, and that of the mantle is 4.6 km/sec. Except for model d), the models have a 31.8km thick upper crust. The star is the source, and the triangle is the receiver. A strike-slip source, with a Gaussian time history, half width 1.26 seconds, is used. Source depth is 9.8 km, distance is 1000 km.

seconds. The crustal thickness is 60 km for all models. The average velocities of the crust are same, 3.6 km/sec. The mantle velocities are same, 4.6 km/sec, except models g which is 4.4 km/sec and h which is 4.8 km/sec. The attenuation, Q_β, used is 300 for the crust, and 1000 for the mantle. Comparing the synthetics for these various sensitivities we conclude that: the mantle velocity has very little effect on both travel time and waveforms, see the synthetics of models g and h; the velocity of the upper crust seems to dominate the travel time of Love waves, see models b, c, f and g; the velocity gradient does not have much effect on waveforms; the source depth has a profound effect on the waveforms for complicated crustal models, and less effect for simpler models; source mechanism effects travel time only weakly compared to shallow velocity structure.

Figure 4 displays some properties of regional Love waves when crossing a plateau boundary similar to the expected geometry of the Tibetan Plateau. The column on the left displays the source-receiver geometry in a simple idealized crust where all the models have the velocities given at the bottom. The distance is set at 1000 km, and strike-slip source is assumed at a depth of 9.8 km. These synthetics were generated with generalized ray theory and finite-difference method, see Helmberger and Vidale (1988). The Love-waveforms are quite similar which lead us to conclude that the crustal thickness and dipping Moho do not. Thus, regional Love waveforms can be used as a constraint on the velocity structure of the upper crustal layers for paths crossing the plateau with the above restrictions on geometry.

RESULTS

The upper mantle shear velocity structures we derived are given in Table 2 and Figure 5. TIP is the model for the Tibetan Plateau, and ECH that for the eastern part of China, part of Yangtze and Sino-Korean Cratons.

Tibetan Plateau

It is convenient to break this discussion into two sections, namely crustal and upper-mantle, where the former is constrained by regional long-period Love waves and the latter by $S-$ and $SS-$waveform data.

Crust

Our preferred velocity model is given in Table 2 with a 3.75 km surface layer of 2.55 km/sec (same as that of Chen and Molnar (1981)), followed by a 16.25 km of 3.5 km/sec, 20 km of 3.7 km/sec, and 30 km of 3.8 km/sec.

The source-station paths used in this Love wave investigation are given in Figure 6, along with two P_{nl} paths discussed later. It is difficult to measure the initial arrival time of Love waves, so the first large pulse was used to denote relative timing and the synthetic has been aligned accordingly. Figure 6 indicates the number of seconds the synthetic is faster than the observed for that particular ray path. The comparison of the data and synthetics is given in Figures 7, and 8.

In Figure 7, we display the data, whose source mechanisms are known

Table 2
Velocity models for Tibetan Plateau (TIP)
and Eastern China (ECH)

Depth (km)	TIP (km/sec)	ECH (km/sec)	Depth (km)	TIP (km/sec)	ECH (km/sec)	Depth (km)	TIP (km/sec)	ECH (km/sec)
0	2.550	3.450	150	4.550	4.440	290	4.705	4.668
3.75	3.500	3.450	160	4.550	4.467	300	4.708	4.675
10	3.500	3.700	170	4.590	4.484	310	4.712	4.682
20	3.700	3.800	180	4.625	4.501	320	4.715	4.695
30	3.700	3.850	190	4.658	4.518	330	4.718	4.710
35	3.700	4.650	200	4.668	4.535	340	4.721	4.720
40	3.800	4.650	210	4.675	4.552	350	4.725	4.730
70	4.600	4.600	220	4.680	4.569	360	4.730	4.740
80	4.600	4.550	230	4.685	4.586	370	4.740	4.750
90	4.600	4.500	240	4.690	4.603	380	4.750	4.760
100	4.600	4.450	250	4.690	4.620	390	4.760	4.770
110	4.600	4.400	260	4.693	4.637	400	4.770	4.770
130	4.550	4.400	270	4.697	4.654	405	5.014	5.014
140	4.550	4.420	280	4.701	4.660	425	5.050	5.050
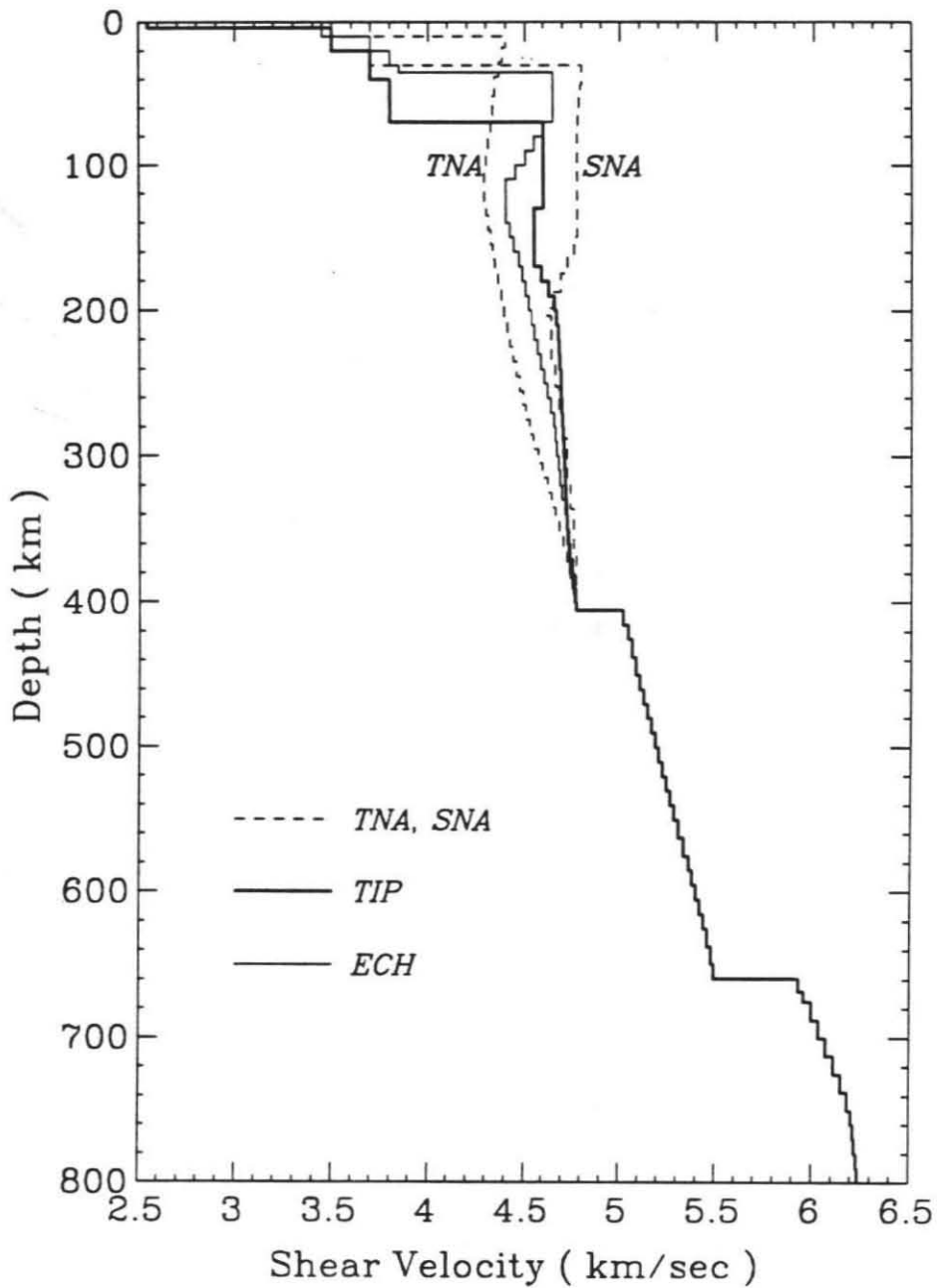
Figure 5. Shear velocity models TIP (Tibetan Plateau) and ECH (southeastern part of China) derived in this study compared to profiles of the Canadian shield (SNA) and the tectonic western North America (TNA).
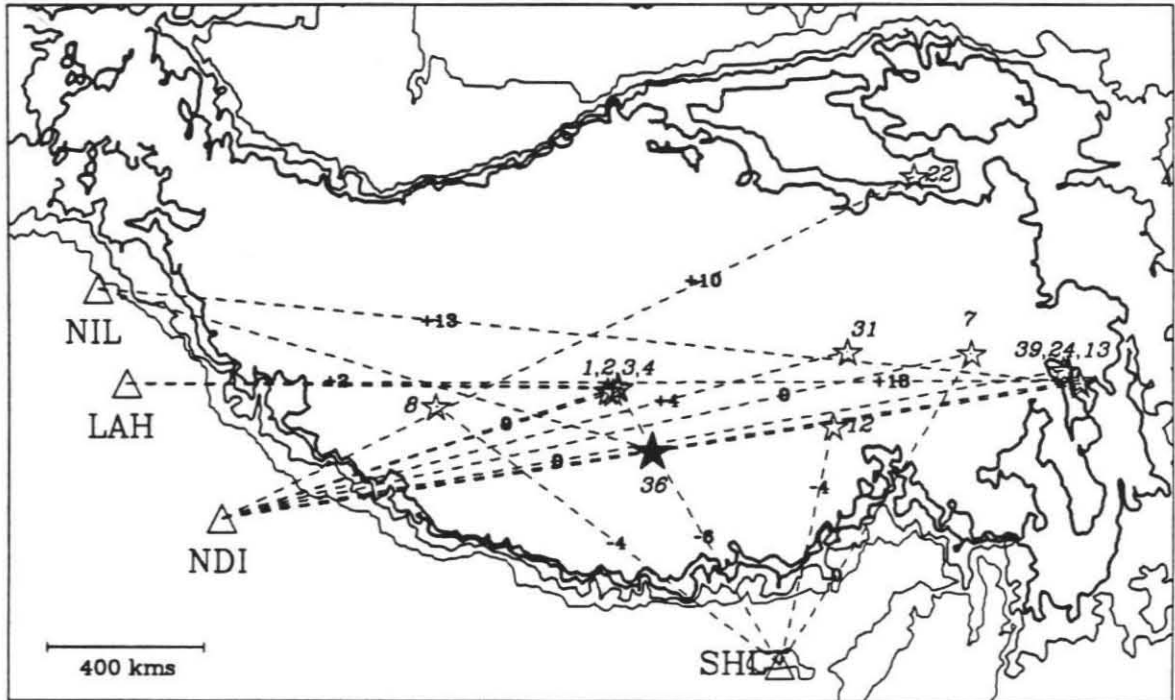
Figure 6. The ray paths of Love wave data used to derive the velocity distribution of the crust of the Tibetan Plateau, where the stars are sources, and the triangles are stations. The numbers are the differential maximum amplitude travel times of the data compared to the synthetics. The + sign means the model is faster in seconds. The number beside the source is event number of Table 1. The iso-bath relief contour lines with altitude of 1000 meters, 2000 meters, 3000 meters and 4000 meters are given to define the physical boundary of the Tibetan Plateau. The dark star, event 36, is the location of the P_{nl} wave source.

60.0 seconds
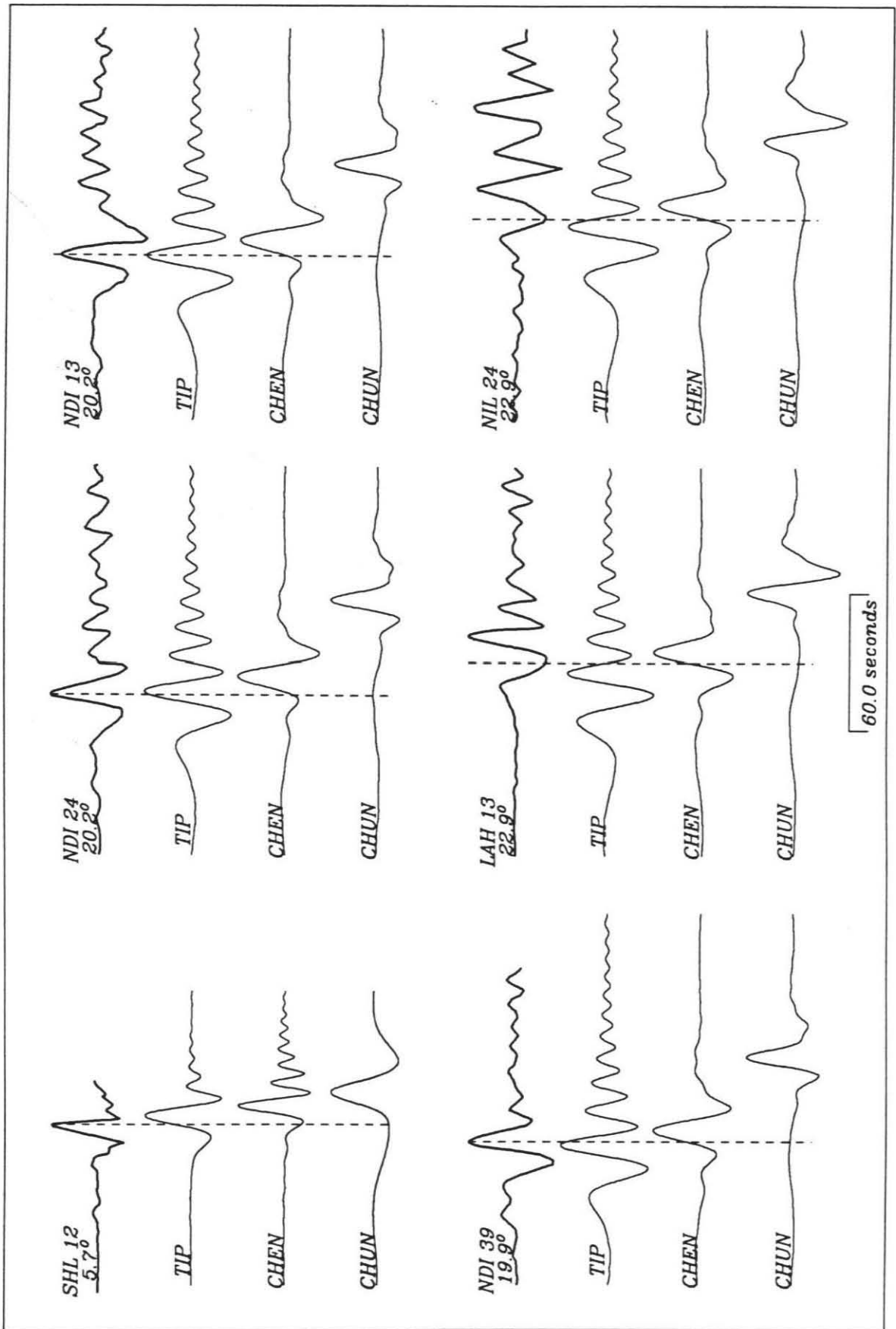
Figure 7. Synthetic comparison of different models with the data from known source parameters. In each group, the first trace is data with station name and event number in Table 1, along with the distance. The second, third and fourth traces are the synthetics of models TIP, CHEN, CHUN respectively.
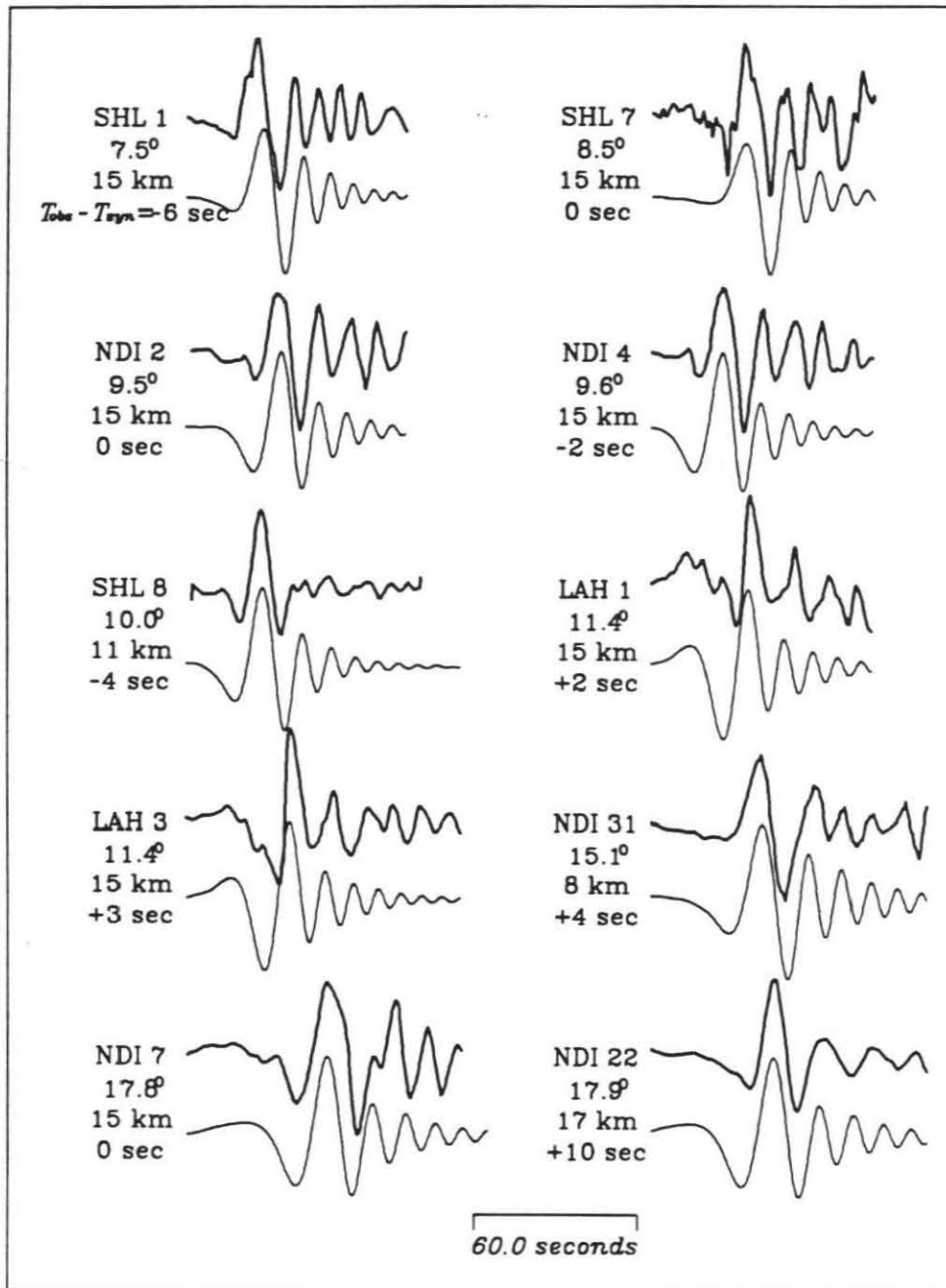
Figure 8. The Love wave data for paths shown in Figure 6 compared with the synthetics. Upper traces are the data, the lower ones are synthetics when the amplitude are normalized, and shifted by the amounts indicated by $T_{obs} - T_{syn}$. On the left of each comparison are the station names and the event number given in Table 1 followed by the distance, source depth and $T_{obs} - T_{syn}$.

(Holt and Wallace, 1989), along with the synthetics of proposed models, where TIP indicates the synthetics appropriate for the model developed in this study, CHEN associated with model S7 of Chen and Molnar (1981), and CHUN computed from the model derived by Chun and McEvilly (1985). The data and synthetics are displayed in absolute travel time. From this figure, the waveform matches of TIP are better than the others, and the travel times at stations NDI and SHL are better. However, for the paths of event 24 to NIL, and event 13 to LAH, the travel times of TIP are 13 seconds faster than the data and are not as good as CHEN. CHUN is slow. In Figure 8, the time shift was applied for each comparison. In this figure, the depth used to generate the synthetic is given. The depths may be different from the corresponding ones given in Table 1. Because the source depth is poorly known, we just compared the data of unknown source depth with the data of known source depth to estimate the source depth. The basic assumption is that, the source depth should be roughly the same if the two data are roughly alike. A strike-slip source with a time history (2, 2, 2) trapezoid was used to generate all synthetics. From these two figures, the travel times and the waveforms fit the data reasonably well, although TIP is faster, or slower for certain paths. We consider this model to be an average velocity distribution of the crust of the Tibetan Plateau which is considerably faster than previous proposed models.

Upper-mantle

The upper-mantle shear velocity distribution of the Tibetan Plateau

beneath the crust is constrained by 11 S-waveforms with distances from 15.5° to 27.2°, and 16 $SS-S$ waveforms with distances from 35.3° to 59.7°. Some of the S-wave data is from Lyon-Caen's paper (1986), and some of the $SS-S$ wave data is from Wang and Yao's paper (1989). The travel times of the S-waves are not used, for they are rather scattered, and a large portion of their paths lie outside the Tibetan Plateau. Note that the $SS-S$ waveform data is controlled by triplication positions or differential times where rays share common paths near the source and receiver and thus much less suspectable to travel time offsets caused by lateral variation (Grand and Helmberger, 1984a). The ray paths of the S-wave data and the bounce points of the SS-wave data are given in Figure 9a. The triangles represent the stations; stars the events generating the S-waves; circles the bounce points of the SS-waves for distances greater than 45 degrees; and squares the bounce points of the SS-waves for distances less than 45 degrees. In order to avoid the strong lateral heterogeneity, we did not use the SS-wave data with bounce points near the boundary of the Tibetan Plateau.

The starting model for the upper mantle shear velocity structure of the Tibetan Plateau is TNA (Tectonic North America, Grand and Helmberger, 1984a), with the crustal model derived above. After comparisons of synthetics and the data for several dozens of models, following a trial-and-error procedure, we obtained model TIP, see Figure 5 and Table 2. This model has a 60 km thick lid of 4.6 km/sec, and 40 km of 4.55 km/sec below. It does not have a distinct low velocity zone, and is shield-like below.

Figure 10 shows the comparison of the observed waveforms with syn-
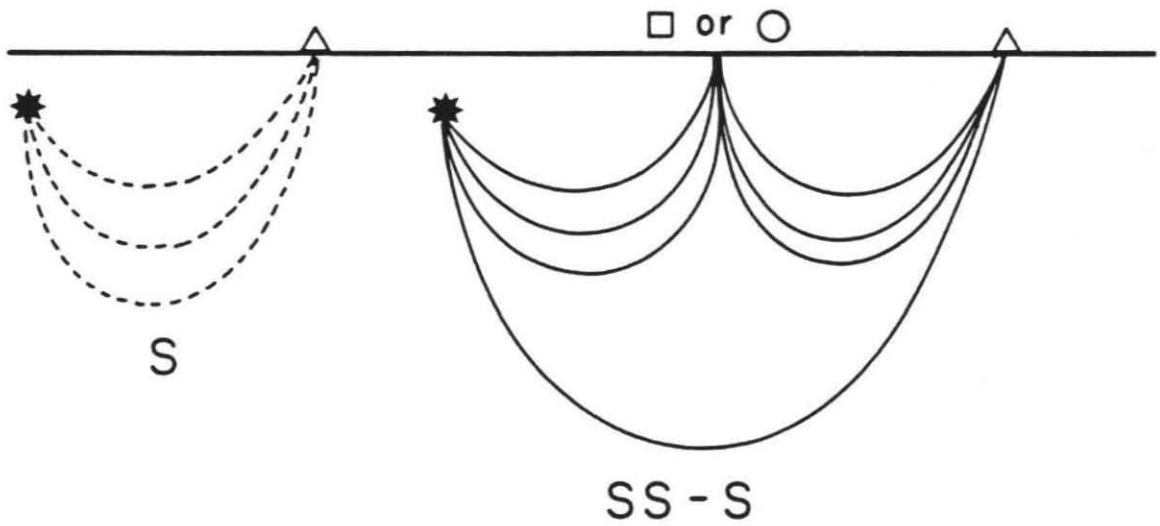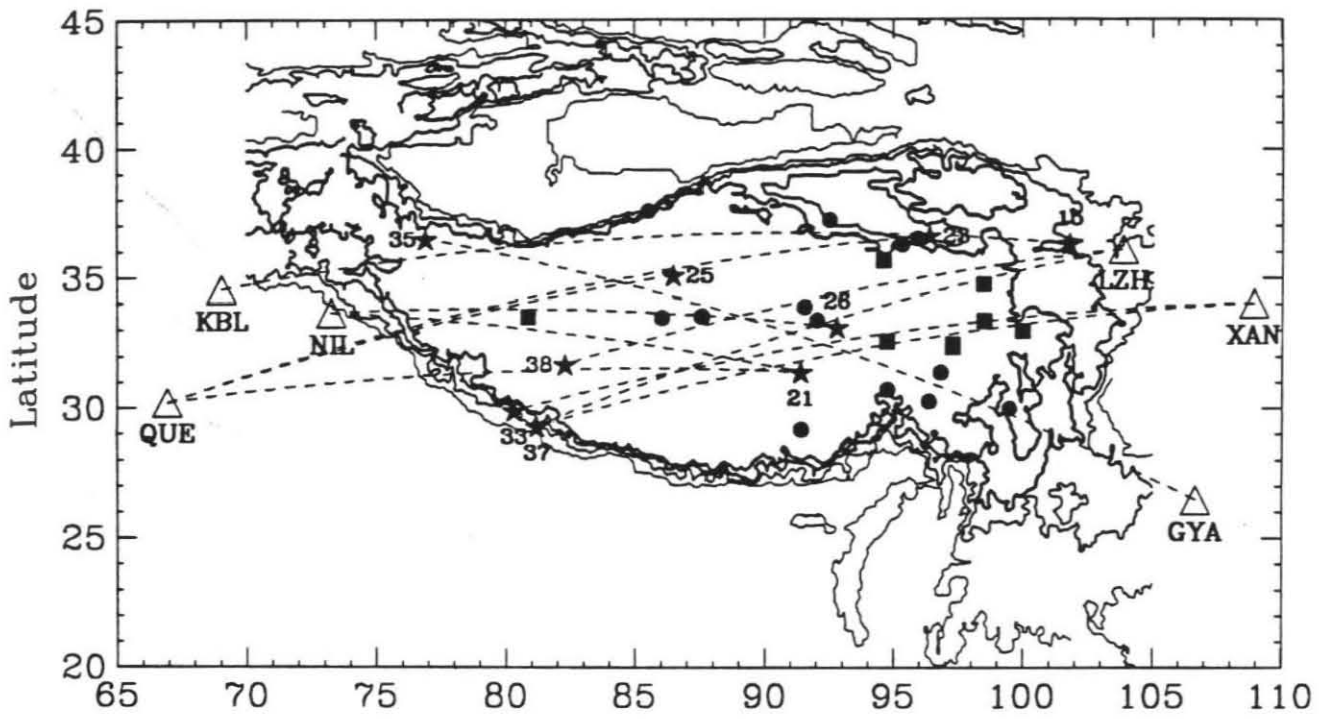
Figure 9. (a): The ray paths, dotted lines, of S wave data, and the bounce points of the SS wave data used to study the upper mantle shear velocity structure of the Tibetan Plateau. Circles represent the source-receiver distances greater than 45°, squares less than 45°, Stars are sources, and triangles are stations. The solid lines from thin to thick are contour lines with 1000 meters, thinnest, 2000 meters, 3000 meters and 4000 meters, thickest, above see level. The number beside the source is event number in Table 1. (b): Schematic illustration of rays producing S waveforms (left), and SS waveforms (right).

30.0 seconds
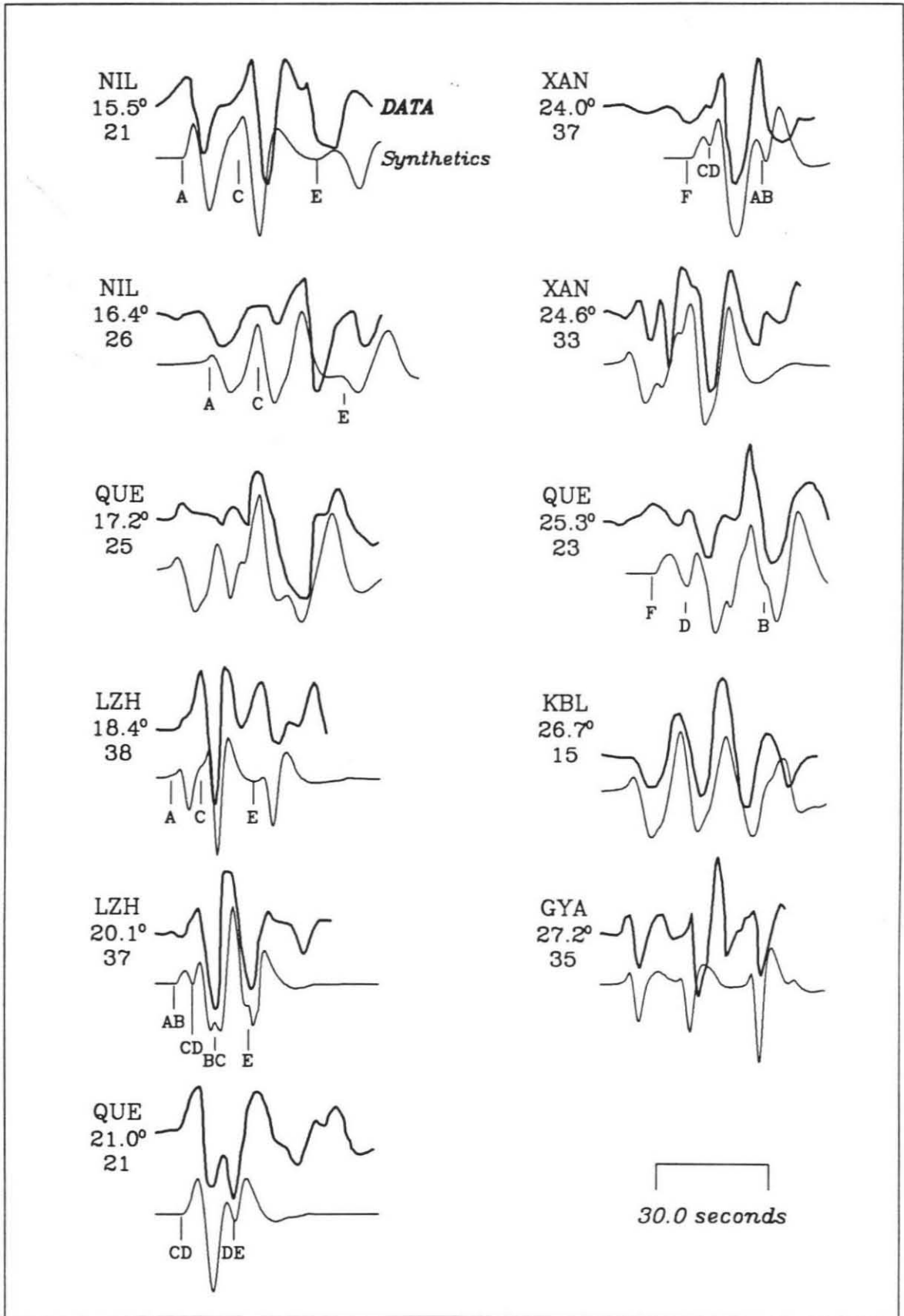
Figure 10. The comparisons of the waveforms of the *S*-waves for the paths of the Tibetan Plateau with the synthetics using the model TIP. " A ", " B ", " C ", " D ", " E " and " F " are the branch names of the corresponding arrivals (Figure 11). On the left of each datum-synthetic comparison, are station names, distances and event number.

thetics. Because most of the S-wave data does not correspond to pure paths and sample areas with large heterogeneities, it is difficult to say which part of the data gives the most definitive information about the Tibetan Plateau. However, by comparing the paths indicated in Figure 9a we see that the shallowest structure is sampled best by the western station, NIL. Almost all of the data and synthetics have three arrivals that are due to three sets of rays, one bottoming above the 405 km discontinuity (branch AB), one bottoming below the 405 km discontinuity and above the 670 km discontinuity (branches BC and CD), and another bottoming below the 670 km discontinuity (branches DE and EF). We will generally refer to branches by single letters, which will denote the two arrivals forming the cusp designated by the letter (Figure 11). With long-period data the two geometric arrivals forming a branch usually cannot be distinguished. When there is possible confusion in the branch name, we will indicate a full designation. A good fit of the waveforms and, therefore, differential travel times of branches A, B, C, D, E and F to the data at distances of $17.2°$, $20.1°$, $24.0°$, $24.6°$, $25.3°$, and $26.7°$ is achieved. Note that the A branch is missing from the LZH data ($18.4°$) indicating a shallow heterogeneity along the path (Grand and Helmberger, 1985). The differential travel time between the branches A and C of the data recorded at NIL at a distance of $15.5°$ is 3.5 seconds faster than that of the synthetics, and that of the data also recorded at NIL at a distance of $16.4°$ is 2 seconds faster than that of synthetics. Perhaps these differences were caused by the local faster structure and thinner crust thickness near the station NIL. The amplitude of the E branch for QUE data at a
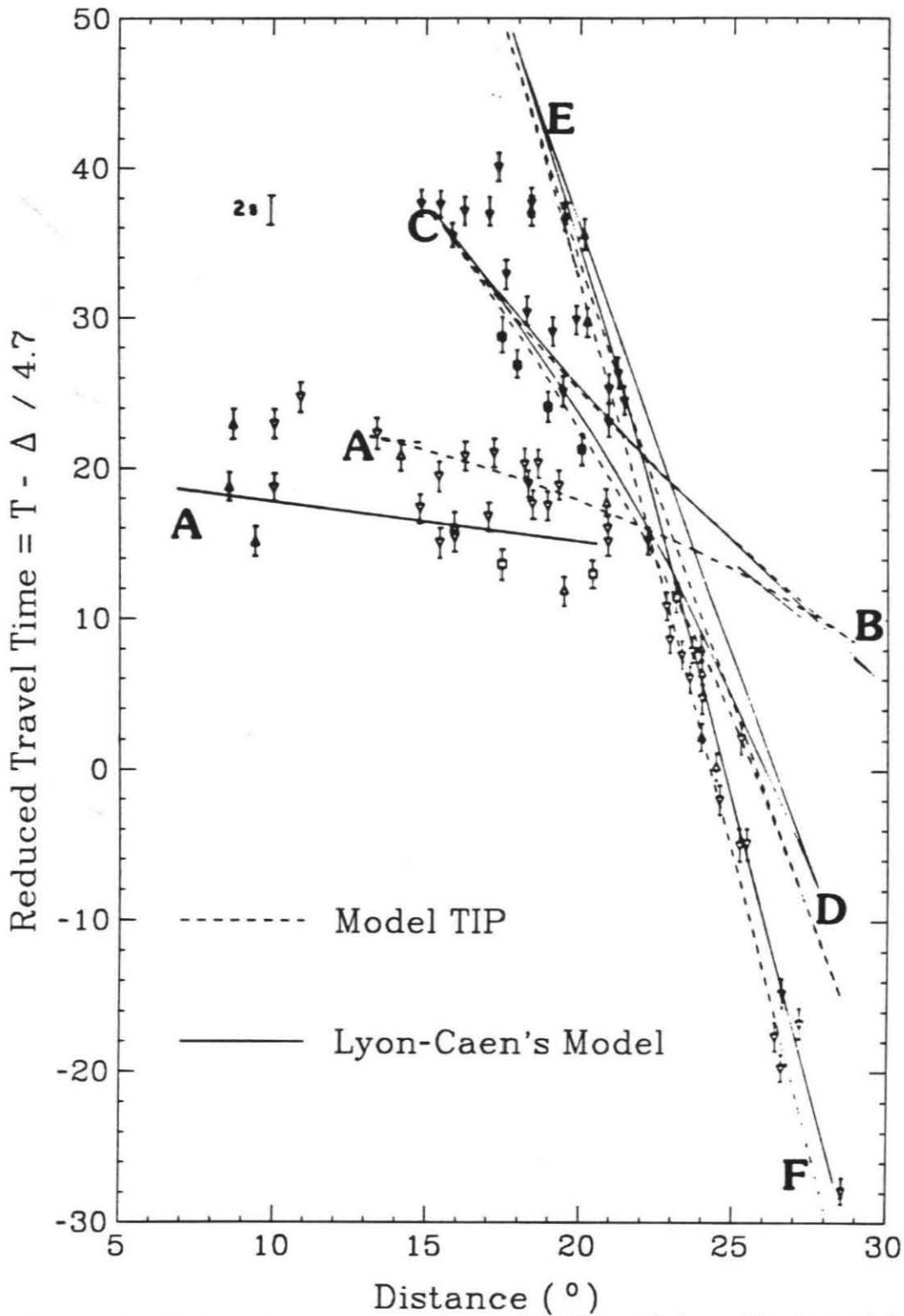
Figure 11. Triplication curves of the model TIP and Lyon-Caen's model, and Lyon-Caen's travel time data of S waves for the Tibetan Plateau paths. The different symbols indicate the properties of the path (Lyon-Caen, 1986, Figure 8).

21.0° could be due to the missing A branch.

The travel times and waveforms of S-waves alone do not yield definitive constraints on the velocity distribution of the Tibetan Plateau, because a large part of the ray paths are outside the region. Figure 12 shows the $SS-S$ wave data with synthetics of the model TIP. The fits of the waveforms and differential travel times between the first and the second arrivals (F and D branch), and the S-wave of the data recorded at SEO at a distance of 54.5 degrees with the synthetics indicate that the shear velocity distribution beneath the 405 km discontinuity is the same as that beneath the Canadian Shield (Grand and Helmberger, 1984). The source functions used for the synthetics of SS waveforms are the teleseismic S waveforms. The advantage of using the teleseismic S-waveform as a source function is that the importance of the source mechanisms and source depth is almost completely eliminated. The waveforms of S-waves are the sum of direct S- and sS-waves. The travel time difference between these two phases is controlled by the source depth and the ray parameter, or take-off angle. The amplitude ratio is determined by the source mechanism (Langston and Helmberger, 1975). The different S-waveforms at different distances are due to the ray parameters. The ray parameter changes very slowly with distance beyond 15 degrees, becoming nearly a constant for distances beyond 25 degrees. Thus the effects of source depth and source mechanism are almost the same on triplication S-waves as on teleseismic S-waves.

The differential travel time of the C branch and S-wave of the data recorded at MSH at a distance of 35.3° is about 5 seconds faster than that of

100.0 seconds
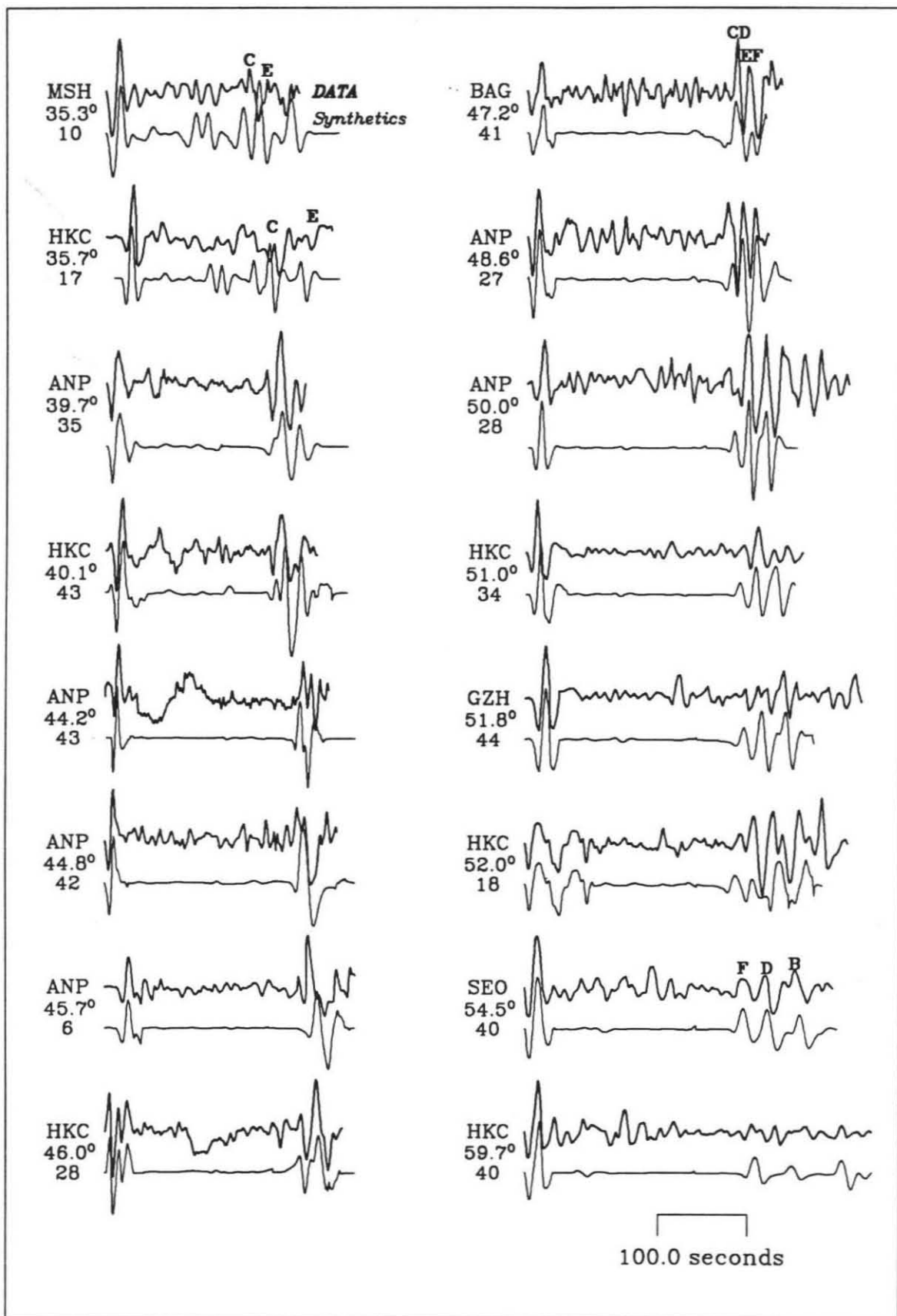
Figure 12. *SS-* and *S-*wave data for the paths with midpoints in the Tibetan Plateau and the synthetics of the model TIP. The *S-* waves are aligned with synthetic *S-*waves. When the observed *S-*waveforms are used as the source function. On the left of each data-synthetic comparison, are station names, distances and event number.

the synthetics, and the branch A is absent. The bounce point for it is the far west point indicated in Figure 9a. The ray of the C branch in this case travels almost entirely in the upper 405 km with only a very small part of it going below the 405 km discontinuity. A large part of the time difference is due to the more than 10 degrees of horizontal travel distance in a shield-like region (Rial et al., 1984) outside of the Tibetan Plateau. Also, the lateral heterogeneity could cause some difference in the differential travel time of SS- and S-waves. The differential travel times and waveforms of SS- and S-waves of the HKC (35.7°) data, see Figure 12, are matched very nicely for the branches C and E, although the A branch is not clear. The beginning waveform of the HKC station at a distance of 52.0° is most likely S. If it is a combination of S and sS, the source depth should be about 80 km, and the amplitude of the second one would not likely be so big. If we use all of the beginning waveform as the S-wave, or source function, the synthetics for the SS-wave are very good, but we could not label the branches. The waveforms of the SS-waves of HKC at a distance of 51.0° do not agree well with that of the synthetics, but the match of the differential travel time is not bad. The arrival between the S- and SS-waves on the data HKC 51.0°, GZH 51.8°, HKC 52.0°, SEO 54.5°, and HKC 59.7° is the phase ScS.

The synthetic fits to this dataset proved particularly difficult. The reason is in the inherent complexity of the structure itself in terms of heterogeneity. Nevertheless, it appears that the derived model for the structure beneath the Tibetan Plateau fits the $S-SS$ waveform data better than existing models, as will be discussed in more detail later.

Eastern China

The data coverage of the eastern portion of China is presently lacking but will become more complete when the new digital array becomes operational. The ray paths of the data used for the study of Eastern China are displayed in Figure 13. It is clear from the figure that the region sampled includes the Yangtze Craton and the southern half of the Sino-Korea Craton. Although the region is relatively complex, we will assume a uniform upper-mantle structure as a first order approximation of the area. The data set we used to constrain the upper mantle shear velocity distribution includes 5 S-wave data , distances from 19.0° to 24.5°, and 10 SS-wave data, distances from 33.2° to 39.7°. The model, ECH, we obtained, is given in Table 2 and Figure 5. The comparisons of the synthetics with the data are given in Figure 14 and Figure 15.

In Figure 14, we display synthetic and S- wave observation comparisons along with the theoretical responses and source function estimates. The branches are identified on the theoretical responses similar to Figure 10 discussed earlier. Although all the branches cross each other in this distance range, we can see pulses of branches on both the data and the synthetics. The travel time of the synthetics is 3 seconds faster than that observed at HKC (19.0°), 3 seconds slower than that of ANP (20.8°), 4 seconds slower than that of SHL (22.9°), 7 seconds slower than that of SEO (23.2°), and 9 seconds slower than that of ANP (24.5°) (Figure 13). The fit of the travel times is certainly reasonable for such a big laterally heterogeneous area. The synthetics are produced by convolving the theoretical responses (Earth
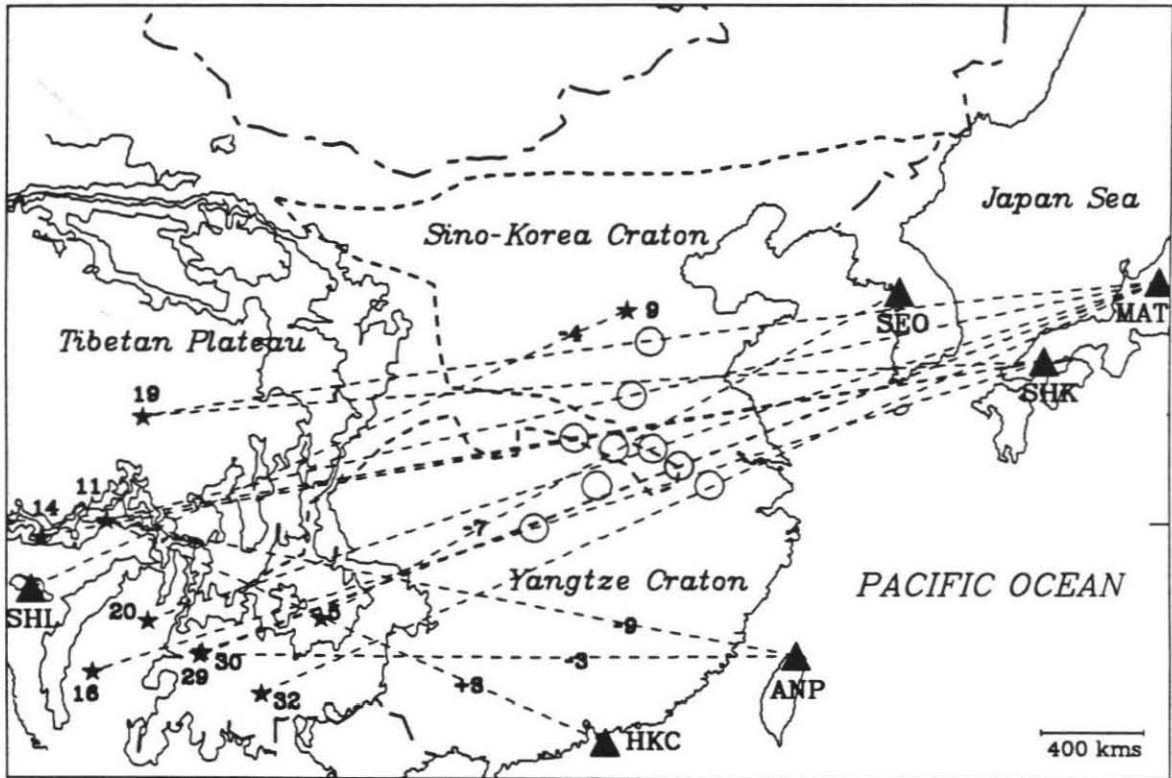
Figure 13. The ray paths of the *S-* and *SS-*wave data used to derive the upper mantle shear structure of the southeastern part of China. The stars are sources, and the triangles are stations. Circles indicate the midpoints of the *SS* data. Numbers near stars are event numbers, same as in Table 1. Numbers with " + " or " - " sign on the rays of *S-* waves are the differential travel times of the data relative to the synthetics using the model ECH. The symbol + means that the model is faster than the data.
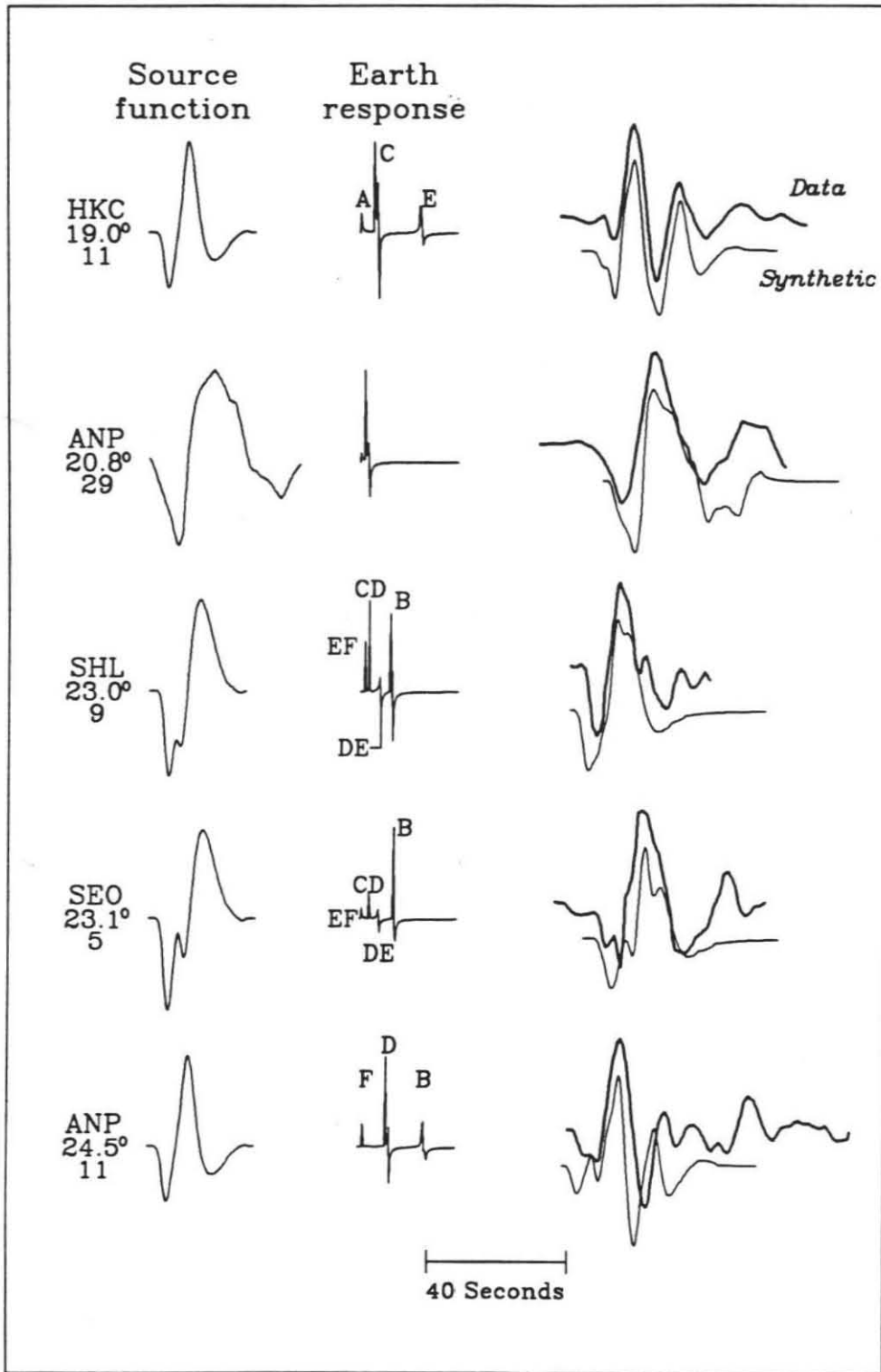
Figure 14. *S* data for the paths of southeastern China and the synthetics using the model ECH. Numbers below the distances are event numbers as displayed in Table 1. They are lined up with maximum amplitudes.

responses) with the effective source functions which contain sS . The source function of ANP (20.8°) is the S-waveform observed at MAT (36.0°, Figure 15). The other source functions are theoretical predictions assuming a strike-slip at SHL and SEO, and a dip-slip at ANP and HKC. The bottom two observations at SEO and ANP, showing the interference of F and D branches, are very similar to those displayed in Figure 17 of Grand and Helmberger (1984a).

Figure 15 gives the comparisons of the synthetics of SS-waveforms and the data. The SS-waveform recorded at a distance less than 45° gives not only information about the bounce point, but also information about a large part of the upper mantle structure along the ray path. All of the SS-wave data we have used are less than 40°, so this may cause some difficulties for the large lateral heterogeneity. Also it is difficult to locate the E, F branches of the model. The complexity of the waveforms of SHK (35.0°) is due to the depth of the source, 134 km. We have not matched sS- and sSS-waves, so the synthetic is incomplete. Note that 7 of the 10 seismograms used are recorded at MAT, and one third of their ray paths lie out of continental China (Figure 13). Actually, for some of the SS-wave data, only one third of their paths and bounce points are in the eastern part of China, Yangtze Craton, and the south half of the Sino-Korea Craton. It can be inferred from the data and the synthetics (Figure 14, and Figure 15) and the travel time residuals (Figure 13) that the velocity of the Sino-Korea Craton is faster than that of the Yangtze Craton, and that the northern part of Yangtze Craton is faster than the southern part. The model we derived here
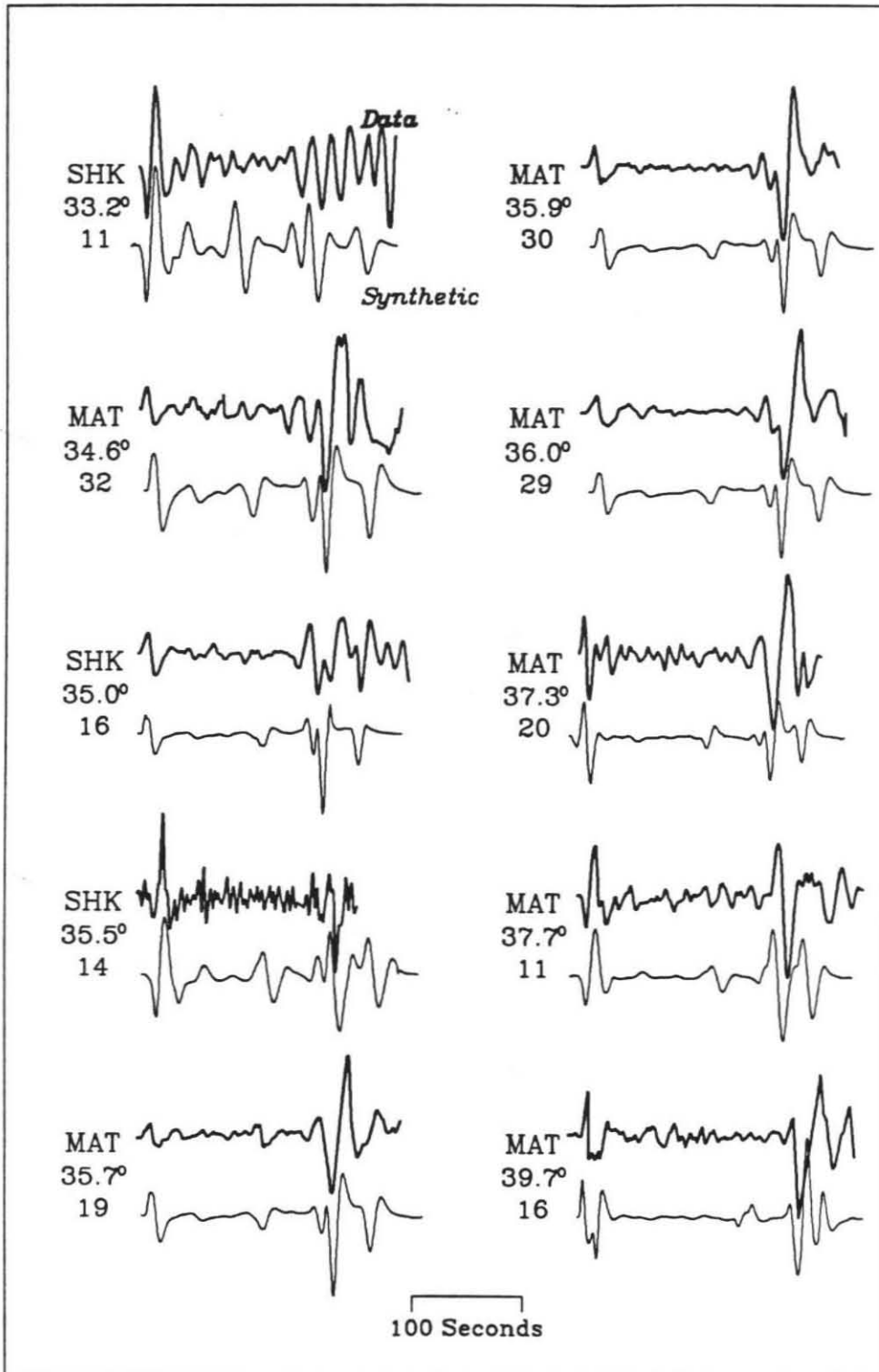
Figure 15. *SS* and *S* data for the paths with midpoints in southeastern China, and the synthetics using the model ECH. The *S* waves are aligned with synthetic *S* waves.

is, obviously, only a very approximate model for the upper mantle shear velocity distribution for the eastern part of China. Nevertheless, these preliminary results suggests that the mantle beneath eastern China is predominantly shield at depths greater than a few hundred kilometers. The large travel time off-sets suggest strong shallow lateral variation. More data will be required to resolve the connection with the surface geology and interplate interaction.

DISCUSSION AND CONCLUSION

In this section we will briefly compare synthetics associated with existing models (Figure 16) proposed for the Tibetan Plateau with some of the key $SS-S$ observations. The $SS-S$ data is the least contaminated by lateral variation as discussed earlier and thus the most definitive. This will be followed by an indepth discussion of the upper 200 kms of the models since this is the region where models differ the most and are the most significant in terms of tectonic implications. The waveforms of $SS-S$ waves are the results of the interference of the five branches AB, BC, CD, DE and EF (Figure 11). Since the travel time branches are nearly straight lines, we can get a shear velocity model for a homogeneous structure if we have two ideal waveforms of $SS-S$ waves at a distance near 30 and 60 degrees. We present three key data taken from Figure 12, located at roughly 10° intervals, namely, HKC at 35.7°, ANP at 44.8°, and SEO at 54.5° in Figure 17. The waveforms of SEO at 54.5° are particularly meaningful, because waveforms of the different branches have separated. At ANP the branches
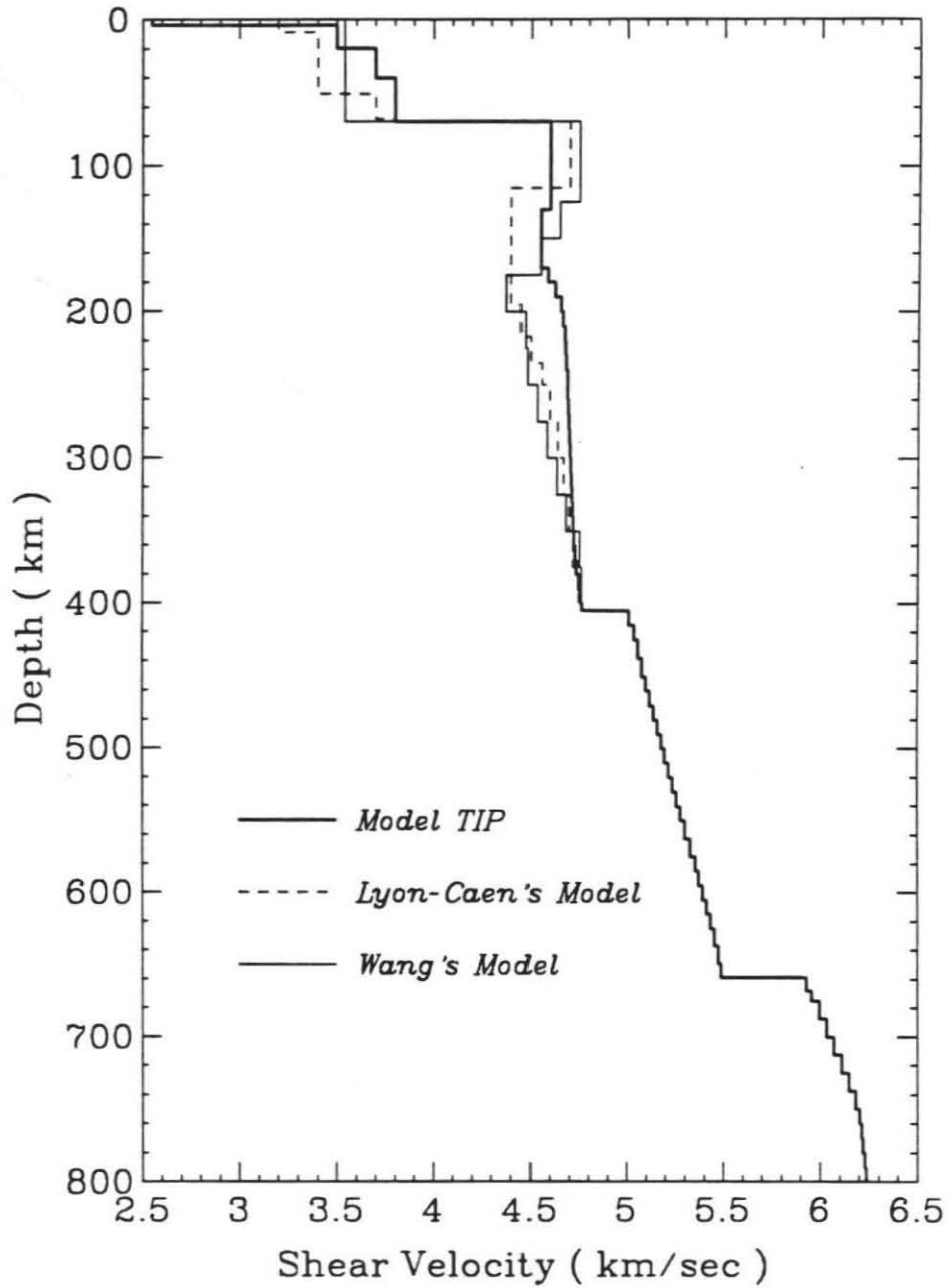
Figure 16. Comparison of the existing models for the Tibetan Plateau.
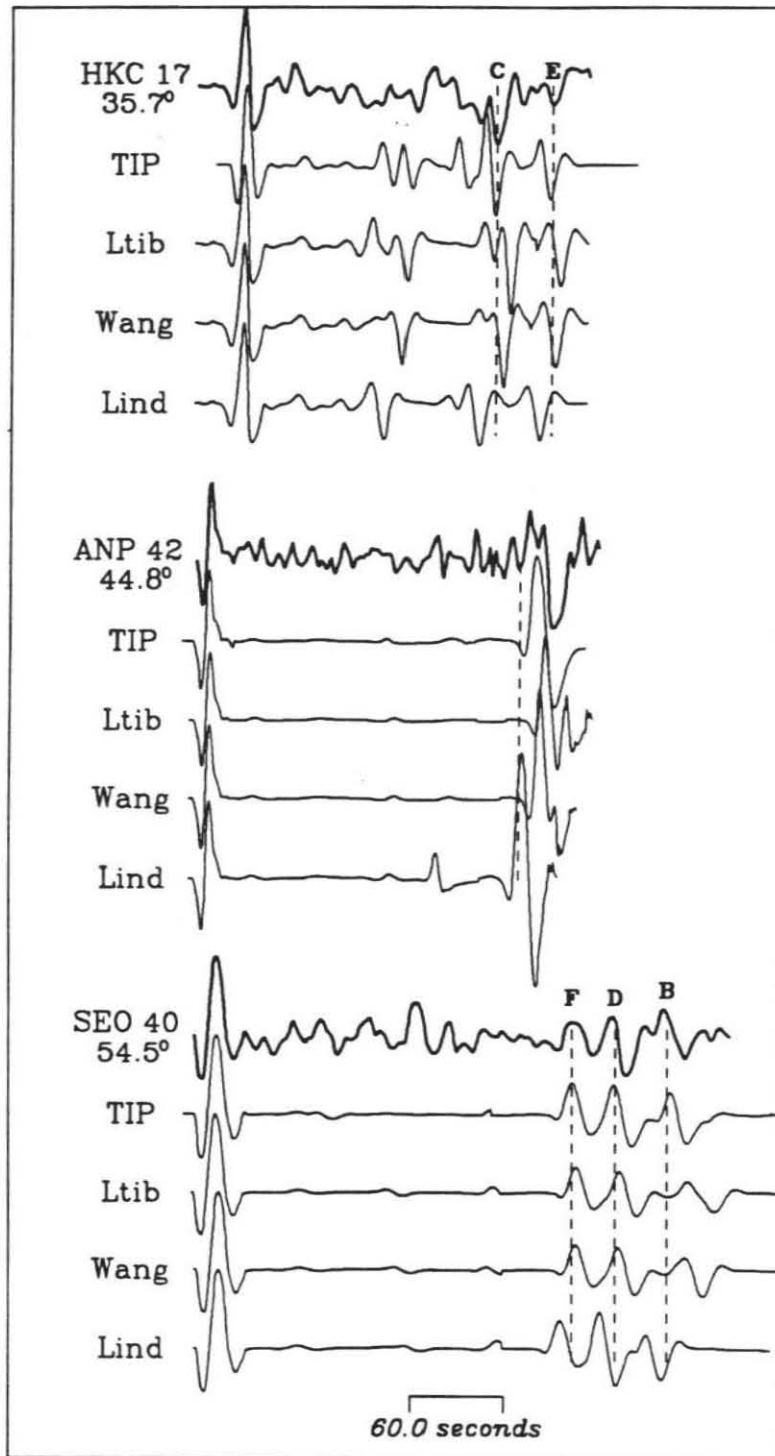
Figure 17. Comparison of the data and synthetics of models TIP, Ltib, Lind, and Wang's model. Ltib is Lyon-Caen's model for the Tibetan Plateau, Lind is Lyon-Caen's model for the Indian shield. Letters on top of the data are the branch names (Figure 10).

are all together. In order to see clearly the differences between the data and synthetics, we have inserted the vertical lines. The bottom four traces of each group are synthetics for proposed models for this region.

Comparing the various models presented in Figure 16 we note that TIP has a faster crust and a slower lid than the other models. Thus, the S_n and P_n arrival time prediction for TIP are distinctly slower than others. Comparing with the data at HKC (35.7°), the branches C and E of the TIP synthetics are about two seconds faster than the data, this means that either the shear velocity of the upper part, especially the crust, is faster than the observed or the crustal thickness at the bounce point is greater than the model TIP, as discussed earlier. The C branch, and the E branch of the synthetics of Lyon-Caen's models (Ltib) are 7.5, and 4.5 seconds slower than that of the HKC data. The synthetics for Wang's model are also slower than the HKC data by a few seconds. The branches arrive at almost the same time for the ANP (44.8°) data. The synthetics of Wang and Ltib are slower. The F, D and B branches of Ltib are 3.5, 5 and 16 seconds slower than those of SEO data respectively. The B branch of Wang is 11 seconds slower than that of SEO data. Lyon-Caen's Indian model presents a comparison of Indian Shield with the Tibetan Plateau. The slow B branch of Ltib and Wang suggest that the velocities of the upper 200 km of the models are too slow.

Records at this range are particularly important in fixing the shallow mantle velocity. A few additional SRO records were found sampling this range as displayed in Figure 18. The waveform fits are not good, probably
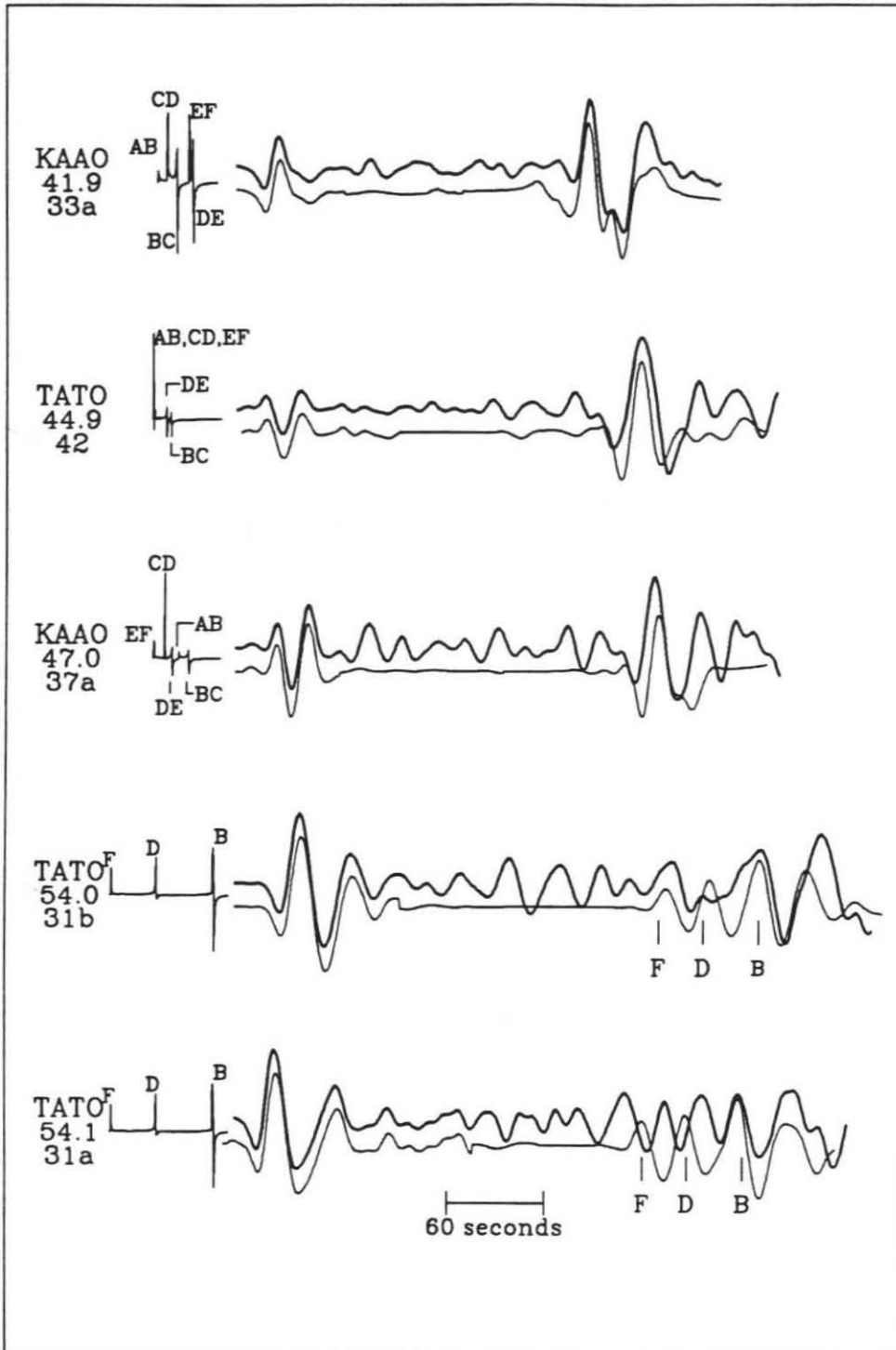
Figure 18. Comparison of the data recorded by SRO stations (upper traces) and synthetics (lower traces) from model TIP. On the left are the stations, distances, and event numbers. On the right of the stations are the Earth responses, on which the branch names indicated.

indicating the heterogeneity of the region, but the timing on the B branch relative to the other triplications is indicative of shield structure. This suggests that the upper mantle in this region is, indeed, fast.

To check our results further requires some absolute travel time constraints or better knowledge about the earthquake sources used in terms of location and mechanism. For instance, we used the ISC location and origin time for event 22 in timing NDI, see Figure 6, and found a residual of +10 seconds. This means that the model TIP is 1.5 % faster than the average velocity along this path, but if we used the USGS location and origin time for this event, the travel time residual would be +2 seconds, which means this model is very good. We have no particular reason to say the ISC location and origin time are better. We choose to use them simply for bookkeeping. Since these locations given by the agencies do not use depth phases in their analysis we decided to do an indepth study of one of these events to assess uncertainties and establish a few absolute travel time constraints. Event 36 was selected for this purpose since it also has a few P_{nl} waves on scale. The origin time and location used are 3:2:47.2, 30.506° N, 88.583° E, and an epicentral depth of 33 km assigned by NEIS. This event is big enough to be recorded worldwide, $m_b = 5.7, M_s = 6.2$.

First, we derive the source depth by modeling the teleseismic P waveforms. The results are given in Figure 19 where the best fitting source depth is 10 km. We estimate the errors in depth to be less than 3 km, and fault plane less than 5°. Figure 19 displays the best overall fit of different runs, indicating a strike of 160°, a dip of 60°, and a rake of 250° . Stations

30.00 sec
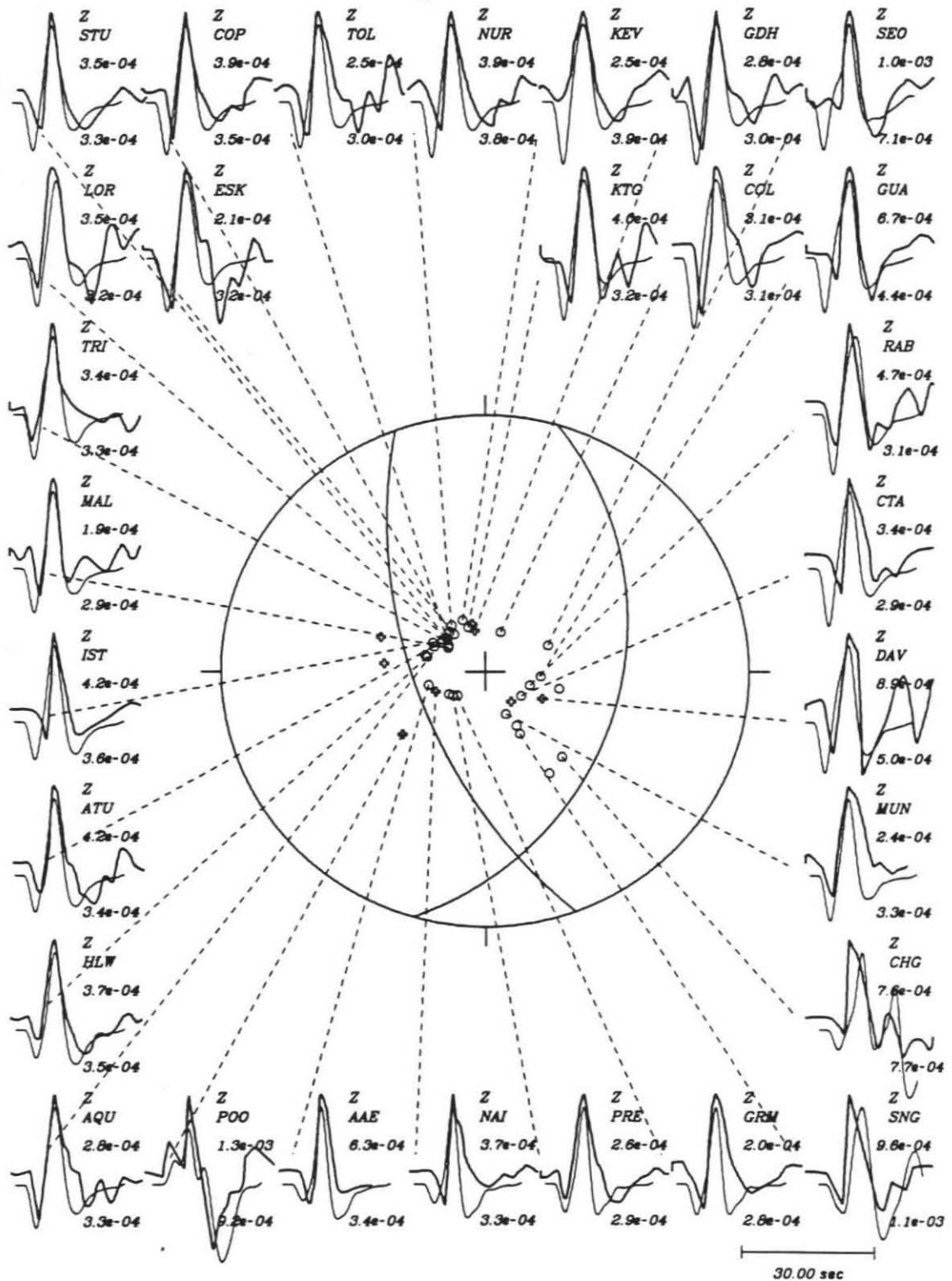
Figure 19. Source mechanisms, and synthetic comparison with the long-period P wave WWSSN data of February 22, 1980 Tibetan earthquake. The origin time is 3:2:43.7, epicenter locates at $30.658°$ N $88.649°$ E, source depth is 10 km. The strike, dip and rake are $160°$, $60°$ and $250°$ respectively. The moment is $8.0 \times 10^{24} dyn \cdot cm$ and the source function is a trapezoid (1, 1, 1). The darker traces are the data, and the lighter ones are synthetics. On the left of each data-synthetic comparison, are the component of the data used ("Z", vertical component), station name, the peak amplitude of the data , and the peak amplitude of the synthetics in centimeters using the moment shown in the head line. The (+) symbol indicates the compressional, and little circles indicate dilational. If the polarity of the short-period data is different from that of its corresponding long-period data, we use that of the short-period.

POO and CHG are within upper mantle distances and the P waveforms recorded by them are complicated by triplications, and matched well by the synthetics. The model used in these calculation was derived by comparing TIP with a P-wave model for the Canadian Shield, namely S25 (LeFevre and Helmberger, 1989) and SNA (Grand and Helmberger, 1984a), and using the relationship with shear velocities of rocks of basaltic composition (Ludwig et al. 1970), (Table 3). Some bad-looking seismograms are due to digitizing since the line-thickness of the recordings is 3-5 seconds thick, and the maximum amplitudes of some recordings do not exceed half of the line-thickness, such as MUN.

The results of the relocation, based on the new source depth, are given in Table 4. In this table, STAT are station names; TPK are the times we picked from vertical component of short-period WWSSN data after minute mark in second; TPKP are the times picked by station operator; TOBS1 and TOBS2 are the observed P wave travel times after the old and new origin time; TCOM1 and TCOM2 are the computed P wave travel times for the old epicenter and origin time, and for the new epicenter and origin time. DT1 and DT2 are the residual travel times after Dziewonski and Anderson (1983) station correction, minus sign means TCOM is faster than TOBS. The standard deviation is 1.5 seconds. This error mainly comes from the contributions of the three stations UME, HLW and STU, whose deviations are greater than 4 seconds. After relocation: the location becomes 30.658° N, 88.649° E, and the origin time becomes 03:02:43.7. The new location is 18 km from the location given by NEIS. The origin time is 3.5

Table 3 Compressional Velocities of TIP

Depth (km)	Thick (km)	Vel (km/sec)	Depth (km)	Thick (km)	Vel (km/sec)
0.00	0.00	4.530	280.0	10.0	8.470
3.75	3.75	4.530	290.0	10.0	8.480
20.0	16.25	6.160	300.0	10.0	8.486
40.0	20.0	6.550	310.0	10.0	8.510
70.0	30.0	6.740	320.0	10.0	8.540
130.0	60.0	8.290	330.0	10.0	8.560
170.0	20.0	8.200	340.0	10.0	8.570
180.0	10.0	8.270	350.0	10.0	8.594
190.0	10.0	8.340	360.0	10.0	8.623
200.0	10.0	8.400	370.0	10.0	8.653
210.0	10.0	8.420	380.0	10.0	8.691
220.0	10.0	8.430	390.0	10.0	8.730
230.0	10.0	8.440	400.0	10.0	8.770
240.0	10.0	8.450	405.0	5.0	8.810
260.0	20.0	8.460			9.280
270.0	10.0	8.462			

Table 4. Relocation of February 22, 1980 Tibet earthquake. The location 30.506° N, 88.583° E, and the origin time 03:02:47.2; After relocation: the location 30.658° N, 88.649° E, and the origin time 03:02:43.7.

STAT	TPK	TPKP	TOBS1	TOBS2	TCOM1	TCOM2	DT1	DT2
AAE	51.3	50.0	544.1	547.6	544.8	545.5	-3.1	-0.3
ADE	57.8	59.3	730.6	734.1	733.4	733.8	-2.9	0.2
AQU	51.3	51.3	604.1	607.6	607.9	607.7	-4.7	-1.0
BAG	17.4	16.1	390.2	393.7	392.3	392.2	-2.7	0.9
BUL	36.1	36.0	708.9	712.4	712.3	713.0	-2.8	-0.0
CHG	14.8	14.9	207.6	211.1	212.3	213.4	-4.0	-1.5
COL	27.9	28.3	700.7	704.2	705.5	704.6	-5.1	-0.6
COP	37.1	37.8	589.9	593.4	594.1	593.5	-5.1	-1.0
CTA	26.1	26.0	698.8	702.3	702.7	702.9	-3.9	-0.6
DAV	36.4	34	469.2	472.7	471.3	471.5	-3.5	-0.1
ESK	34.7	34.8	647.5	651.0	652.1	651.5	-4.9	-0.9
GDH	36.6	36.3	709.4	712.9	713.5	712.7	-4.0	0.3
GRM	28.6		761.4	764.9	764.0	764.7	-3.5	-0.6
HKC	2.8	5	315.6	319.1	319.0	318.8	-4.9	-1.2
HLW	37.9	34	530.7	534.2	529.3	529.4	1.5	4.8
IST	29.4	25	522.2	525.7	526.4	526.2	-4.7	-1.0
JER	6.2		499.0	502.5	500.3	500.4	-2.2	1.3
KBL	40.8	41.1	233.6	237.1	237.9	238.0	-4.2	-0.7
KEV	54.9	55.0	547.7	551.2	551.4	551.2	-4.0	0.4
KTG	46.8	46.2	659.6	663.1	662.0	663.1	-3.6	0.7
LOR	24.3	25.1	637.1	640.6	642.3	640.6	-4.7	-0.8
MAT	32.0	31.3	464.8	468.3	468.8	467.9	-3.6	0.9
MUN	41.9	40	654.7	658.2	658.0	658.7	-2.5	0.3
NAI	43.9	44	596.7	600.2	599.0	599.8	-3.4	-0.6
NDI	11.6	11.5	144.4	147.9	146.6	147.6	-1.4	1.0
NIL	55.2		188.0	191.5	190.9	191.0	-2.8	0.5
NUR	48.8	49.5	541.6	545.1	546.0	545.3	-4.4	-0.2
POO	54.7	54.3	247.5	251.0	250.0	251.8	-2.2	-0.4
PMG	50.5	50	663.3	666.8	666.4	666.5	-3.3	0.1
QUE	2.8		255.6	259.1	259.5	260.1	-3.7	-0.8
RAB	57.4	57.5	670.2	673.7	672.3	672.3	-2.6	0.9
SHL	12.3	12	85.1	88.6	87.6	88.9	-1.3	0.8
SNG	17.6	19	330.4	333.9	333.1	334.1	-2.9	-0.4
STU	3.5	2.0	616.3	619.8	616.5	616.1	0.2	4.2
TOL	16.3	15.0	689.1	692.6	692.0	691.8	-3.5	0.3
TRI	43.0	42.9	595.8	599.3	600.9	600.5	-4.5	-0.7
UME	2.2	6.5	555.0	558.5	564.2	563.4	-8.9	-4.6

seconds earlier than that given by NEIS, 1.3 seconds earlier than that given by ISC. We used the modified P-wave TIP model as discussed before for the source region and JB for the receivers to calculate the TCOM. For a distance greater than 30°, the half way travel time difference between the model TIP and the model JB is only 0.5 seconds. If we used JB model for the source region, the new location would be 30.625° N , 88.632° E, only 4 km from the location given by different source velocity models, the origin time would be 03:02:43.7, only 0.04 seconds difference. This is because the upper 400 km of JB model is slow, or the average velocity of upper 400 km of JB is about same as that of the model TIP.

As a check on the accuracy of our crustal model, we make synthetics of P_{nl} waveforms and compare with the data recorded at the stations NDI and NIL due to the Tibetan earthquake we relocated above. Figure 20 displays the P_{nl} data along with the synthetics of the model TIP. The method used to make these synthetics is reflectivity (Mallick and Frazer, 1988). The synthetics of NDI is shifted left 1.5 seconds, that of NIL is shifted left 0.5 seconds. We present only three seismograms here since the amplitudes of the north components of both stations are very small and the vertical component of NIL station was not available. We can see from Figure 20 that the fits are good. This means that the average velocity structure and the crustal thickness of the Tibetan Plateau can be approximated by the model TIP for the paths (Figure 6), although these paths only sample the southern part of the Plateau. The time shifts given above are largely caused by the dipping Moho. Thinning the crust at the receiver by 20 km
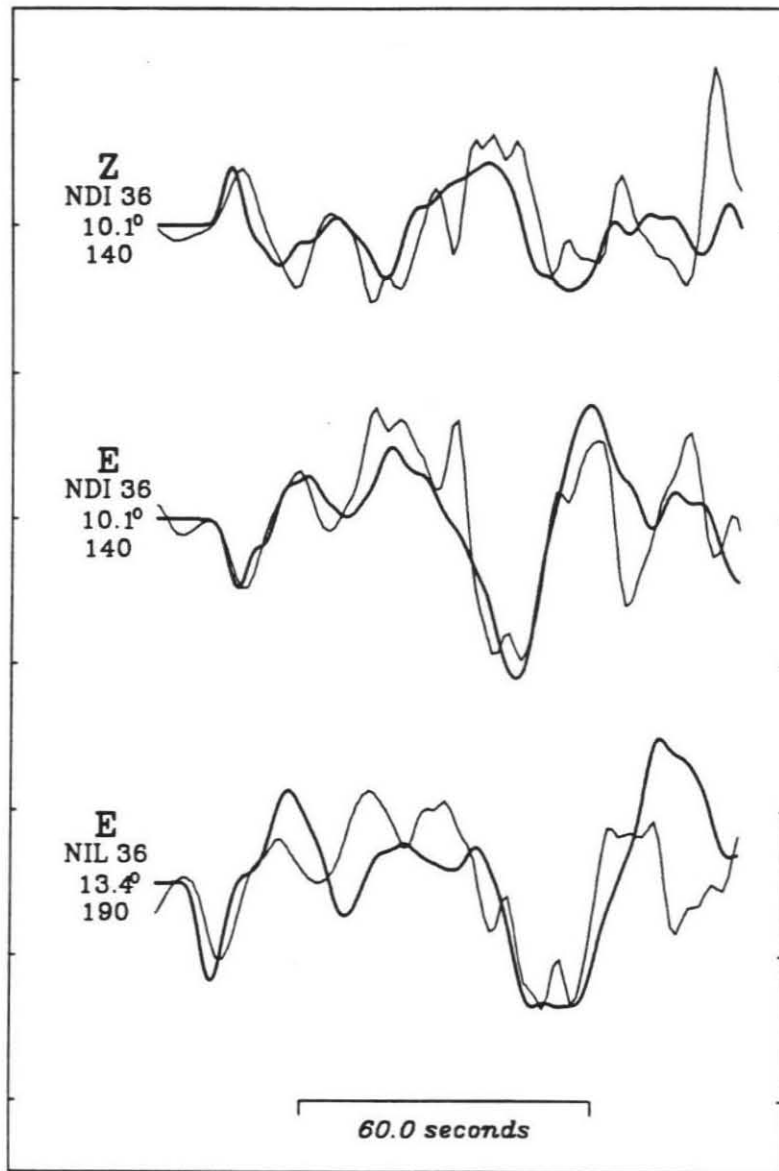
Figure 20. Synthetic comparison with P_{nl} waveform data. The darker traces are the data, and the lighter ones are the synthetics. The beginning time of the corresponding data and synthetics are 140 and 190 seconds. The data and synthetics are lined up with absolute time, with NDI synthetics shift left 1.5 seconds, NIL synthetics shift left 0.5 seconds. The numbers beside the station names are event numbers given in Table 1.

reduces the P_n travel time by 2.2 seconds, see Figure 6. Thus, considering the possible crustal thickness beneath the stations, and assuming that the crustal thickness beneath NDI and NIL is 50 km, we conclude that the model TIP is about 0.7 seconds faster for the path to NDI, 1.7 seconds faster for that to NIL. This implies that the P wave velocity of the mantle for these paths is 8.23 km/sec instead of the 8.29 km/sec that we used in the above flat layered P_{nl} calculation.

Barazangi and Ni (1982), and Ni and Barazangi (1983) used P_n- and S_n- waves crossing the Tibetan Plateau, and obtained velocities of 8.42 km/sec for P_n, and 4.73 km/sec for S_n. They concluded that these velocities were very similar to those beneath the Himalaya Mountains and the Indian shield, and suggested that the Indian continental lithosphere underthrusts the Tibetan Plateau at a shallow angle. However, our earlier experiments suggest a high velocity bias for most recording geometries if one simply assumes a flat-layered model. For instance, in Figure 4, the S_n arrives about 3.5 seconds earlier in the model d than a flat structure with a crustal thickness 70 km, model f. A mantle velocity would be 4.69 km/sec, instead of 4.6 km/sec used in Figure 4. Thus, an average S_n velocity of 0.1 km/sec greater than the average velocity beneath the Tibetan Plateau is very likely obtained if the only S_n data are used. Seismograms for two-dimensional models crossing this interesting region will be discussed in a later paper.

Our results (TIP) are consistent with that of the attenuation study of pure path long-period Rayleigh waves across the Tibetan Plateau by Romanowicz (1984). The conclusion of "no lid" for the Tibetan Plateau is

consistent with that for the central Chang-Thang of Tibet from pure path phase velocity measurement of long period Rayleigh waves by Brandon and Romanowicz (1986). These results are similar to those obtained from modeling multi-bounce S-waves by Grand and Helmberger (1985), who constructed a 2D cross-section from Tibet to Europe. Resolution from their study begins at the edge of Tibet and indicates that the structure beneath the Tarim basin is similar to our results for Tibet, namely, a shield-like model with a slow upper 200 km. We do not presently have a detailed shear velocity model available for the eastern part of China, except that it appears similar to other shields. Thus, from this study, and the studies by Grand and Helmberger (1985), and Rial, Grand and Helmberger (1984) we suggest that the upper mantle of the Eurasian plate is shield-like below 200 km.

Although these results are preliminary in nature it would appear that the deformations of the European plate is confined mainly to the upper 200 km. This type of velocity distribution thus becomes an important piece of evidence to be used in deducing the tectonics of the area.

It is generally assumed that major undertrusting is occurring along the Himalayan arc as deduced from source mechanism studies, see Ni and Barazangi (1984) and others. The dynamic processes that lead to the formation and maintenance of a mean elevation of 5 kms over some 2 million square kms behind the Himalayan arc appears more controversial. Essentially two hypothesis have been put forward, namely underthrusting and crustal shortening. Underthrusting in the Pacific Northwest results in complex crustal structures with a large low velocity zone associated with the subducted

upper crustal section, see Langston (1977). We did not find much evidence for such structures in this study. Crustal shortening has been suggested by Molnar and his associates. They argue that the temperature at the base of the crust is 250 to 300° higher than beneath platforms, see Chen and Molnar (1981). Increased radiogenic material per horizontal area is thought to contribute to this heating. If we compare the mantle shear velocity at the top of our model with those of pure shield models we obtain a reduction of 0.1 - 0.2 km/sec, essentially 4.7 - 4.8 to 4.6 km/sec. The temperature difference for this velocity difference is 300–600°, assuming that the upper mantle is composed of olivine (40 %), clinopyroxene and garnet as suggested by Duffy and Anderson (1989). We have $(d\beta/dT)_p = -3.3 \times 10^{-4}$ $km/(sec \cdot °C)$ for upper mantle materials at $1000°K$ (Duffy, personal communication; Suzuki et al. 1983). This temperature estimation are somewhat higher than the above estimates, see Molnar (1989), reflecting the contrast in velocity models, see Figure 16, where the Lyon-Caen's model has a higher lid velocity than TIP. Our results suggest that the crustal structure is playing a particularly important role in controlling the tectonics of the Tibetan Plateau and in surrounding regions. Thus the higher resolution of this complex structure is essential and will be possible when the new digital observations from the Soviet Union and China become available.

In conclusion, we have examined some of the special problems associated with determining the upper-mantle structure beneath Tibet. The principal difficulty is caused by the absence of stations located on the thickened plateau structure. This situation is compounded by inaccuracies in source lo-

cations and origin times for events in the region. We have attempted to quantify these effects by locating some master events, modeling teleseismic waveforms in shape and in timing, and by developing timing corrections based on 2D numerical experiments. Our results indicate that P_n and S_n velocities from previous studies are probably 2–3% too high based on geometrical corrections for laterally varying crustal structure. The most meaningful data in determining the structure directly beneath Tibet is from the $SS-S$ data. Near fifty degrees three distinct branches of SS appears, the slowest is bottoming the shallowest and it is the timing of this particular phase that is the most diagnostic. Our results suggest that the separation of branches and relative timing is similar to that found in other shields and that the structure is shield-like below 200 km. However, the waveform consistency is poor, suggesting considerable crustal complexity. These features will be explored in future efforts.

ACKNOWLEDGEMENTS

fornia, 91125.

REFERENCES

Baranowski, H., H. Armbruster, L. Seeber and P. Molnar, 1984. Focal depths and fault plane solutions of earthquakes and active tectonics of the Himalaya, *J. Geophys. Res.*, **89**, 6919-6928.

Barazangi, M., and J. Ni, 1982. Velocities and propagation characteristics of *Pn* and *Sn* beneath the Himalayan arc and Tibetan Plateau: possible evidence for underthrusting of Indian continental lithosphere beneath Tibet, *Geology*,**10**, 179-185.

Brandon C. and B. Romanowicz, 1986. A " no - lid " zone in the central Chang - Thang platform of Tibet: Evidence from pure path phase velocity measurements of long period Rayleigh waves, *J. Geophys. Res.*, **B6**, 6547-6564.

Chapman, C. H., 1978. A new method for computing synthetic seismograms, *Geophys. J. R. astr. Soc.*, **57**, 649-670.

Chen, Wang-Ping, and P. Molnar, 1981. Constraints on the seismic wave velocity structure beneath the Tibetan Plateau and their tectonic implications, *J. Geophys. Res.*, **86**, 5937-5962.

Chun Kin-yip and T. V. McEvilly, 1985. New seismological evidences of Tibetan lithosphere structure, *Acta Geophysica Sinica*, **28**, Supp. I., 135-147 (in Chinese, English Abstract).

Duffy, T. S., and D. L. Anderson, 1989. Seismic velocities in mantle minerals and the mineralogy of the upper mantle, *J. Geophys. Res.*, **94**, 1895-1912.

Dziewonski, A. M, and D. L. Anderson, 1983. Travel times and station corrections for P waves at teleseismic distances, *J. Geophys. Res.*, **88**, 3295-3314.

Feng, C., 1982. A surface wave study of crustal and upper mantle structures of Eurasia, *Ph.D thesis*, University of Southern California.

Grand, S. P., and D. V. Helmberger, 1984a. Upper mantle shear structure of North America, *Geophys. J. R. astr. Soc.*, **76**, 399-438.

Grand, S. P., and D. V. Helmberger, 1984b. Upper mantle shear structure beneath the northwest Atlantic Ocean, *J. Geophys. Res.*, **89**, 11465-11475.

Grand, S. P., and D. V. Helmberger, 1985. Uppermantle shear structure beneath Asia from multi-bounce *S* waves, *Phys. Earth Planet. Inter.*, **41**, 154-169.

Harkrider, D. G., 1964. Surface waves in multilayered elastic media, I. Rayleigh and Love waves from buried sources in a multilayered elastic half-space, *Bull. Seism. Soc. Am.*, **54**, 627-679.

Harkrider, D. G., 1970. Surface waves in multilayered elastic media, II. Higher mode spectra and spectral ratios from point sources in plane layered Earth models, *Bull. Seism. Soc. Am.*, **54**, 1937-1987.

Helmberger, D. V. and J. E. Vidale, 1988. Modeling strong motions produced by earthquakes with two-dimensional numerical codes, *Bull. Seism. Soc. Am.*, **78**, 109-121.

Hirn, A., J.-C. Lepine, G. Jobert, M. Sapin, G. Wittlinger, Z. X. Xu, E. Y. Gao , X. J. Wang, J. W. Teng, S. B. Xiong, M. R. Pandey, and J. M.

Tater, 1984. Crustal structure and variablity of the Himalayan border of Tibet, *Nature*, **307**, 23-25.

Holt, W. E. and T. C. Wallace, 1989. Crustal thickness and upper mantle velocities in the Tibetan Plateau region from the inversion of regional P_{nl} waveforms: Evidence for a thick upper mantle lid beneath southern Tibet, submitted to *J. Geophys. Res.*

Langston, C. A., 1977. Corvallis, Oregon, crustal and upper mantle receiver structure from teleseismic P and S waves, *Bull. Seis. Soc. Am.*, **67**, 713-724.

Langston, C. A., and D. V. Helmberger, 1975. A procedure for modeling shallow dislocation sources, *Geophys. J. R. astr. Soc.*, **42**, 117-130.

LeFevre, L. V. and D. V. Helmberger, 1989. Upper mantle P velocity of the Canadian Shield, *J. Geophys. Res.*, **B12**, 17749-17765.

Ludwig, W. J., J. E. Nafe, and C. L. Drake, 1970, Seismic refraction, in *The Sea*, edited by A. E. Maxwell, Vol. 4, Part I, 53-84, Wiley-Interscience.

Lyon-Caen, H., 1986. Comparison of the upper mantle shear wave velocity structure of the Indian Shield and the Tibetan Plateau and tectonic implications,

   Geophys. J. R. astr. Soc. , **86**, 727-749.

Mallick, S. and L. N. Frazer, 1988. Rapid computation of multioffset vertical seismic profile synthetic seismograms for layered media, *Geophysics*, **55**, 479-491.

Minster, J. F., T. J. Jordan, P. Molnar and E. Haines, 1974. Numerical modeling of instantaneous plate tectonics, *Geophys. J. R. astr. Soc.* ,

36, 541-576.

Molnar, P. and W.-P. Chen, 1983. Focal depths and fault plane solutions of earthquakes under the Tibetan Plateau, *J. Geophys. Res.*, **88**, 1180-1196.

Molnar, P., 1989. The geology evolution of the Tibetan Plateau, *American Scientist*, **77**, 350-360.

Ni, J., and M. Barazangi, 1983. High frequency seismic wave propagation beneath the Indian Shield, Himalayan arc, Tibetan Plateau and surrounding regions: High uppermost mantle velocities and efficient *Sn* propagation beneath Tibet, *Geophys. J. R. astr. Soc.*, **72**, 665-681.

Ni, J., and M. Barazangi, 1984. Seismotectonics of the Himalayan collision zone: geometry of the underthrusting Indian plate beneath the Himalaya, *J. Geophys. Res.*, **89**, 1147-1163.

Rial, J. A., S. Grand, and D. V. Helmberger, 1984. A note on lateral variation in upper mantle shear-wave velocity across the Alpine front, *Geophys. J. R. astr. Soc.*, **77**, 639-654.

Romanowicz, B. A., 1982. Constraints on the structure of the Tibet Plateau from pure path phase velocities of Love and Rayleigh waves, *J. Geophys. Res.*, **87**, 6865-6883.

Romanowicz, B. A., 1984. Pure path attenuation measurements of long-period Rayleigh waves across the Tibet Plateau, *Phys. Earth Planet. Inter.*, **36**, 116-123.

Shedlock, K. M., and S. W. Roecker, 1987. Elastic wave velocity structure of the crust and upper mantle beneath the North China basin, *J. Geophys.*

Res.,**92**, 9327-9350.

Singh, D. D., 1977. Crust and upper mantle velocity structure beneath north and central India from the phase and group velocity of Rayleigh and Love waves, *Tectonophysics*, **139**, 187-203.

Suzuki, I., O. L. Anderson, and Y. Sumino, 1983, Elastic properties of a single-crystal forsterite Mg_2SiO_4, up to 1200 K, *Phys. Chem. Min.*, **10**, 38-46.

Tapponnier, P., and P. Molnar, 1977. Active faulting and tectonics of China, *J. Geophys. Res.*, **82**, 2905-2930.

Teng, Ji-Wen, 1987. Explosion study of the structure and seismic velocity distribution of the crust and upper mantle under the Xizang (Tibet) Plateau, *Geophys. J. R. astr. Soc.*, **89**, 405-414.

Wang, Kai, and Zhen-Xing Yao, 1989. Preliminary study of upper mantle shear velocity structure of China, *Chinese J. of Geophysics*, **32**, 49-60. (English edition published by Allerton Press Inc. New York).

Wang, Shu - Yun, and Zhong - Huai Xu, 1985. Seismic tectonic stress fields of eastern continental China, *Acta Seismological Sinica*, **7**, 17-31 (*in Chinese, Figure Captions in English*).

Wier, Stuart, 1982. Surface wave dispersion and earth structure in southeastern China, *Geophys. J. R. astr. Soc.*, **69**, 33-47.

Yang, Zunyi, Yuqi Cheng, and Hongzhen Wang, 1986. *The Geology of China, Oxford Monographs on Geology and Geophysics*, **3**, Clarendon Press, Oxford.

Zhang, Zh. M., J. G. Liou, and R. G. Coleman, 1984. An outline of the

plate tectonics of China, *Geol. Soc. Am. Bull.*, **5**, 295-312.

CHAPTER 4

A Note on the Relocation of Tibetan Earthquakes

ABSTRACT

Present ISC locations for earthquakes beneath Tibet indicate a random distribution of events down to a depth of about 50 km. This distribution might be expected from a relatively cool crust which would allow the seismo-genic zone to extend to such depths. A detailed investigation of 100 such events yields a distinctly different picture. Waveform modeling of depth phases such as pP indicates that only three or four events from this population is actually deeper than 25 km. These few events occur near the edges of the Plateau where active subduction is occurring as suggested by the thrust-like nature of their mechanisms. The events, averaging the entire population, occurred earlier than indicated by the ISC by about 3 seconds which leads to about a 1.5% and 0.5% over estimation of P_n and S_n velocities respectively applying ISC tables and standard flat-layered models. A more serious error occurs if the P_n and S_n velocities are determined by correcting for source depth but assuming the ISC origin times.

DATA, ANALYSIS AND RESULTS

The events studied are listed in Table 1. Included in this table are the ISC determinations of depth, location and origin times of these events along with new estimates obtained from this investigation. The main objective of this report is to document these results and discuss their significance.

The data comes from the WWSSN chip library of the Seimological Laboratory at California Institute of Technology and consists mostly of long period P-waveforms and travel time picks read from the short period vertical components. The P-waveform data is used to constrain depths while the time picks are used to relocate and determine the origin times.

Errors in depth determinations using travel times become serious when no local stations are available, that is the case in Tibet. Essentially, there is a complete trade-off between origin time and depth. This difficulty can be circumvented by determining the depths independently by applying waveform modeling of the P-waveforms (Langston and Helmberger 1975). This technique models the interference between direct P and free surface reflections to fix the epicentral depth although it is dependent on the velocity model of the source region. For example, assuming a surface layer of velocity 5 km/sec instead of 5.5 km/sec introduces a -1.0 km depth error, if the travel time difference between P and pP is used in modeling an event at a depth of 10 km. Thus, the source depth as determined by P waveform modeling is not very sensitive to crustal velocity and can be used to estimate the depths of the above events.

Many of the P-waveforms from Tibetan events have been modeled previously by a number of authors as indicated in the Table. These solutions

Table 1. Relocation of Tibetan Earthquakes

Date			Origin Time			ΔT	Location (°N, °E)				D	Depth		Mb	N	Data
Mo	Da	Yr	h m	relc	ISC	(sec)	relc		ISC		(km)	relc	ISC			
03	16	64	0105	13.5±1.2	19.8	-6.3	37.11	95.60	36.95	95.50	20.1	10	50	5.9	21	in
09	26	64	0046	-3.1±1.3	02.6	-5.7	29.91	80.55	29.96	80.46	10.6	18	50	5.8	32	abin
10	21	64	2309	15.8±1.3	19.0	-3.2	28.22	93.87	28.04	93.75	10.6	15	37	5.9	32	adhn
01	12	65	1332	22.1±1.1	24.1	-2.0	27.41	87.85	27.40	87.84	1.8	15	23	5.8	27	anf
02	05	66	1512	27.2±1.0	32.9	-5.7	26.29	103.20	26.22	103.21	8.3	4	42	5.6	39	en
02	13	66	1044	36.0±1.2	38.0	-2.0	26.27	103.25	26.17	103.25	10.6	4	6	5.4	32	en
03	06	66	0210	52.1±0.8	52.0	+0.1	31.50	80.53	31.51	80.55	2.2	11	5	5.3	33	n
03	06	66	0215	49.8±1.1	57.2	-7.4	31.48	80.50	31.49	80.50	10.0	8	50	6.0	37	gn
06	27	66	1041	04.2±1.2	08.1	-3.9	29.70	80.89	29.62	80.83	10.4	15	33	6.0	42	abhn
08	15	66	0215	29.9±1.1	28.0	+1.9	28.70	78.91	28.67	78.93	4.5	25	5	5.6	31	fn
09	26	66	0510	54.5±1.1	56.2	-1.7	27.53	92.73	27.49	92.61	12.9	17	20	5.4	34	bn
09	28	66	1400	18.5±1.3	21.0	-2.5	27.55	100.10	27.53	100.08	2.5	10	12	5.7	42	en
10	14	66	0104	40.0±1.2	42.9	-2.9	36.50	87.46	36.45	87.43	6.3	8	14	5.2	32	ghn
12	16	66	2052	14.1±1.5	16.3	-2.2	29.66	80.84	29.62	80.79	6.1	12	19	5.7	40	ahfn
03	14	67	0658	02.8±1.5	04.4	-1.6	28.57	94.37	28.41	94.29	19.0	15	20	5.8	36	adhn
08	15	67	0921	-2.6±0.9	03.3	-5.9	31.23	93.56	31.05	93.56	17.0	8	36	5.5	25	en
08	30	67	0422	01.8±1.2	05.1	-3.2	31.71	100.24	31.61	100.26	11.7	10	24	6.1	35	emn
08	30	67	1108	44.8±1.4	51.0	-6.2	31.73	100.28	31.57	100.31	18.1	8	35	5.2	28	emn
02	19	70	0710	00.2±1.4	01.5	-1.3	27.47	94.02	27.40	93.96	9.7	10	12	5.4	19	hfn
02	24	70	0207	31.5±1.4	36.0	-4.5	30.66	103.02	30.61	103.05	6.2	7	24	5.8	27	in
03	24	71	1354	15.2±1.2	18.4	-3.2	35.46	98.03	35.46	98.04	0.9	7	13	5.7	40	in
04	03	71	0449	-2.2±1.4	03.1	-5.3	32.19	95.08	32.16	94.99	8.9	8	27	5.6	40	n
04	03	71	0450	39.8±1.4	45.8	-5.6	32.10	95.10	32.10	95.19	8.9	8	33	5.3	25	en
05	22	71	2003	27.3±1.3	31.9	-4.6	32.42	92.11	32.36	92.11	6.7	8	29	5.5	43	egn
08	30	72	1514	05.0±1.3	07.5	-2.5	36.64	96.35	36.65	96.35	1.3	15	17	5.5	31	in
08	30	72	1847	38.6±1.2	40.3	-1.7	36.71	96.46	36.56	96.35	18.9	19	16	5.5	30	in
09	03	72	1648	24.4±0.9	29.5	-5.1	36.06	73.31	35.94	73.33	13.6	12	45	6.2	37	aehn
02	06	73	1037	06.1±1.5	07.0	-0.9	31.38	100.54	31.33	100.49	6.7	10	5	5.9	37	mn
02	07	73	1606	20.7±1.3	25.8	-5.1	31.58	100.28	31.50	100.33	10.2	8	35	5.9	35	en
07	14	73	0451	16.1±1.5	20.0	-3.9	35.25	86.41	35.16	86.40	10.0	6	22	5.9	48	eghn
07	14	73	1339	24.1±0.7	29.4	-5.3	35.30	86.51	35.21	86.54	10.7	7	29	5.7	18	egn
01	15	75	1134	37.0±1.2	41.0	-4.0	29.46	101.78	29.41	101.78	5.3	10	29	5.5	41	en
01	19	75	0801	57.6±1.4	58.0	-0.4	32.39	78.58	32.39	78.50	7.5	9	1	6.2	36	ghn
08	16	76	1406	44.5±1.4	45.0	-0.5	32.80	104.09	32.78	104.09	3.8	12	9	6.1	35	kn
08	21	76	2149	49.1±1.1	52.0	-2.9	32.58	104.29	32.59	104.29	1.2	5	15	6.0	17	kn
08	23	76	0330	02.9±1.2	06.0	-3.1	32.55	104.24	32.49	104.18	8.8	8	17	6.2	20	kn
11	18	77	0520	06.7±1.1	10.3	-3.4	32.75	88.44	32.65	88.39	12.4	10	24	5.7	22	ehin
03	29	79	0707	15.3±1.3	22.0	-6.7	32.55	97.28	32.44	97.26	12.9	10	45	5.4	32	ein
02	13	80	2209	32.3±1.2	30.8	+1.5	36.61	76.85	36.47	76.86	15.1	90	74	6.0	36	cn
02	22	80	0302	42.8±0.7	45.2	-2.4	30.65	88.61	30.55	88.60	11.0	10	14	5.7	34	hikln
06	01	80	0619	-5.2±1.1	01.2	-6.3	39.06	95.63	38.91	95.60	16.5	12	50	5.2	26	in
06	24	80	0735	44.7±1.2	44.7	+0.0	33.02	88.46	33.00	88.55	9.2	11	3	5.1	25	in
07	29	80	1458	39.4±1.0	41.6	-2.2	29.64	81.08	29.63	81.09	7.5	15	23	6.1	39	hikn
08	23	80	2136	48.9±1.5	49.0	-0.1	33.07	75.69	32.96	75.75	13.0	14	3	5.2	27	in
08	23	80	2150	-0.5±2.0	01.0	-1.5	32.89	75.83	32.90	75.80	3.2	13	12	5.2	28	in
10	07	80	0932	03.0±1.3	08.7	-5.7	35.63	82.21	35.62	82.14	6.5	4	32	5.4	29	in
11	19	80	1900	45.5±0.9	45.0	+0.5	27.47	88.80	27.40	88.80	7.9	14	1	6.0	45	hkn
01	23	81	2113	46.5±1.2	52.0	-5.5	30.99	101.14	30.89	101.15	11.4	8	34	5.7	22	mn
06	09	81	2208	17.6±1.3	18.6	-1.0	34.65	91.34	34.51	91.42	21.1	10	10	5.3	29	ein
01	23	82	1737	25.8±1.2	29.2	-3.4	31.74	82.27	31.68	82.28	6.6	10	25	6.0	33	hn
06	15	82	2324	26.5±1.2	28.8	-2.3	31.91	99.92	31.85	99.92	7.1	7	10	5.5	34	ein
02	13	83	0140	08.2±1.9	09.2	-0.9	40.05	75.17	39.99	75.24	9.0	5	0	5.6	29	en
05	20	85	1511	35.6±0.5	38.9	-3.3	35.62	87.28	35.56	87.20	9.9	8	19	5.2	13	in
04	26	86	0735	12.6±1.3	16.2	-3.6	32.23	76.39	32.15	76.40	11.8	13	33	5.2	28	in
06	20	86	1712	43.5±1.2	47.2	-3.7	31.23	86.79	31.22	86.82	3.0	15	33	5.9	27	ejin
07	06	86	1924	20.9±1.2	23.1	-2.2	34.55	80.15	34.45	80.20	12.3	5	9	5.7	28	in
07	16	86	2203	07.7±1.6	07.0	+0.7	31.10	78.08	31.05	78.00	8.8	13	4	5.6	25	n
08	20	86	2123	51.2±1.2	53.9	-2.8	34.65	91.49	34.56	91.64	17.1	11	25	5.6	24	in
08	26	86	0943	-1.2±1.4	00.5	-1.7	37.83	101.55	37.74	101.52	10.7	7	8	6.1	29	hn

a Baranowski et al., 1984
b Chandra, 1978
c Fan and Ni, 1989
d Fitch, 1970
e Holt and Wallace, 1990

f Molnar et al., 1973
g Molnar and Chen, 1983
h Molnar and Chen, 1984
i Molnar and Lyon-Caen, 1989
j Nelson et al., 1987

k Ni and Barazangi, 1984
l Zhao et al., 1989
m Zhou et al., 1983
n this study

have been checked by adding station coverage and, in general, found to be satisfactory. New depth estimates from modeling these events assuming the crustal model given in Zhao, Helmberger and Harkrider (1991), model TIP, are listed in Table 1.

We used the P wave travel times for relocations. These usually agreed with the ISC reports except in a few cases. More than 30 travel time picks distributed in azimuth are available for most events, thus providing excellent coverage. The station coverage is indicated in the Table 1. The relocation procedure used is a simple iteration scheme based on the definition of the ray parameter p, namely,

$$p = \frac{dT}{dR} \qquad \text{or} \qquad dR = \frac{dT}{p} \qquad (1)$$

where dT is a small change in travel time associated with a small change in location. We start with the origin time and location given by ISC. We define

$$dT = (T_{obs} - T_0) - T_c \qquad (2)$$

where T_{obs} is the observed time pick, T_0 is the origin time and T_c is the theoretical travel time based on an earth model. We assume TIP in the source region along with elevation correction and the model JB at the receiver stations. Station corrections were applied from the Dziewonski and Anderson's (1983) station correction table. By assuming that the dT's are from a Gaussian distribution, we form the expectation estimate

$$\delta T = \frac{1}{n} \sum_{i=1}^{i=n} dT_i. \qquad (3)$$

and obtain a new origin time $T_{0new} = T_{0old} + \delta T$. From equations (2) and (3), we can see that δT based on this new origin time is zero.

Then we use the new dT assuming T_{0new} given in Equation (2) to determine the mislocation dR from equation (1). We find the estimated mislocations in the North dx and East directions dy, namely,

$$dx = -\frac{1}{n} \sum_{i=0}^{i=n} dR_i \cos\Phi_i \qquad (4)$$

$$dy = -\frac{1}{n} \sum_{i=0}^{i=n} dR_i \sin\Phi_i$$

assuming Gaussian distributions of the two direction mislocations, where Φ_i is the azimuth of the source to the station (i). The new location of the earthquake is given by latitudes θ_{new} and longitude ϕ_{new}:

$$\theta_{new} = \theta_{old} + dx / R_E \qquad (5)$$

$$\phi_{new} = \phi_{old} + dy / (R_E * \cos\theta_{old}).$$

Next we use the new origin time and new location as initial values, we use equations (3) and (5) to calculate the new origin time and location, until some criteria is met. The criteria we used here is that the difference of the standard error $\sigma = (\frac{1}{n} \sum_{i=1}^{i=n} dT^2)^{\frac{1}{2}}$ and the standard error of the last loop is smaller than 0.01 seconds. In this inversion we assume that the source depth is known, but this assumption is not required by the method. The method converges fast, normally under 5 iterations and the final results is not dependent on the initial input. Since changing the origin time trade-offs with T_c, the ISC locations are not effected much by changing the source depths.

After relocation, if the travel time residual of certain station is greater than three seconds, we consult the record again. If there is no problem with the pick, we use it; if the pick is not certain, buried in the noise, we may throw it away depending on the confidence of the pick, and event size, and all other station conditions. We throw away data that have a residual more than 5 seconds, even though the on-set is sharp. For example, UME and SEO produce more than 10 second residuals for some of the large earthquakes, and perhaps were caused by improper clock corrections or reporting errors.

We summerize our results in Table 1. In the table, " relc " means relocation, " D " is the distance between the relocated location and ISC location, " ΔT " is the relocated origin time difference from that of ISC. We also give number of stations used under " N ". Under " Data ", we give the references. The standard error of the origin time due to the inversion are also given in Table 1.

Figure 1 displays the contrast between the ISC depth determinations versus the new estimates. The results are dramatic where all the events occurring beneath the interior of Tibet become shallow events while the events along the frontal thrust zone become deeper. This implies a warm lower crust beneath Tibet similar to other tectonic regions of the world.

The mislocations are not very significant, the greatest is 21.1 km. The origin time corrections are more serious. Of the 59 earthquakes, 54 earthquakes occurred earlier than reported by ISC. The average of all earthquakes is -3.1 seconds, or these earthquakes have occurred 3.1 seconds earlier than reported by ISC. The worst case is -7.4 seconds for the second March 6, 1966 earthquake. Eleven of the events have a residual greater than 5.5
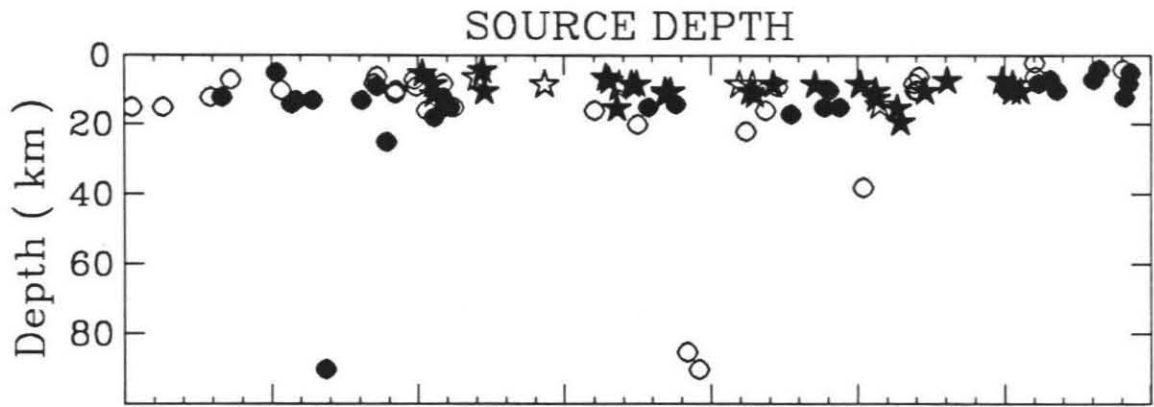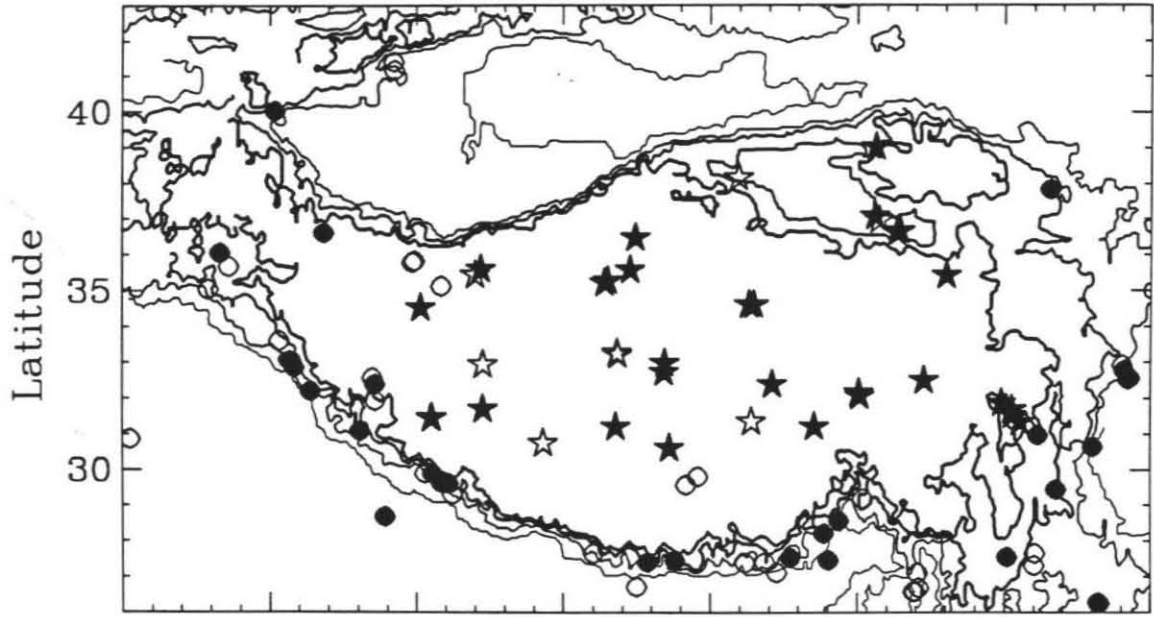
SOURCE DEPTH
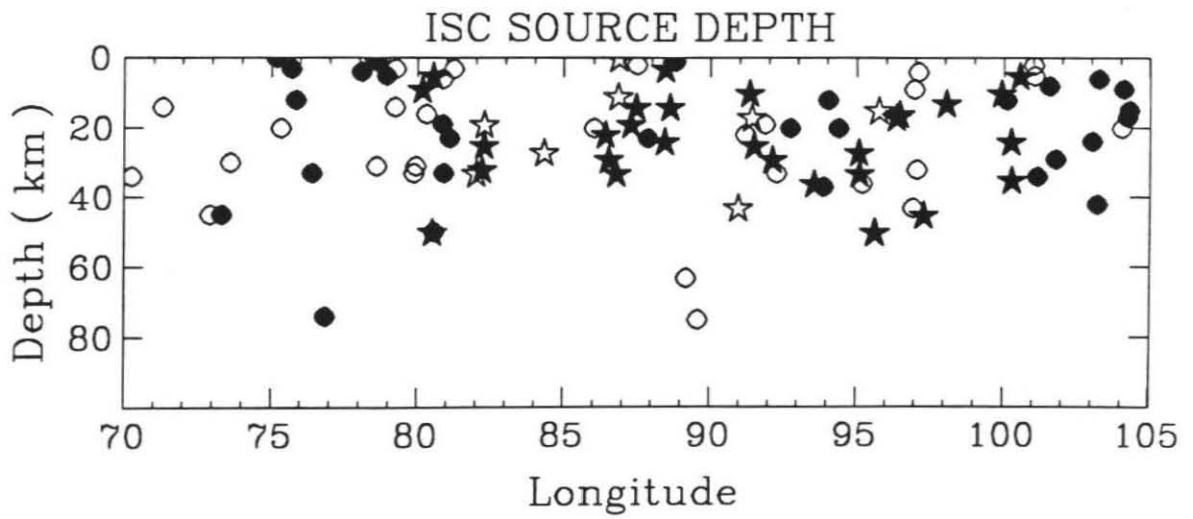
ISC SOURCE DEPTH

Figure 1. The source depths before and after relocation. The top plot shows the locations of the earthquakes whose depths are plotted below. The dots are the earthquakes on the Tibetan boundary, the stars are inside Tibet. The middle plot shows the source depth distribution after relocation and the bottom plot shows ISC depths. The solid symbols indicate the events that we relocated in this study.

seconds.

Figure 2 shows the depth error verses origin time error, with respect to those of ISC. The new points should show a linear trend based on the assumed earth model. The least square fit of the data yields:

$$T = 0.141H - 1.43 \qquad (6)$$

where T, origin time error in seconds, H depth mislocation in km is equal to relocated source depth minus ISC source depth. The standard error is 0.55 seconds if we assume that the origin times do not have errors and the standard error is 0.91 seconds if the error bars are included. The least square fitting method that includes error bars assumes that the probability distribution in the intervals of values between two ends is constant, the non-information probability density. The coefficient of H, 0.141, is dependent on the input model TIP, 6.16 to 6.55 km/sec of source layer, and the average ray parameter.

The offset of -1.43 seconds comes from the differences of earth model, the station correction and topographic correction relative to ISC assumption. For example, suppose we pick an event, August 20, 1986, 21 : 23 : 53.9 (ISC origin time), which falls near the line or on the average level (Figure 2) and examine the various corrections. We relocate it and find a new origin time 21 : 23 : 54.21. In this calculation, we assume the source depth of 25 km given by ISC, and the JB model for both source region and the receiver structures, without correcting for the station delay. The travel time difference resulting from replacing the JB model by TIP is 0.4 seconds assuming a ray parameter of 0.07 sec/km. Station correction contributes about -0.2 seconds to the origin times. The elevation correction of 5 km
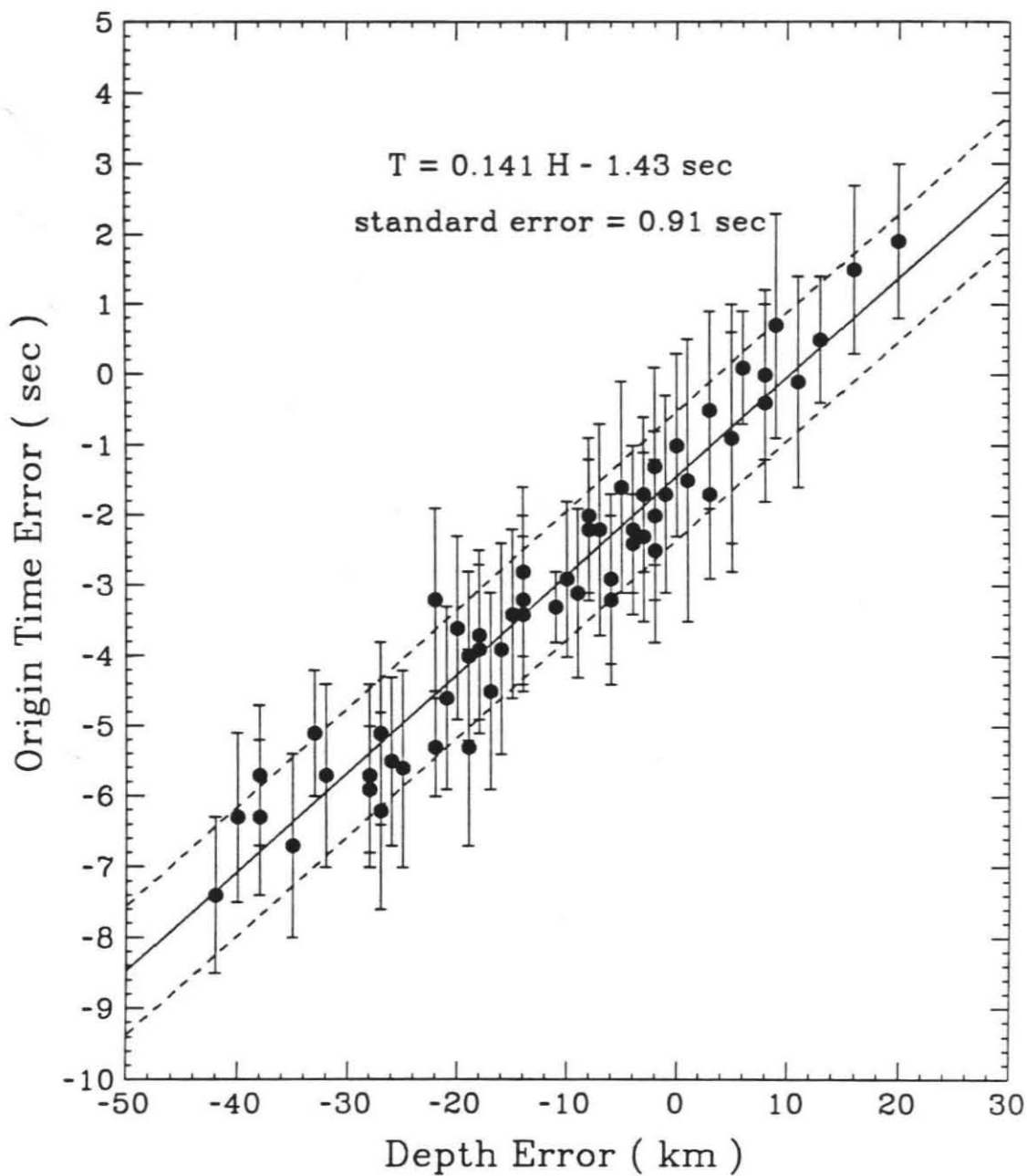
Figure 2. Origin time error verses depth error respects to the ISC reports. The vertical lines show the error bars.

results in 0.8 seconds. The total of all these corrections accounts for the 1.4 second offset.

In Figure 3, we show the origin time errors, and source depth errors versus the body wave magnitude m_b. The data set for bigger earthquakes is certainly larger than that for smaller ones and the expected location and origin times should be better determined. Apparently, this is not true for the Tibetan earthquakes where the errors remain relatively uniform and small down to magnitudes near five.

DISCUSSION

Barazangi and Ni (1982), and Ni and Barazangi (1983) used P_n- and S_n- waves crossing the Tibetan Plateau, and obtained velocities of 8.42 km/sec for P_n, and 4.73 km/sec for S_n. Holt and Wallace (1990) inverted the P_{nl} waveform data and concluded that the P_n velocity is 8.24 km/sec beneath the Tibet region. Zhao et al. (1991) reported that the P_n velocity beneath the Tibetan Plateau is 8.3 km/sec, and that the S_n velocity is 4.6 km/sec by modeling SS and S waveforms. Zhao et al. (1991) did not use the absolute travel time in developing the velocity model TIP, but rather the differential travel times of $SS-S$, thus their results on the upper mantle velocities are not effected by the accuracy of the origin times. Using P_{nl} waveforms and the travel times of P_n and S_n phase may introduce two percent higher lid velocity bias due to the non-planar characteristics of the Moho boundary beneath the Tibetan Plateau as given by Zhao and Helmberger (1991).

Models based on absolute travel times obviously do depend on the origin time. For example, Holt and Wallace (1990) used 24 events from
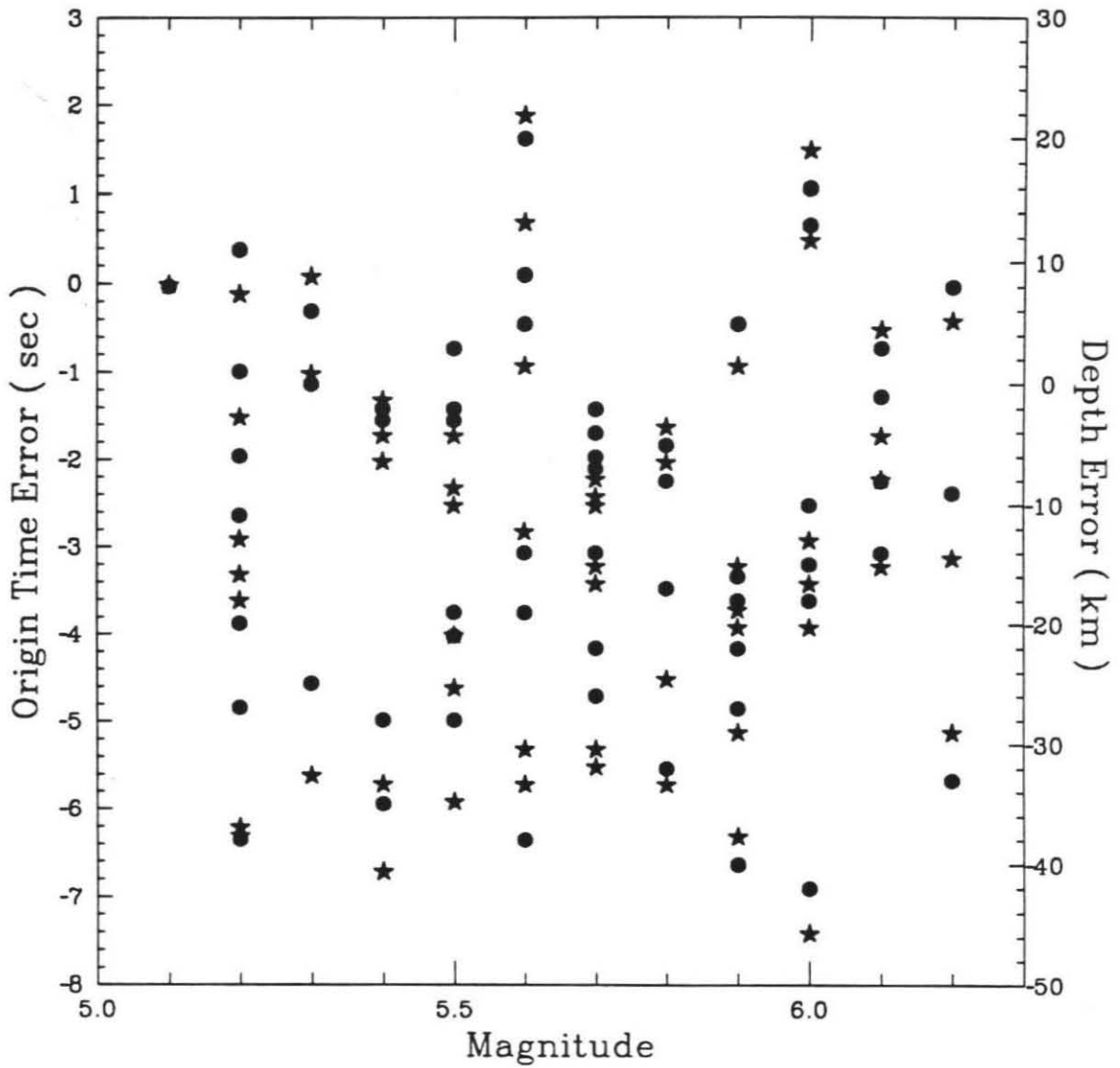
Figure 3. Origin time error and source depth error verses magnitude m_b. The dots indicate the data points of source depths, the stars indicate those of the origin times.

population given in Table 1. They assumed these events are shallow with depths similar to the relocated depths given in Table 1, and applied the ISC origin times with corrections of the source depth, dipping Moho and 70 km crust. If they did not correct the origin times, their P_n travel times would be 3.6 seconds too short relative to the results presented in Table 1 on average. Although they over corrected the effects of the velocity structure of source region, two seconds, (they assume that below the crust, the Tibetan Plateau has a JB velocity distribution), their result of P_n velocity 8.24 km/sec is reasonable.

The origin time effects on the P_n and S_n results from the regional phases are slightly less dramatic, if both the source depths and origin times of ISC are used. This is because the deeper source depth of ISC compensates its later origin time. The effects of origin time errors and depth errors on the travel times of P_n and S_n are given by

$$\Delta T_{P_n} = -0.034H + 1.43 \tag{7}$$

and

$$\Delta T_{S_n} = 0.044H + 1.43 \tag{8}$$

assuming that the compressional velocity 6.2 km/sec, the shear velocity 3.5 km /sec for the crust and velocities for the mantle are 8.3 and 4.6 kms^{-1} respectively. Averaging over all the relocated earthquakes, yields $\Delta T_{Pn} = +1.8$ seconds and $\Delta T_{Sn} = +0.95$ seconds.

The travel time of P_n phase recorded at a station 10 degrees away from the source is about 140 seconds. From Equation (7), the P_n travel time is 1.8 seconds longer than that predicted by using ISC origin time and source depth, averaging over all the relocated earthquakes. Considering this

travel time difference, we get a P_n velocity of 8.43 kms^{-1} by using the P_n travel time predicted by using ISC source depth and origin time if the real P_n velocity is 8.30 kms^{-1}. This velocity difference almost covers the possible models proposed for the Tibet region discussed earlier.

The S_n travel time of a source-receiver distance of 10 degrees is about 260 seconds. From Equation (8), the S_n travel time is 0.95 seconds longer than that predicted by using ISC origin time and source depth, averaging over all the earthquakes we relocated. Considering this travel time difference, we get a S_n velocity of 4.62 kms^{-1} by using S_n travel time predicted by using ISC source depth and origin time if the real S_n velocity is 4.60 kms^{-1}. Thus the origin time and source depth given by ISC do not make very much difference to the S_n velocity if only S_n travel times are used. In short the travel time errors introduced by the ISC origin times and source depths lead to about 1.5 per cent over-estimate of the P_n velocity and about 0.5 per cent over-estimated of the S_n velocity.

The ISC location of the earthquakes are not badly mislocated. However this mislocation may introduce more than 5 seconds to regional Love wave travel times, since the group velocity of the maximum amplitude of Love waves is about 3.5 km/sec. Thus, this small mislocation can lead to a bias in the velocity model. For example, suppose we consider the events discussed by Zhao et al. (1991), see Table 2. In this table, ΔD is the distance between the old and new location in kms at a number of stations surrounding Tibet. Positive values mean that the new distances are larger, ΔT_{syn} is the synthetic travel time correction caused by the distance change assuming a 3.5 km/sec group velocity. ΔT_{obs} is the observed travel time change due to the change in origin time, and δT is defined as $T_{obs} - T_{syn}$. From this table,

Table 2.

Data	Time	Station	Distance	ΔD	ΔT_{syn}	ΔT_{obs}	δT
08 15 67	0921	SHL	649	19.2	5.5	5.9	0.4
08 30 67	1108	NDI	2242	-2.1	-0.6	6.2	6.8
08 30 67	1108	LAH	2456	-4.9	-1.4	6.2	7.6
08 30 72	1514	NDI	1995	-0.4	-0.1	2.5	2.6
02 07 73	1606	NDI	2241	-4.4	-1.3	5.1	6.4
02 07 73	1606	NIL	2540	-6.6	-1.9	5.1	7.0
06 15 82	2324	NDI	2209	0.4	0.1	2.3	2.2

we see that the velocity structure derived by using the travel times of Love waves are about one percent exaggerated. Zhao et al. (1991) claim that TIP's crustal model is mainly for the southern part of the Tibetan Plateau, If we include the effects of the new origin times and locations given here, the crustal velocity structure appropriate for the northern part of the Plateau is about three percent slower than indicated by TIP.

In conclusion, we investigated about 100 Tibetan earthquakes and found that most of these events are shallower than reported by ISC; most are no deeper than 20 km. We relocated 59 of them, and found that the average origin time is 3.06 seconds earlier than that reported by ISC. Eleven of them are more than 5.5 seconds earlier than reported. Applying these corrections to P_n and S_n travel times explains why many authors have over-estimated the upper mantle velocities beneath the Tibetan Plateau.

ACKNOWLEDGMENTS

REFERENCES

Baranowski, H., H. Armbruster, L. Seeber and P. Molnar, (1984). Focal depths and fault plane solutions of earthquakes and active tectonics of the Himalaya, *J. Geophys. Res.*, **89**, 6919-6928.

Barazangi, M., and J. Ni, 1982. Velocities and propagation characteristics of *Pn* and *Sn* beneath the Himalayan arc and Tibetan Plateau: possible evidence for underthrusting of Indian continental lithosphere beneath Tibet, *Geology*,**10**, 179-185.

Chandra, U., (1978). Seismicity, earthquake mechanisms and tectonics along the Himalayan mountain range and vicinity, *Phys. Earth Planet. Inter.*, **16**, 109-131.

Dziewonski, A. M, and D. L. Anderson, (1983). Travel times and station corrections for P waves at teleseismic distances, *J. Geophys. Res.*, **88**, 3295-3314.

Fan, Guangwei and J. F. Ni, (1989). Source parameters of the 13 February 1980, Karakorum earthquake, *Bull. Seis. Soc. Am.*, **79**, 945-954.

Fitch, T. J. 1970, Earthquake mechanism in the Himalayan, Burmese, and Andaman regions and continental tectonics in central Asia, *J. Geophys. Res.*, **75**, 2699-2709.

Holt, W. E. and T. C. Wallace, (1990). Crustal thickness and upper mantle velocities in the Tibetan Plateau region from the inversion of regional P_{nl} waveforms: Evidence for a thick upper mantle lid beneath southern Tibet, *J. Geophys. Res.* **95**, 12499-12525.

Langston, C. A., and D. V. Helmberger, 1975. A procedure for modeling shallow dislocation sources, *Geophys. J. R. astr. Soc.*, **42**, 117-130.

Molnar, P., T. J. Fitch, and F. T. Wu, (1973). Fault plane solutions of shallow earthquakes and contemporary tectonics in Asia, *Earth Planet. Sci. Let.*, **19**, 101-112.

Molnar, P. and W.-P. Chen, (1983). Focal depths and fault plane solutions of earthquakes under the Tibetan Plateau, *J. Geophys. Res.*, **88**, 1180-1196.

Molnar, P. and W.-P. Chen, (1984). S-P wave travel time residuals and lateral inhomogeneity in the mantle beneath Tibet and the Hymalaya, *J. Geophys. Res.*, **89**, 6911-6917.

Molnar, P. and H. Lyon-Caen, (1989), Fault plane solutions of earthquakes and active tectonics of the Tibetan Plateau and its margins, *Geophys. J. Int.*, **99**, 123-153.

Nelson, M. R., R. McCaffrey, and P. Molnar, (1987). Source parameters for 11 earthquakes in the Tien Shan, Central Asia, determined by P and SH waveform inversion, *J. Geophys. Res.*, **92**, 12629-12648.

Ni, J., and M. Barazangi, 1983. High frequency seismic wave propagation beneath the Indian Shield, Himalayan arc, Tibetan Plateau and surrounding regions: High uppermost mantle velocities and efficient *Sn* propagation beneath Tibet, *Geophys. J. R. astr. Soc.*, **72**, 665-681.

Ni, J., and M. Barazangi, (1984). Seismotectonics of the Himalayan collision zone: geometry of the underthrusting Indian plate beneath the Himalaya, *J. Geophys. Res.*, **89**, 1147-1163.

Zhao, Lian-She, D. V. Helmberger, and D. G. Harkrider, (1991). Shear-velocity structure of the crust and upper mantle beneath Tibetan and southeastern China. *Geophys. J. Int.* in press.

Zhao, Lian-She and D. V. Helmberger (1991) Non-planar Moho effects on

the lid velocity, manuscript in preparation.

Zhou, Huilan, Hsui-Lin Liu, and H. Kanamori, (1983). Source processes of large earthquakes along the Xianshuihe fault in southwestern China, *Bull. Seis. Soc. Am.*, **73**, 537-551

APPENDIX A

For inclusion of this and rotated versions of this source into a vertically inhomogeneous half-space, it is convenient to express the source in

$$\mathbf{u} = \nabla\Phi + \nabla\times\Psi \tag{A1}$$

where Φ is the P wave potential and Ψ is the S wave potential. For the external medium, the P and S wave potentials can be expressed as

$$\Phi = \frac{1}{k_\alpha} \sum_{l=0}^{l=\infty} (2l+1) d_l h_l^{(2)}(k_\alpha r) P_l(\cos\delta) \tag{A2}$$

$$\Psi = -\frac{1}{k_\beta} \sum_{l=0}^{l=\infty} (2l+1) c_l h_l^{(2)}(k_\beta r) \frac{d}{d\delta} P_l(\cos\delta) \mathbf{e}_\gamma \tag{A3}$$

For the translated coordinate system with the source located at (r_0, θ_0, ϕ_0), Figure 1 , we use the addition theorem for zonal harmonics

$$P_l(\cos\delta) = \sum_{m=0}^{l} \epsilon_m \frac{(l-m)!}{(l+m)!} P_l^m(\cos\theta) P_l^m(\cos\theta_0)(\cos m\,\phi\cos m\,\phi_0 + \sin m\,\phi\sin m\,\phi_0)$$

$$\tag{A4}$$

Substituting (A4) into equation (A2), we obtain equation (A5).

$$\Phi = -\frac{1}{k_\alpha^2} \sum_{n=0}^{n=\infty} \sum_{m=0}^{m=n} [A_{nm} \cos m\,\phi + B_{nm} \sin m\,\phi] P_n^m(\cos\theta) h_n^{(2)}(k_\alpha r) \tag{A5}$$

where

$$A_{nm} = -(2n+1)\frac{(n-m)!}{(n+m)!}k_\alpha d_n \epsilon_m P_n^m(\cos\theta_0)\cos m\,\phi_0$$

(A6)

$$B_{nm} = -(2n+1)\frac{(n-m)!}{(n+m)!}k_\alpha d_n \epsilon_m P_n^m(\cos\theta_0)\sin m\,\phi_0$$

For the shear potential, we implicitly define ψ as

$$\mathbf{\Psi} = \psi\mathbf{e}_\gamma.$$

and in the translated coordinates

$$\mathbf{\Psi} = \psi^r\mathbf{e}_r + \psi^\theta\mathbf{e}_\theta + \psi^\phi\mathbf{e}_\phi$$

with

$$\psi^r = 0,$$

$$\psi^\theta = -\psi\sin\theta_0\sin(\phi-\phi_0)/\sin\delta,$$

and

$$\psi^\phi = -\psi(\sin\theta_0\cos\theta\cos(\phi-\phi_0)-\cos\theta_0\sin\theta)/\sin\delta.$$

Defining

$$\phi_n = \frac{\mathrm{d}}{\mathrm{d}\delta}P_n(\cos\delta)\mathbf{e}_\gamma$$

, or

$$\phi_n = -P_n'(\cos\delta)\mathbf{e}_{r_0}\times\mathbf{e}_r$$

we obtain

$$\phi_{n1} = -P_n'(\cos\delta)(\sin\theta_0\sin\phi_0\cos\theta-\sin\theta\sin\phi\cos\theta_0)$$

$$\phi_{n2}=-P_n^{'}(\cos\delta)(\cos\theta_0\sin\theta\cos\phi-\sin\theta_0\cos\phi_0\cos\theta)$$

$$\phi_{n3}=-P_n^{'}(\cos\delta)(\sin\theta_0\sin\theta\sin(\phi-\phi_0))$$

where

$$P_n^{'}(\cos\delta)=\frac{dP_n(\cos\delta)}{d\cos\delta}$$

Then,

$$\frac{\partial P_n(\cos\delta)}{\partial\phi_0}=P_n^{'}(\cos\delta)\sin\theta\sin\theta_0\sin(\phi-\phi_0)=-\phi_{n3},$$

$$\phi_{n1}=\sin\phi_0\frac{\partial P_n(\cos\delta)}{\partial\theta_0}-\cot\theta_0\cos\phi_0\cdot\phi_{n3},$$

and

$$\phi_{n2}=-\cos\phi_0\frac{\partial P_n(\cos\delta)}{\partial\theta_0}-\cot\theta_0\sin\phi_0\cdot\phi_{n3}.$$

From these relations, it is not difficult to get equation (A7) in a manner similar to equation (A5).

$$\Psi_j=-\frac{2}{k_\beta^2}\sum_{n=0}^{n=\infty}\sum_{m=0}^{m=n}[C_{nm}^{(j)}\cos m\,\phi+D_{nm}^{(j)}\sin m\,\phi]P_n^m(\cos\theta)h_n^{(2)}(k_\beta r)\quad(A7)$$

where $\Psi_j(j=1,2,3)$ are the Cartesian components of the S wave potential Ψ, and

$$C_{nm}^{(1)}=-\frac{k_\beta}{2}(2n+1)\frac{(n-m)!}{(n+m)!}\epsilon_m\,c_n\,[\frac{d}{d\theta_0}P_n^m(\cos\theta_0)\sin\phi_0\cos m\,\phi_0$$

$$-mP_n^m(\cos\theta_0)\cot\theta_0\cos\phi_0\sin m\,\phi_0]$$

$$D_{nm}^{(1)} = -\frac{k_\beta}{2}(2n+1)\frac{(n-m)!}{(n+m)!}\epsilon_m\, c_n\,[\frac{d}{d\theta_0}P_n^m(\cos\theta_0)\sin\phi_0\sin m\,\phi_0$$

$$+mP_n^m(\cos\theta_0)\cot\theta_0\cos\phi_0\cos m\,\phi_0]$$

$$C_{nm}^{(2)} = \frac{k_\beta}{2}(2n+1)\frac{(n-m)!}{(n+m)!}\epsilon_m\, c_n\,[\frac{d}{d\theta_0}P_n^m(\cos\theta_0)\cos\phi_0\cos m\,\phi_0$$

$$+mP_n^m(\cos\theta_0)\cot\theta_0\sin\phi_0\sin m\,\phi_0]$$

$$(A8)$$

$$D_{nm}^{(2)} = \frac{k_\beta}{2}(2n+1)\frac{(n-m)!}{(n+m)!}\epsilon_m\, c_n\,[\frac{d}{d\theta_0}P_n^m(\cos\theta_0)\cos\phi_0\sin m\,\phi_0$$

$$-mP_n^m(\cos\theta_0)\cot\theta_0\sin\phi_0\cos m\,\phi_0]$$

$$C_{nm}^{(3)} = -\frac{k_\beta}{2}(2n+1)\frac{(n-m)!}{(n+m)!}\epsilon_m\, c_n\, P_n^m(\cos\theta_0)\sin m\,\phi_0$$

$$D_{nm}^{(3)} = \frac{k_\beta}{2}(2n+1)\frac{(n-m)!}{(n+m)!}\epsilon_m\, c_n\, P_n^m(\cos\theta_0)\cos m\,\phi_0$$

where $\epsilon_m = 1$ if $m = 0$, $\epsilon_m = 2$ if $m \neq 0$. Ψ_3 is the SH wave potential.

From the equation (A8), we see that SH waves will be generated if $C_{nm}^{(3)}$ and $D_{nm}^{(3)}$ are not zero in Cartesian coordinate system. Harkrider et al. (1992) gives a detailed derivation of the surface waves in layered media due to a transparent source expressed in the general form (A5) and (A7).

When the explosion source is on the z axis, as in equation (A3), there are only SV waves because of symmetry. As one moves the source off the z axis, the $C_{nm}^{(3)}$ and $D_{nm}^{(3)}$ are no longer zero and we have SH waves as one would expect.

APPENDIX B

In this appendix, we give the analytic solution for the source at the center of the cavity. From equation (1), we have

$$\mathbf{u}_1 = A \mathbf{L}_{0,0}^-(k_{\alpha_1} r) - b \mathbf{L}_{0,0}^+(k_{\alpha_1} r) \tag{B1}$$

$$\mathbf{u}_2 = d \mathbf{L}_{0,0}^-(k_{\alpha_2} r) \tag{B2}$$

where A is $ik_{\alpha_1}^2 g(\omega) A_0$. Other terms in (1) are zero. From the boundary condition at $r = a$, we have

$$\begin{Bmatrix} b \\ d \end{Bmatrix} = \frac{A}{\Delta} \begin{bmatrix} F_{0,3}^-(\xi_2) & -h_0^{(2)'}(\xi_2) \\ -\gamma F_{0,3}^+(\xi_1) & j_0'(\xi_1) \end{bmatrix} \begin{bmatrix} h_0^{(2)'}(\xi_1) \\ \gamma F_{0,3}^-(\xi_1) \end{bmatrix} \tag{B3}$$

where $\xi_i = k_{\alpha_i} a$, $\gamma = \dfrac{\mu_1 k_{\alpha_1}}{\mu_2 k_{\alpha_2}}$, and

$$\Delta = F_{0,3}^-(\xi_2) j_0'(\xi_1) - \gamma h_0^{(2)'}(\xi_2) F_{0,3}^+(\xi_1).$$

According to the relations of Bessel functions, we have

$$\Delta = h_0^{(2)}(\xi_2) j_0(\xi_1) [(cot\,\xi_1 - \frac{1}{\xi_1})(i + \frac{1}{\xi_2})(\frac{2}{\xi_2} - \frac{2\gamma}{\xi_1}) -$$

$$\frac{1}{2}(\frac{\alpha_2}{\beta_2})^2 (cot\,\xi_1 - \frac{1}{\xi_1}) - \frac{1}{2}(\frac{\alpha_1}{\beta_1})^2 \gamma(i + \frac{1}{\xi_2})].$$

From equations (B2) and (B3), $\mathbf{u}_2$ can be written as

$$\mathbf{u}_2 = \frac{A_0}{2a^2\Delta} g(\omega) \frac{\mu_1 k_{\alpha_1}}{\mu_2 k_{\alpha_2}} \left(\frac{\alpha_1}{\beta_1}\right)^2 h_0^{(2)'}(k_{\alpha_2}r)\mathbf{e}_r. \tag{B4}$$

APPENDIX C

The Error Analysis of Surface Wave Dispersion Curves Determined by Frequency-Time Analysis

ABSTRACT

Numerical experiments and Mathematical proof show that the surface wave dispersion curve is highly suspectable for the periods much longer than the duration of the source for the regional records.

The surface wave dispersion curves have been used extensively to understand the earth structure. The techniques used to determine the dispersion curves are generally " frequency-time analysis (FTAN) " (Landisman et al. 1969 , Dziewonski et al. 1969), " display-equalized filter (DEF) " (Nyman and Landisman, 1977). Feng and Teng (1983) gave an error analysis of frequency-time analysis.

Numerical Example

Figure C1 shows numerical examples of the determination of surface wave dispersion curves. The parameters used for these synthetics:
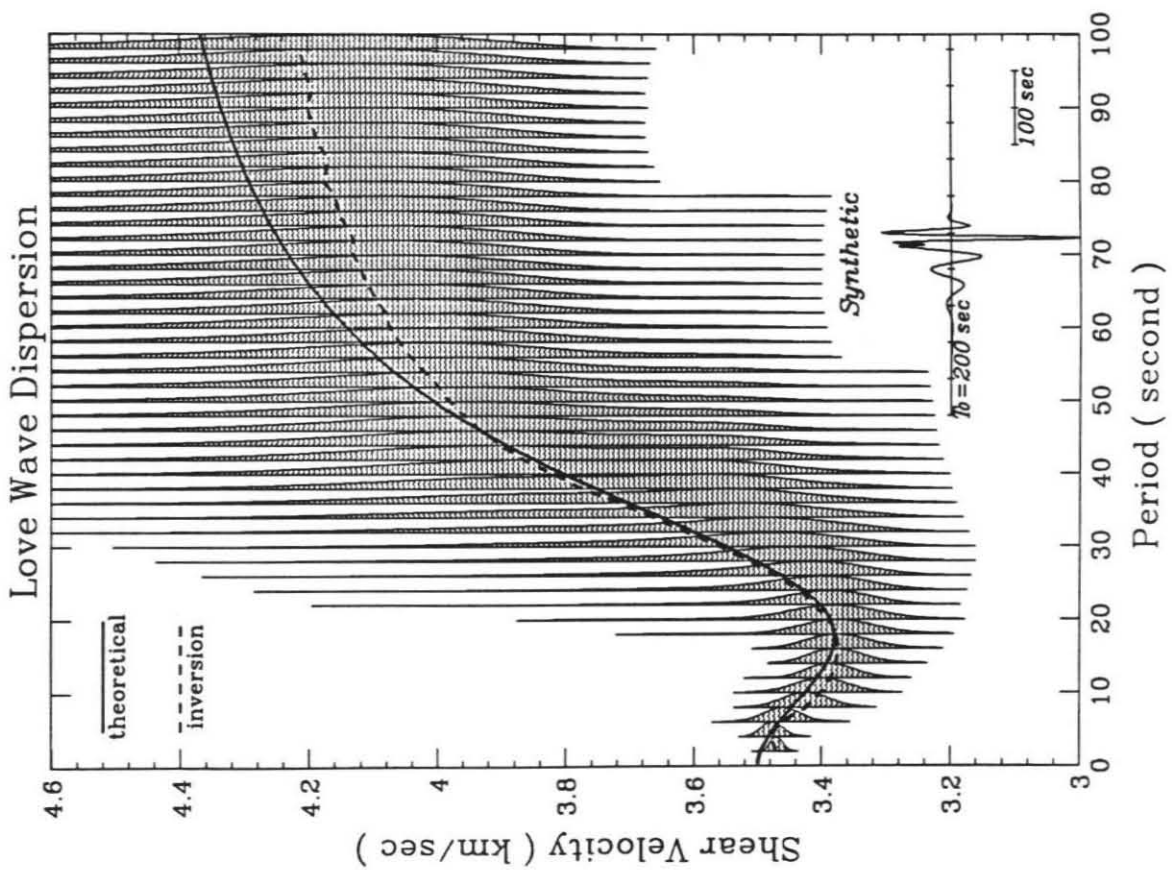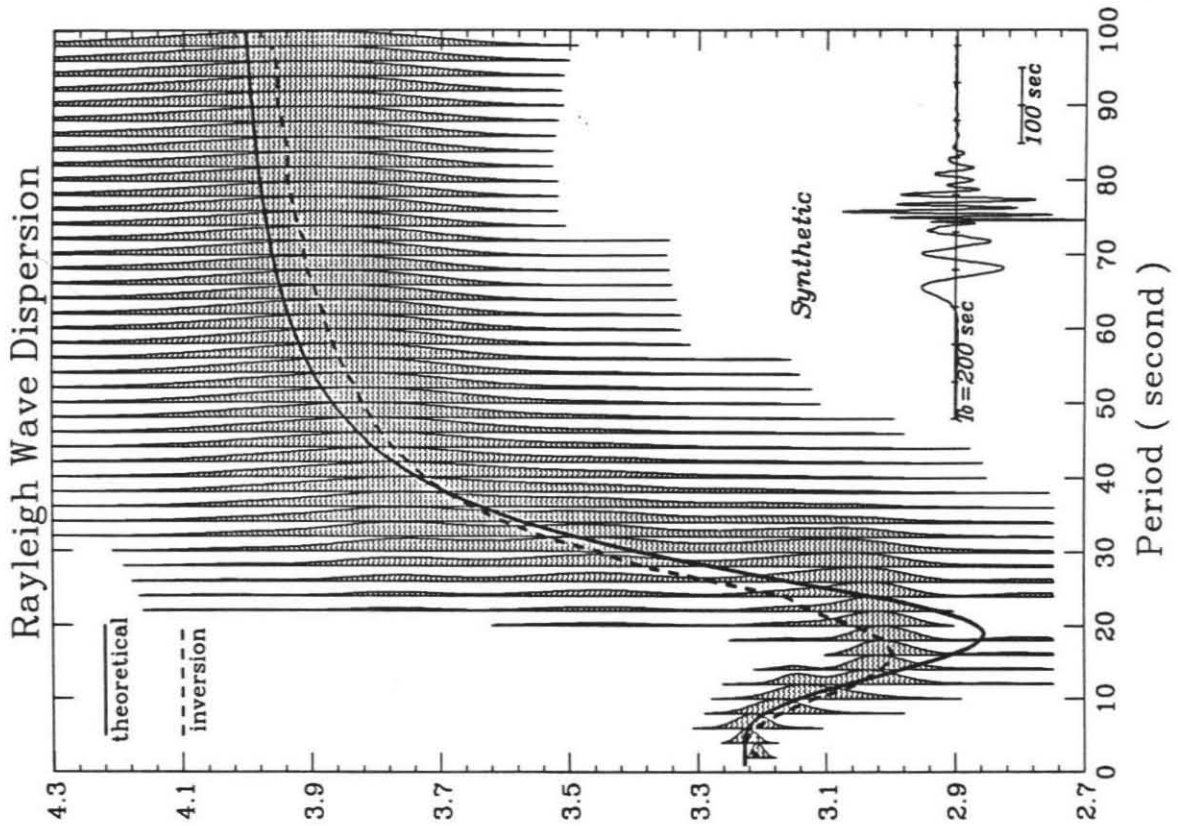
Figure C1. Accuracy of the determinations of the surface wave dispersion curves. Left panel shows Love waves and the right shows Rayleigh waves. The solid lines is the dispersion curves of the model used to make the synthetics shown on the bottom right corner of each panel. The dash lines are the predicted dispersion curves from the synthetics by using the DEF method (Nyman and Landisman, 1977). The shaded areas are the areas under the envelop the amplitudes of filtered seismograms. The shaded areas can serve as error bars of the determined dispersion curve.

Distance=1500km, Δt =0.5 seconds, strike-slip source with 2, 2, 4 trapezoidal source function and a depth of 10 km, the length of Rayleigh wave synthetics is 1024 seconds and that for Love wave synthetics is 512 seconds, no instrument is applied. The method used to make these synthetics is Mode Summation Method (Harkrider, 1964, 1972). The model parameters are: α_c =6.2, β_c =3.5 for the crust with 32 km thickness and α_m =8.2, β_m =4.5 half-space mantle. The synthetics are fundamental mode only. The method used is DEF (Nyman and Landisman, 1977). We used the point in time domain that divides the area beneath the absolute amplitude curve into two equal parts after inverse FFT as the travel time of the frequency. In Figure C1, the solid lines are the dispersion curves we used to make the synthetics shown on the bottom. The dashed lines are the predictions. The errors on the dispersion curves are more than ten percent. The shaded areas are the absolute amplitude. They serve as error bars. The error bar is larger than 0.5 km/sec, see Figure 4. From Figure 4, we can see that the dispersion curve can never be determined within high accuracy even under idealized conditions, long datum segment, noise free, no instrument, no higher mode contaminations. These results can be proved mathematically even under extreme conditions.

Mathematical Proof

First we organize the problem of the determination of surface wave dispersion curves in to the mathematical problem. The spectrum of surface wave displacements caused by an earthquake for a station at azimuth ϕ and

epicentral distance r can be written as:

$$G(w)=S(w,\phi)e^{-ikr}e^{-wr/2Qu}e^{i\phi} \tag{C1}$$

where $S(w,\phi)$ is source spectrum (Zhang and Lay, 1989; Kanamori and Given, 1981). Using multiple filter technique (Dziewonski et al. 1969), we have

$$x_n(t)=\frac{1}{2\pi}\int\limits_{-\infty}^{\infty}G(w,\phi)e^{-\alpha(\frac{w-w_\ast}{w_\ast})^2}e^{irf(w,w_\ast)}P(w,w_n)e^{-iwt}dw, \tag{C2}$$

where $P(w,w_n)e^{irf(w,w_\ast)}$ is called an isolation filter. Find out t_m where $|x_n(t)|$ reaches its maximum, the velocity $v_n=r/T_m$ is the group velocity for the frequency w_n.

Now, we assume the source function of the earthquake is $h(t)$, it has its maximum at $t=0$ and it is zero outside of interval $[h_1,h_2]$. The source spectrum $S(w,\phi)$ is

$$S(w,\phi)=\int\limits_{h_1}^{h_2}h(T)e^{-iwT}dT, \tag{C3}$$

and using

$$e^{-irf(w,w_\ast)}=e^{ikr+wr/2Qu}, \tag{C4}$$

we have

$$x_n(t)=\int\limits_{-\infty}^{\infty}e^{-(\frac{w-w_\ast}{w_\ast})^2}e^{iwt}dw\int\limits_{h_1}^{h_2}h(T)e^{-iwT}dT. \tag{C5}$$

After manipulations, we have

$$x_n(t) = w_n \left(\frac{\pi}{\alpha}\right)^{1/2} \int_{h_1}^{h_2} h(T) e^{-\frac{w_n^2}{4\alpha}(T-t)^2 - iw_n(T-t)} dT. \tag{C6}$$

From this formula, we can see that $|x_n(t)|$ reaches its maximum when $t=0$ for high frequency $w_n \gg 1$. For the low frequency $w_n \ll 1$, i. e., $w_n = 2\pi/T_n$, $T_n \gg h_2$, or $-h_1$, we have $\frac{dx_n}{dt} \approx w_n^3$. This means $x_n(t)$ is a constant over a broad time range. It is not possible to get a group velocity for the lower frequency. This is the end of the proof. In the Figure C1, it was clearly shown that the error bars or the envelop of $x_n(t)$ are so big at lower frequency end.

The assumption we used in Equation (C4) means that we know exactly the structure of the path, i. e., the dispersion curves. Under this strong assumption, it is still not possible to determine the group velocity with high accuracy. This mathematical result simply suggests that it is impossible to obtain the dispersion curves accurately.

REFERENCES

Dziewonski, D. A., S. Bloch and M. Landisman, 1969 . A technique for the analysis of transient seismic signals, *Bull. Seism. Soc. Am.*, **59**, 427-44.

Feng, C.-C., and T.-L. Teng, 1983. An error analysis of frequency-time analysis, *Bull. Seism. Soc. Am.*, **73**, 143-155.

Harkrider, D. G., 1964. Surface waves in multilayered elastic media, I. Rayleigh and Love waves from buried sources in a multilayered elastic half-space, *Bull. Seism. Soc. Am.*, **54**, 627-679.

Harkrider, D. G., 1970. Surface waves in multilayered elastic media, II. Higher mode spectra and spectral ratios from point sources in plane layered Earth models, *Bull. Seism. Soc. Am.* , **54**, 1937-1987.

Kanamori, H. and J. Given, 1981. Use of long-period surface waves for rapid determination of earthquake-source parameters, *Phys. Earth Planet. Inter.*, **27**, 8-31.

Landisman, M., A. Dziewonski, and Y. Sato, 1969. Recent improvements in the analysis of surface wave observations, FIGeophys. J., **17**, 369-403.

Nyman, D. C., and M. Landisman, 1977. The display equalized filter for frequency-time analysis, *Bull. Seism. Soc. Am.*, **67**, 393-404.

Zhang, J.-J., and T. Lay, 1989. Measuring complex spectra of long-period surface waves for earthquake source analysis, *Geophys. Res. Lett.*, **16**, 259-262.